Condensation Frosting:
From Ice Bridges to Dry Zones

Saurabh Nath

Thesis submitted to the Faculty of the
Virginia Polytechnic Institute and State University
in partial fulfillment of the requirements for the degree of

Master of Science
in
Engineering Mechanics

Jonathan B. Boreyko
Pengtao Yue
Sunny Jung
James Hanna
Mark R. Paul

July 17, 2017
Blacksburg, Virginia

Condensation Frosting: From Ice Bridges to Dry Zones

Saurabh Nath

(ABSTRACT)

The most ubiquitous mode of frost formation on substrates is condensation frosting, where dew drops condense on a supercooled surface and subsequently freeze, and has been known since the time of Aristotle. The physics of frost incipience on a microscopic scale has, nevertheless, eluded researchers because of an unjustified ansatz regarding the primary mechanism of condensation frosting. It was widely assumed that during condensation frosting each supercooled droplet in the condensate population freezes in isolation by heterogeneous nucleation at the solid-liquid interface, quite analogous to the mechanism of icing. This assumption has very recently been invalidated with strong experimental evidence which shows that *only a single droplet* has to freeze by heterogeneous nucleation (typically by edge effects) in order to initiate condensation frosting in a supercooled condensate population. Once a droplet has frozen, it subsequently grows an ice bridge towards its nearest neighboring liquid droplet, freezing it in the process. Thus ensues a chain reaction of ice bridging where the newly frozen droplets grow ice bridges toward their nearest neighbor liquid droplets forming a percolating network of interconnected frozen droplets. Not always are these ice bridges successful in connecting to their adjacent liquid droplets. Sometimes the liquid droplet can completely evaporate before the ice bridges can connect, thus forming a local dry region in the vicinity of the ice bridge.

In this work, we first formulate a thermodynamic framework in order to understand the localized vapor pressure gradients that emerge in mixed-mode phase-change systems and govern condensation and frost phenomena. Following this, we study droplet pair interactions between a frozen droplet and a liquid droplet to understand the physics behind the local ice bridge connections. We discuss the emergent scaling laws in ice bridging dynamics, their relative size dependencies, and growth rates. Thereafter, we show how with spatial control of inter-droplet distances in a supercooled condensate and temporal control of the first freezing event, we can tune global frost propagation on a substrate and even cause a global failure of all ice bridges to create a dry zone. Subsequently, we perform a systematic study of dry zones and derive a scaling law for dry zones that collapses all of our experimental data spanning a wide parameter space. We then show that dry zones forming around hygroscopic droplets are almost always regions of inhibited growth and not of inhibited nucleation. Finally, we end with a discussion and preliminary results of our proposed anti-frosting surface that uses ice itself to prevent frost.

Condensation Frosting: From Ice Bridges to Dry Zones

Saurabh Nath

(GENERAL AUDIENCE ABSTRACT)

In the movie *Iron Man*, during the very final battle sequence between our eponymous hero and Iron Monger, there is a moment when Tony Stark realizes that Iron Monger can fly. Immediately Iron Man shoots up into the sky. He tries to reach as high as he can. Iron Monger chases after him. Eventually, high up in the sky amidst the clouds, Iron Monger catches up. He grabs Iron Man in his enormous grip and punches him. It seems like there is no escape for Iron Man. But right then, writhing in Iron Monger's grip, Tony Stark asks Iron Monger, *'How'd you solve the icing problem?'* It is then revealed that Iron Monger's suit has completely frozen over, whereas Iron Man's suit has no ice whatsoever. Iron Monger shuts down and starts falling from the sky.

The *icing problem*, which Tony Stark mentions, occurs when supercooled liquid water droplets impact on a chilled substrate and subsequently freeze. Another way of accretion of ice constitutes the *frosting problem*. The most common mode of frost formation on a surface is called condensation frosting, where the ambient water vapor first condenses on the chilled surface as dew drops, and these liquid droplets subsequently freeze. Until very recently, it was widely assumed that during condensation frosting all the dew droplets freeze in isolation at the solid-liquid interface, without interacting with each other. This assumption, however, is not true. It has recently been shown that in order to initiate condensate frosting, *only a single droplet* has to freeze by itself, at the solid-liquid interface. Thereafter, frost propagates by the formation of an inter-droplet ice bridge network, where the frozen droplets grow ice bridges toward their nearest neighbor liquid droplets. Interestingly, these ice bridges are not always successful in connecting to their adjacent liquid droplets. If the inter-droplet distance is too large, the liquid droplet can completely evaporate before the ice bridges can connect, thus forming a local dry region in the vicinity of the ice bridge. In this work, we do extensive experiments to investigate the underlying physics of frost incipience on a microscopic scale. We then derive scaling laws for successful ice connections, their growth rates and for dry zone formations, and end by discussing possible anti-frosting strategies.

It appears that Tony Stark in his universe has solved the *icing problem*, and most probably also the *frosting problem*. In reality, however, on earth, we have not. Though anti-icing has received a lot of attention, the same cannot be said about the *frosting problem*. This work tries to take the first steps towards that. Quite ironically, it looks like ice itself might be the solution to the *frosting problem*, because of its ability to create dry zones.

ולמד
למוד

Acknowledgements

I struggle.
I struggle with words.
With ideas. With things that I know. And know not.
I struggle to be the person I want to be. I struggle to understand who I am.
Why I am. I do not know. I do not.
But I do know – whoever I am, I am only so for the seasons I've seen.
And, of the many seasons I saw, I see, I'll see
Blacksburg will forever be
The Śhorôt[1] of my life.
It will be.

Thank you.

Thank you, Jonathan! Thank you for everything! From our unending discussions on research, on philosophy, on determinism, on free will, on movies, on music and on all things under the sun. We have not agreed on everything, but I have learned about everything. And you have profoundly influenced my ideas. You have changed the way I think, the way I approach research, life, philosophy, and what not! You taught me how to experiment, write papers, give talks, you encouraged me, rebuked me, inspired me. I really cherish the fact that I was your very first graduate student and got so much of your attention. It means a lot to me. I objectively feel you are a great advisor. I could not have asked for anything more.[2]

Thank you to all my committee members. Pengtao is an amazing researcher and an equally patient man. I will not forget how he patiently listened to each and every stream of consciousness idea I had regarding my research and stood by me when I struggled with my research. I have been fortunate to know Sunny. His ideas and thoughts on my research have been very insightful, and our conversations enlightening. Prof. Paul is one of the best teachers I have seen and his course on Chaos was undoubtedly the best physics course I have ever had. And I have never seen someone like James before. I feel no matter what I am working on, if I am ever stuck on anything and have no way to proceed any further, when everyone has given up, all roads are closed, all I need to do is go to James – he will undoubtedly tell me something, which I will not understand then, but *eventually* I will, and the solution would emerge from there.[3] To me he is like a sage old man, though he is not really old, who knows something about everything, and just enough to always show you the way. He was the first person I ever spoke to at Virginia Tech and I will never forget that hour-long conversation I had with him over phone from India! Maybe he does not know, but the way he spoke that day really inspired a naive young kid, who really wanted to do research but in reality knew nothing about it.

I have had really great labmates,[4] who have tolerated me, no matter what – Kevin, Wei Wei and Mohammad, and some amazing undergrads[5] – Christian, Corey, Daniel, Grady, Josh, Julia, Katherine, Lance, Matt, Megan, Zara,and Ziad. Special mention: Caitlin and Stuti, you were just awesome! And Austin, you were not an undergrad. You were a grad!

---

[2] Maybe an IR Camera...

[3] I have multiple instances of this, but the most vivid one that comes to mind is that of one particularly dry afternoon. I was struggling with modeling co-operative evaporation of droplets and had almost given up, when I happened to chance upon him. He told me something about *'Russians and bispherical co-ordinates'*, which made little sense... But, the literature trail that sent me on, three months down the line, eventually landed me on Ivanstov, Müller-Krumbhaar and the entire crystallography literature.

[4] Specific details in the marvellous artwork on our lab door

[5] Who are now frankly too many to count and whose names I cannot remember.

I miss my incessant ramblings on different ideas with Sean.

And now I will miss my incessant ramblings on different ideas with Brian.[6]

But most of all, I will miss my ramblings with Farzad. He is the one who has literally been there by me, all of my days at 109 Norris. Little did I know when I came to Virginia, that I would find a brother, a brother who can do anything – he is the elastician, he is the mathematician, he is the experimentalist! He is everything! He is Bruce Banner! There is no one like Farzad. And there will never be. And I'll never forget the endless conversations we've had over our coffee and cigarettes, and the countless problems we started but never finished. So many Seattle's Best's napkins with our scribbles and doodles that they could fill up the entire Seattle's Best itself!

Thanks to Lisa, Melissa, Jessica, Cristina and Bev, and Darrell and Dave, without whom not a single set-up would have been made!

And Bailey, who used to be the only other living soul in Norris Hall barring me, awake in the dead of night. Thank you for your wonderful company![7]

I would like to now thank a few people, who helped me overcome a very turbulent time of my life, without whom I would not have been in Blacksburg: PapiyaDi, ParomitaDi and JBNSTS, Swarnendu Sir, Ranjan Sir and DRC. And SouvickDa and BratoDa, and Rama Govindarajan – you have inspired me, influenced me and changed my being. I am greatly indebted to all of you. I was also not without friends then, and that I survived is only because of them – Anish and Namrata.

And, of course, my family.

---

[6] Hopefully not for long. :) :) :)

[7] Here 'company' means infinite supply of candies and chocolates!

Phew! Now it's time to give thanks to all my friends and family in Blacksburg. And it is a long list. So, leave if you will, else buckle up! Let's go ...

First, they, who were a part of my fateful experiences when I arrived here in Blacksburg – Pramit, Soumik, DebjitDa, Santa and Leo, and Mudassar Haidat, a certain benevolent middle-aged man from Pakistan. He and his limousine bus brought me to what would be my abode for the next three years – Apts. #2 & #10 of 1309. Those apartments are sure gone now, but their air is still heavy with our shouts and screams, incomplete dreams and peals of hysterical laughter.[8]

Next, they, who were my guardians of sort in Blacksburg – ShreyaDi and GabluDa, and GuptaDa ~~and PoornaDi~~,[9] trying relentlessly (and pointlessly) to moderate/ discipline/ civilize me, trying to make a man out of me. Of course, these naive endeavors have all ended in an epic failure of gargantuan proportions, as is evident. Nevertheless, they have made me realize something that I had never known before – what it feels like to have an elder sister or an elder brother. And then there is that moment when Gablu-Gabli call me to their house, and GabluDa says '*Shukhobor Achhe*'! I have never felt happier!

My amazing roommates – I have had two: WrikDa, the invisible roommate, who paid my bills, took out the trash, checked the mailbox, and never made me feel I had a roommate at all.[10] And Sreeya – who made me realize what having a roommate actually felt like, ~~for better or worse~~. And yes, you are the best roommate![11] You have been much more than a roommate.

And my juniors, who taught me *empathy*. For my seniors.[12] – GB, Ritwam, Saikat, Jana, Padhi, Appy, Lekha, Kar, Aheli, Rounak, Kochi, Bashok...

And my seniors, who I am surprised have not killed themselves already, after having us as their juniors – PoornaDi, Godfather, BratoDa, HossainDa, SrijanDa, ProsenDa, DonuDa, DebaratiDi, SubhradeepDa, MalayDa, DebaDa, GothDa, SuvankarDa, AritraDa, AvikDa, SRC, BikramDa, AtashiDi, KunduDa, NaikDa, DaduDa, SukanyaDi, SouravDa, RamkrishnaDa, ShibajiDa... and a glass of water!

And Paul, for being the elder brother to us all.

And Shuchi, for her midnight tales of frightful noir and our unfinished squabbles.[13]

---

[8] And carrom, cards and nicotine.

[9] Pssst! You are not my guardian!

[10] Barring the time he came to play chess with me and made me realize that even chess is not for me

[11] Since invisible roommates do not count

[12] Sympathy for ShreyaDi and GabluDa

[13] Floating in the air somewhere in West Virginia

And Ranit, for helping me survive undergrad and finally listening to me and joining academia.[14]

And it does not stop here, there's more: Kedar and Aarushi, I do not why I am mentioning you.[15]

And Parag, I can't think of any good things to say about you. I don't know – come to France![16]

And a little bit of gratitude for those without whom I am incomplete: Santa and Anish, who are the Huey and Dewey to my Louie.[17]

And my infinite love and appreciation for my Dad and Mom, who brought me to this world, showed sunshine and rain and gave me wings to fly, and deep affection for my lovely little sister.

And I end by saying, Namrata,[18] *if not for you...*

---

[14] Also surviving me five years in the same workspace – which no other friend of mine has actually pulled off. Santa – three years, Anish – four years, and Namrata – four years! That's no mean feat!

[15] I don't.

[16] My days in Blacksburg wouldn't have been the same without ~~you~~ your *chai*.

[17] the Bob and Pete to my Jupe, the Clotho and Lachesis to my Atropos, the R and G to my B, the Rock and Paper to my Scissors, the Stheno and Euryale to my Medusa, the Id and the Ego to my Super-ego, the Sachin and Dravid to my Sourav, the proton and neutron to my electron, the Amar and Akbar to my Anthony, the Om and Bhur to my Bhuva swaha ... This list is long. I can keep going. It will fill this thesis.

[18] *You met me at a very strange time in my life.*

"Some say the world will end in fire,
Some say in ice. "

$-Robert\ Frost$

Contents

List of Figures

xv

xxi

7.4   a) Phase Map of Nucleation and Flux Dry Zones. Dry zone lengths are nondimensionalized with the radius of the frozen droplet and plotted against the ambient vapor concentration. The gray and orange regions correspond to the theoretical values of nucleation dry zones (δ_N^*, Equation 7.2) and flux dry zones (δ_F^*, Equation 7.5), respectively. Any line running within and parallel to the gray or orange bands represents a given surface temperature where $c_w - c_i$ and SSD are fixed, such that δ_N^* and δ_F^* depend only upon c_∞. Here, a constant value of $SSD \approx 0.128$ for all temperatures was used to calculate δ_N^*, as indicated by our experimental observations (see Section 1 of Supporting Information). The upper and lower bounds of the orange band correspond to the minimum and maximum values of $c_w - c_i$ from our experiments, which were obtained at temperatures of $T_w = -12.5°C$ and $-30°C$, respectively. The experimental data points, collected from Figure 7.2b,d and color coded by the substrate temperature, universally fall within the orange region to suggest that the flux dry zone is always dominant ($\delta_{Cr}^* \sim \delta_F$). Inset: A simplified version of the same plot, where only $T_w = -25°C$ is considered. The dotted and the dashed blue lines represent nucleation dry zones corresponding to $SSD_{max} = 0.23$ and $SSD_{min} = 0.03$, as determined from. Comparisons of δ_{Cr} against theoretical values of δ_N and δ_F for all 12 choices of T_w are provided in Figure S5 of the Supporting Information. b) When rain droplets fell within the dry zone (first panel), they completely evaporated within seconds (second and third panels) while the droplets at the periphery of the dry zone remained unchanged in size.   78

List of Abbreviations and Symbols

a	Height of the monolayer-thick disk shaped embryo nucleating on ice [m]
A_{ij}	Contact area of phase i with phase j [m^3]
$A_{\parallel}$	In-plane projected area of the daughter drop [m^2] the area vector is parallel to the substrate
$A_{\perp}$	Out-of-plane projected area of the daughter drop [m^2] the area vector is perpendicular to the substrate
d	Twice the radius of curvature of the liquid droplet being harvested by its neighboring ice droplet
D	Diffusivity of water vapor in air [m^2/s]
g	Acceleration due to gravity [m/s^2]
h_{ij}	Specific enthalpy for phase change [J/mol]
H	Relative humidity in the ambient
I	Embryo formation rate [m^{-2}s^{-1}]
I_c	Critical embryo formation rate [m^{-2}s^{-1}]
I_0	Kinetic constant of nucleation [m^{-2}s^{-1}]
$J_{l,c}$	Mass flux condensing on the daughter drop [kg/m^2-s]
$J_{l,e}$	Mass flux evaporating from the daughter drop [kg/m^2-s]
k	Boltzmann constant [J/K]
k_{silane}	Thermal conductivity of silane monolayer [W/m-K]
$k_{silicon}$	Thermal conductivity of silicon wafer[W/m-K]
k_w	Thermal conductivity of water [W/m-K]
L	Length of ice bridge [m]
L_{exp}	Experimentally measured ice bridge length [m]
L_{max}	Maximum possible length of an inter-droplet ice bridge [m]
L_s	Length scale of condensing surface [m]

m	Cosine of contact angle
m_{bridge}	mass of inter-droplet ice bridge [kg]
m_l	mass of the liquid drop which is being harvested by its neighboring ice droplet [kg]
$\dot{m}_{i,c}$	Mass flow rate of vapor condensing on the ice drop [kg/m^2-s]
$\dot{m}_{l,c}$	Mass flow rate of vapor condensing on the daughter drop [kg/m^2-s]
$\dot{m}_{l,e}$	Mass flow rate of vapor emanating from the daughter drop [kg/m^2-s]
n	Number of mother droplets which are nearest neighbors to a daughter drop on a condensing surface
N_a	Avogadro's number
$p_{a,d}$	Actual supersaturated vapor pressure around a liquid droplet [Pa]
$p_{i,0}$	Saturation pressure of ice at $0°\,\mathrm{C}$
$p_{n,i}$	Supersaturated pressure required for nucleation on ice [Pa]
$p_{n,w}$	Supersaturated pressure required for heterogeneous nucleation on a substrate at temperature T_w [Pa]
p_s	Saturation vapor pressure [Pa]
$p_{s,d}$	Saturation vapor pressure of liquid water [Pa] corresponding to the droplet temperature T_d
p_{s_i}	Saturation vapor pressure of ice [Pa]
$p_{s_i,w}$	Saturation vapor pressure of ice at wall temperature [Pa]
p_{s_l}	Saturation vapor pressure of liquid water [Pa]
$p_{s_l,w}$	Saturation vapor pressure of liquid water at wall temperature [Pa]
p_t	Pressure at triple point [Pa]
p_∞	Ambient vapor pressure [Pa]
q	Amount of Heat flux flowing through the entire condensing surface [Watts/m^2]
q_d	Amount of Heat flux flowing through a droplet [Watts/m^2]
Q_d	Rate of heat transfer across the droplet [Watts]
r	radius of curvature of droplet [m]
r_d	Width of the monolayer-thick disk shaped embryo nucleating on ice [m]

r_m	Radius of curvature of mother droplets, which are pre-existing micron-sized or larger droplets on a condensing surface [m]
r^*	Critical radius of curvature of an embryo where nucleation is stable [m]
R	Universal gas constant [J/mol-K]
$\bar{R}$	Gas constant of water vapor [J/kg-K]
S	Supersaturation Ratio, $p_\infty/p_{s,w}$
SSD	Supersaturation Degree required for nucleation, $(p_{n,w} - p_{s,w})/p_{s,w}$
t_{silane}	Thickness of silane monolayer [m]
$t_{silicon}$	Thickness of silicon wafer[m]
T	Absolute temperature [K]
T_d	Temperature inside the droplet near vapor-droplet interface [K]
T_{DP}	Dew point temperature [°C]
T_i	Temperature at the vapor-ice interface [K]
T_t	Temperature at triple point [K]
T_w	Wall temperature [K]
T_∞	Ambient Temperature [K]

1

Introduction

"We come from the land
Of the ice and snow
From the midnight sun
Where the hot springs blow..."

$-Led\ Zeppelin$

The content of this chapter was previously published as a subsection of the journal manuscript in [14], and is reproduced here with minor modifications. This chapter discusses the different stages of condensation frosting as have been discovered recently, and chronologizes and contextualizes the research on frost phenomena up until now.

1

In 4th century BC, Aristotle wrote: [15]

> *Let us now deal with the most remarkable conditions which are produced in and around the earth, summarizing them in the barest outline... Dew is moisture of fine composition falling from a clear sky; ice is water congealed in a condensed form from a clear sky; hoar-frost is congealed dew...*

- Metereologica

It is astonishing to think that as early as two thousand years ago, Greek philosophers had such a remarkable understanding of condensation and phase change. Indeed, in this quote Aristotle correctly identifies the two possible modes of frosting – desublimation, which is a direct transformation of water vapor to ice, and condensation frosting, where the vapor first condenses into supercooled dew droplets that subsequently freeze [11, 16]. However it was not until 1657, fifteen years after Galileo's death, that the first systematic experiments on the freezing of water in an enclosed jar were performed to investigate Galileo's anti-Aristotelian claims that water when frozen becomes lighter than water itself [17].

We have come a long way since and yet we have not. Despite significant advances in the understanding of ice physics [12, 16, 18–32], we are far from solving the icing problem. From an economic standpoint, ice accretion today is a multibillion dollar problem in the United States alone [33]. Frosting and icing adversely affect multiple industries including aviation, telecommunication, electrical transmission, hydropower, wind power, oil rigs, and almost all modes of transportation [34]. Accumulation of ice on airplane wings can significantly alter the dynamic characteristics of aircraft flight, causing severe damage and even plane crashes [35–39]. Icing and frosting have also been shown to cause mechanical damage to helicopter blades and fuselage [40], pose severe safety hazard to offshore oil exploration platforms [41, 42], damage locks and dams [34, 43], and account for up to 40% of road accidents in winter [39, 44, 45]. Frost accumulating on refrigerators and heat exchangers can reduce their heat transfer efficiency by as much as 50–75% [39, 46, 47]. Frosting can also cause mechanical damage to power transmission line systems as well as induce electric faults, such as flashovers, due to insufficient clearances [39, 48–50]. On wind turbines, it has been shown that ice accretion can substantially reduce the aerodynamic efficiency and torque, causing power losses as high as 50% [51, 52].

As recently as a few years ago, the underlying mechanism of condensation frosting was considered to be equivalent to that governing icing, namely that supercooled droplets freeze in isolation by heterogeneous nucleation at the solid-liquid interface [53–56]. From this false perspective, the difference between icing and frosting is merely contextual: the supercooled water is deposited for icing and nucleated for condensation frosting. However, it has recently been discovered that heterogeneous ice nucleation is the dominant mechanism only in the case of icing, but not for condensation frosting. The true dominant mechanism of condensation frosting on

hydrophobic and mildly hydrophilic surfaces is that of inter-droplet ice bridging, where frozen droplets grow ice bridges towards their neighboring liquid droplets to form an inter-connected ice network [5, 6, 57].

The aim of the present work is to understand the physics of frost incipience at a microscopic level that has been largely overlooked until the past several years [5, 6, 57–61]. Here we show how the phenomenon of ice bridging, along with other intriguing associated phenomena such as frost halos [4, 62] and dry zones [9, 10, 63], constitute the incipient stages of condensation frosting and fundamentally differentiate the physics of frost growth from ice growth. We investigate each of these phenomena in separate chapters, with extensive experiments and scaling analysis to understand the underlying mechanism behind these phenomena. Finally we discuss how strategies developed in circumventing the icing problem do not necessarily translate to the frosting problem. Drawing from our our newly formed understanding of frost growth at the microscopic level, we propose possible means of delaying or even halting in-plane frost growth by inhibiting one or more of the incipient stages of frost formation.

2

Background Information

"Oh oh oh you'd better cool it down
You know you'd better cool it down..."

− The Velvet Underground

The content of this chapter was previously published as a subsection of a journal manuscript in [14], and reproduced here with minor modifications. This chapter discusses the different stages of condensation frosting as have been discovered recently, and chronologizes and contextualizes the research on frost phenomena up until now.

Stages of Condensation Frosting

There are five prominent stages of condensation frosting: I) supercooled condensation, II) onset of freezing, III) frost halos, IV) inter-droplet ice bridging and dry zones and V) percolation clusters and frost densification. Figure 2.1 shows the chronological order of the stages with illustrative schematics of the various phenomena. We will now elaborate on each stage in order.

2.1   Stage I – Supercooled Condensation

The first stage of condensation frosting is the formation of supercooled condensation on a substrate. Broadly, condensation is a two-step process comprised of: a) heterogeneous nucleation on a substrate and b) subsequent growth (which itself is a multi-step process which will be detailed at the end of this section).

A necessary (but not sufficient) condition to have heterogeneous nucleation on a substrate is that the temperature of the substrate must be beneath the dew point. The dew point temperature is defined as the saturation temperature corresponding to the partial pressure of water vapor in the ambient. As such, at the dew point temperature, ambient water vapor and liquid water have the same chemical potential and are in thermodynamic equilibrium. However, nucleation involves creation of new interfaces which necessitates a certain degree of supersaturation in the ambient atmosphere. The extent of supersaturation necessary for heterogeneous nucleation can be determined by equating the Gibbs free energy change ΔG of a nucleating embryo to the change in free energy associated with supersaturation (Figure 2) [7, 11]. For a nucleating embryo of radius r_e, ΔG can be expressed as a summation of the negative change in energy inherent to supersaturated vapor becoming liquid/ice (ΔG_v) and the positive energy barrier associated with the creation of the interfaces (ΔG_s) (Figure 2.2). If the ambient vapor pressure is supersaturated beyond a certain limit it is possible that the vapor directly transforms to ice on the substrate bypassing the liquid phase (desublimation). We will discuss the thermodynamics and phase stability of the different modes of nucleation in further detail in the next chapter.

The nucleation energy barrier for embryo formation ΔG is much larger for hydrophobic surfaces than for hydrophilic surfaces. Thus, a chemically heterogeneous surface exhibiting both hydrophobic and hydrophilic features, would have preferential nucleation events only within the hydrophilic patterns. In fact, in the last decade, wettability patterning has been successfully utilized to promote preferential condensation and increase condensation heat transfer [64–68], enhance water harvesting [69–71], or to control icing/frosting behavior [72, 73].

After nucleating, the supercooled water droplets keep growing from the ambient vapor. The growth of condensate shows several remarkable features which have been studied in depth by Beysens and others [74–80]. There are three significant stages in droplet growth on a 2D substrate. The first is the isolated growth regime, where the droplets have just nucleated and are sufficiently far from each other, such that the
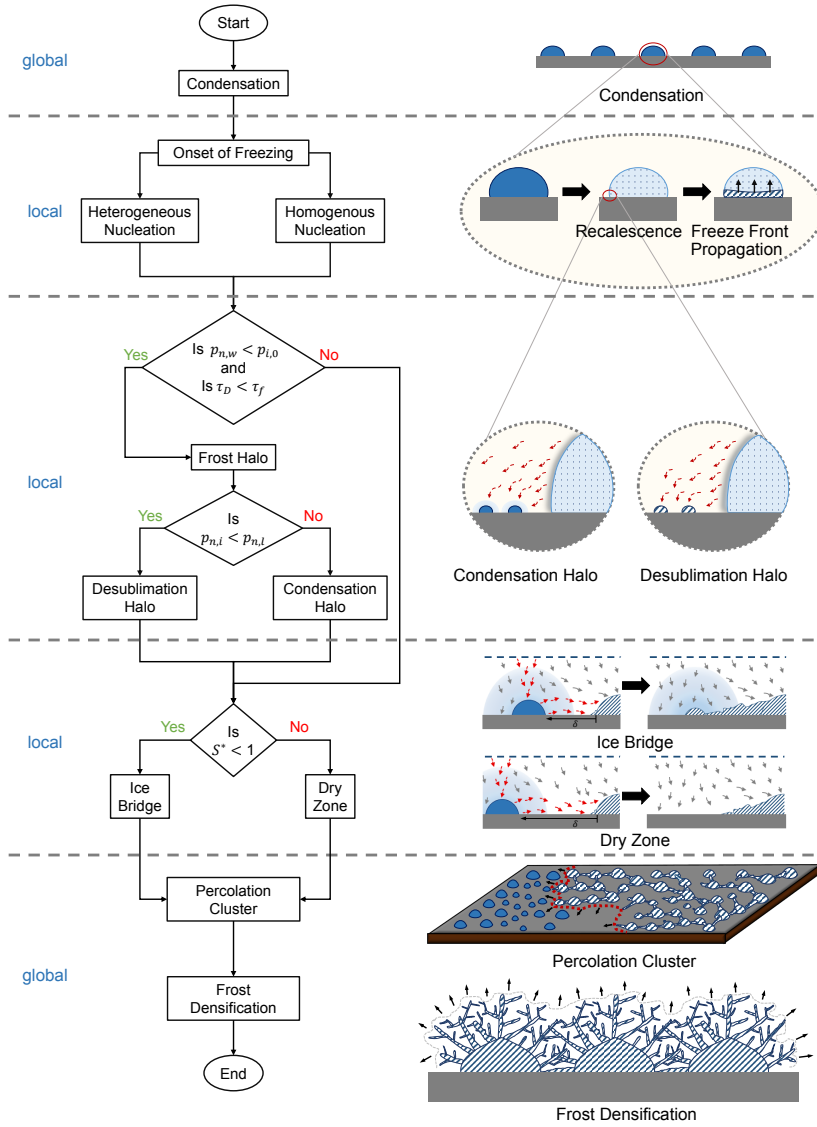
FIGURE 2.1: The different stages of condensation frosting. The word 'local' implies that the given phenomenon is microscopic, that is, specific to either a single droplet or constitutes a droplet pair interaction. The word 'global' implies that the phenomenon is macroscopic and requires the participation of the entire condensate population. The relevant vapor pressures are the pressure required to nucleate a water/ice embryo on a surface with a given wall temperature $(p_{n,w})$, the saturation vapor pressure with respect to ice at 0°C $(p_{i,0})$, and the nucleation pressures corresponding to the condensation mode $(p_{n,w} = p_{n,l})$ or desublimation mode $(p_{n,w} = p_{n,l})$. The time scale of thermal conduction through ice is labeled τ_f while τ_D is the time scale of vapor diffusion from the ice droplet. Length scales include the distance between a frozen droplet and a neighboring water droplet (δ) and the critical dry zone length around a frozen droplet (δ_{Cr})

6
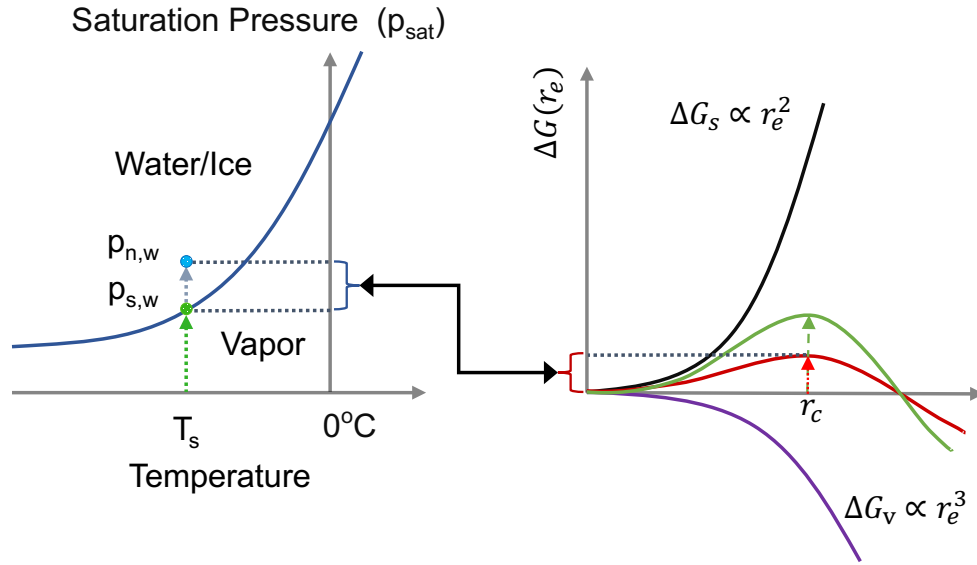
FIGURE 2.2: Left: p-T diagram showing the extent of supersaturation required to nucleate an embryo of water or ice. Right: schematic of Gibbs free enthalpy variation (ΔG) with the radius of the nucleating embryo (r_e). The green curve corresponds to homogneous nucleation, while the red curve corresponds to heterogeneous nucleation. Note the enthalpic requirement associated with supersaturation (blue bracket) equals the critical Gibbs free enthalpy change (red bracket).

pressure profiles about each droplet do not overlap. The vapor pressure distribution about each droplet follows a hyperbolic profile $p = p_\infty - (p_\infty - p_l)R/r$, where p is the vapor pressure at a distance r from the center of the droplet, p_∞ is the vapor pressure in the ambient atmosphere, p_l is the vapor pressure at the liquid-vapor interface and R is the radius of the liquid droplet. In this regime, under a steady state of condensation, each droplet grows in time as $R \sim t^{1/2}$. As the droplets grow larger, the dynamics of droplet growth transition to the second regime. The pressure profiles about each droplet now overlap, resulting in a pressure gradient that is effectively linear and out-of-plane such that the droplet pattern can be treated as a homogeneous film. Analytically, the pressure field can be expressed as $p = p_l + (p_\infty - p_l)(z - h)/\zeta$, where z is the distance perpendicular to the substrate, h is the average thickness of the homogeneous film that approximates the droplet distribution, and ζ is the concentration boundary layer thickness. In this regime, the droplet radius evolves as $R \sim t^{1/3}$. Over time, a plethora of coalescence events lead to a third, accelerated growth regime that is self-similar and characterized by a constant surface coverage. The growth law follows $R \sim t$ as long as the film approximation discussed in the second regime remains valid. Note that the above expressions of pressure profiles are valid only under isothermal conditions, that is, as long as the ambient temperature is not significantly different from that of the substrate. Otherwise, they should be
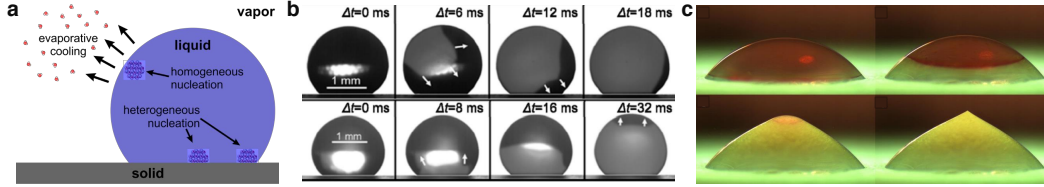
FIGURE 2.3: (a) Schematic depicting the two possible modes of ice nucleation in a water droplet: heterogeneous nucleation and homogeneous nucleation. [1] (b)Top row: Homogeneous nucleation originating at the liquid-vapor interface followed by freeze front propagation in a supercooled sessile droplet. Bottom row: heterogeneous nucleation originating at the solid-liquid interface followed by freeze front propagation in a supercooled sessile droplet [1, 2]. Reprinted (adapted) with permission from [54]. Copyright 2014 American Chemical Society. (c) The freezing of a water droplet ends in a tip singularity. [3] Reprinted (adapted) with permission from [126]; copyright 2012 American Institute of Physics.

replaced by their corresponding vapor concentration values.

2.2 Stage II – Onset of Freezing

The second stage of condensation frosting is the onset of freezing in the supercooled condensate. Even if the substrate is at a subfreezing temperature, freezing does not initiate immediately after condensation ensues. This is because freezing, just like condensation, requires a certain degree of subcooling to overcome the free energy barrier associated with the formation of new interfaces. Supercooled liquid water can in fact remain metastable at temperatures as low as $T_w \approx -40\,^\circ\text{C}$ without freezing right away [21].

Freezing of condensate droplets on a substrate starts with a probabilistic nucleation event. This nucleation can either be homogeneous if it initiates within the droplet away from the solid substrate, or heterogeneous if it starts at the solid-liquid interface (see Figure 2.3a). The preferred mode of nucleation at any given condition corresponds to the one that has a lower enthalpic requirement. The Gibbs free energy barrier for heterogeneous nucleation ΔG_{het} is usually lower than that for homogeneous nucleation ΔG_{hom}. As such, heterogeneous nucleation at the solid-liquid interface is usually the preferred mode of nucleation. However, it has recently been shown that unsaturated gas flow conditions can induce homogeneous nucleation at the free surface of a supercooled droplet due to evaporative cooling [2].

The delay in heterogenous nucleation at the solid-liquid interface can be obtained from the embryo formation kinetics, following classical nucleation theory. Assuming that the freezing events occurring in a condensate population are random and uncorrelated for any given nucleation rate, the random freezing events can be considered to constitute an inhomogeneous Poisson process [81]. Therefore if a substrate is cooled from a temperature T_0 to T_w and $\alpha = dT/dt$ is the rate of cooling, then

the probability of freezing N_f number of droplets in an ensemble of N_0 droplets after time t is given by

$$P(N) \equiv \frac{N_f}{N_0} = 1 - \exp\left(-\alpha^{-1} \int_{T_o}^{T_w} J(T)dT\right), \tag{2.1}$$

where $J(T)$ is the ice nucleation rate per unit time (s^{-1}). Therefore, $J(T) = I(T)A$, where $I(T)$ is the embryo formation rate per unit area per unit time (m^{-2}s^{-1}) and A is the solid-liquid surface area. From Becker-Döring embryo formation kinetics, I can be expressed as [82, 83]

$$I = I_0 \exp\left(-\frac{\Delta G}{kT}\right), \tag{2.2}$$

where I_0 is the kinetic prefactor accounting for the diffusive flux of water molecules across the ice interface, ΔG is the total change in free energy corresponding to nucleation, and $k = 1.38 \times 10^{-23}$ J/K is the Boltzmann constant. The change in free energy is expressed as $\Delta G = 16\pi\sigma^3 f/3\Delta\tilde{g}^2$, where f is a geometrical factor that takes into account the roughness and wettability of the substrate, σ is the water-ice interfacial energy per unit area, and $\Delta\tilde{g}$ is the Gibbs energy change per unit volume. Thus, we see that the nucleation delay is a function of substrate temperature, wettability and surface roughness. This is succinctly condensed in the following equation: if α is a constant then for a given substrate temperature T, the expected delay in nucleation time $\langle\tau\rangle$ is given by [84]

$$\langle\tau\rangle = \frac{1}{J(T)}. \tag{2.3}$$

By increasing the nucleation energy barrier, one can decrease the nucleation rate and consequently delay freezing substantially for deposited or condensed supercooled water. The nucleation energy barrier increases with larger contact angles of the water which serves to increase $I(T)$ while also decreasing A for a droplet of fixed volume. In the extreme case of superhydrophobic surfaces where supercooled droplets exhibit a suspended Cassie state [85], the decrease in A is much more dramatic due to the presence of air pockets replacing much of the solid-liquid interface. Therefore the freezing of supercooled droplets can be significantly delayed or in some cases even prevented by maximizing the hydrophobicity of a substrate. This is precisely the idea that has provided the connective tissue between the fields of icephobicity and superhydrophobicity over the past decade of research [1, 39, 58, 86–101]. For cases where the deposited droplet is initially warmer than the chilled substrate, the superhydrophobic Cassie state also serves to minimize conductive heat transfer between the droplet and substrate to prolong freezing onset [54, 102]. The low hysteresis of supercooled superhydrophobic (or liquid-infused) surfaces also facilitates the dynamic removal of supercooled droplets by rebound or sliding before ice nucleation can occur. [95, 103–107] On some nanostructured superhydrophobic surfaces, even

supercooled condensation can be removed prior to freezing via coalescence-induced jumping [6, 108].

In a few special cases, it has been shown that increasing hydrophobicity or promoting the Cassie wetting state are not always optimal. For example, hydrophobic surfaces can actually exhibit an inferior freezing delay compared to ultrasmooth hydrophilic surfaces in cases where the benefit of the decreased wettability is outweighed by the disadvantage of increased surface roughness (which increases A and/or nucleation-promoting defects) [94, 109]. A thermodynamic analysis by Eberle et al. recently showed that for ultrafine nanoroughness, the tendency of the roughness to promote ice nucleation for impaled supercooled droplets can be counteracted by the confinement of the interfacial quasiliquid layer, delaying freezing by as long as 25 hours under proper conditions. On such a surface, impaled Wenzel droplets could remain in the supercooled liquid state longer than suspended Cassie droplets.

Ice nucleation is followed by two partially overlapping stages of freezing: a) recalescence and b) freeze front propagation [2]. Recalescence is the very rapid (kinetically controlled) first stage of freezing where the growth of the ice embryo leads to an explosive release of latent heat, raising the temperature of the supercooled liquid to the equilibrium freezing temperature– 0°C [110–113]. The recalescent phase transforms the liquid droplet to a slushy matrix of partially solidified liquid, typically in the order of ~ 10 ms for milimetric droplets [4]. This is followed by a significantly slower isothermal freeze front propagation where the liquid in the interstitial space of the ice scaffold is completely frozen. The second stage of freezing is governed primarily by the rate at which the latent heat is conducted into the substrate and/or dissipated in the ambient. As such, the duration of the second stage of freezing may vary from fractions of a second to tens of seconds depending on the thermal conductivity of the underlying substrate. Figure 2.3b shows experimental images of homogeneous and heterogeneous nucleation in deposited supercooled droplets and the subsequent freeze front propagation that follows.

For the case of heterogeneous nucleation, the freezing of a water droplet eventually ends in a beautiful tip formation at the top [114, 115] (Figure 2.3c). This tip singularity is a consequence of the expansion of water upon freezing and the fact that the top of a droplet is the last portion to freeze for heterogeneous nucleation. Intriguingly the cone angle at the tip of a frozen droplet is a constant $139°\pm 8°$, independent of the substrate temperature, droplet size, and wettability [114].

2.3   Stage III – Frost Halos

This third stage of condensation frosting (frost halos) partially overlaps with the second stage, that is, the onset of freezing. This is because the phenomena of frost halos initiates after recalescence [4]. During the recalescent stage of freezing, the temperature of the droplet quickly increases from its supercooled temperature T_w to 0°C [110–113, 116]. This leads to an explosive evaporation from the freezing liquid
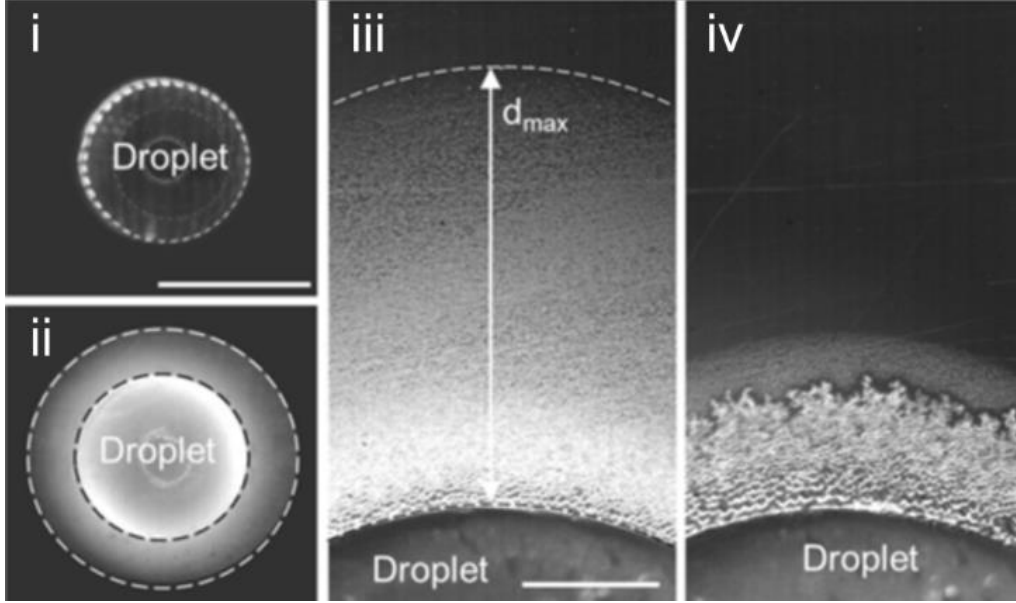
FIGURE 2.4: (a) Condensation halo surrounding a freezing $5\,\mu$L droplet on a PMMA [poly(methylmethacrylate)] substrate [4]. Reprinted with permission from [48]. Copyright 2012 National Academy of Sciences.

droplet. This vapor manifests itself as an annular ring of condensate microdroplets around the frozen droplet that can quickly freeze over, hence the designation of frost halos (Figure 2.4a). Jung et al. [4] show that the phenomenon of frost halos depends on how long the droplet stays at 0°C, and thus can be controlled by tuning the conductivity of the substrate. If the substrate is sufficiently insulating, then the time required for the droplet to cool down to the substrate temperature after freezing τ_f can be much greater than the diffusion time scale τ_D, which is the time taken by the emanated vapor to diffuse out and condense in an annular ring around the droplet.

In Chapter 4, we theoretically study the underlying mechanism of the frost halos and show how it is governed by the wettability of the substrate as well as the competition between the freezing and diffusion time scales. We also the posit the possibility of a desublimation where the emanated vapor directly transitions directly to ice on the substrate.

2.4   Stage IV – Inter-droplet Ice Bridging and Dry Zones

The fourth stage of condensation frosting is essentially what differentiates it from the icing problem, yet eluded researchers until the past five years. It was long believed that each condensate droplet freezes in isolation due to heterogeneous or homogeneous nucleation without interacting with neighboring droplets [53–56]. This
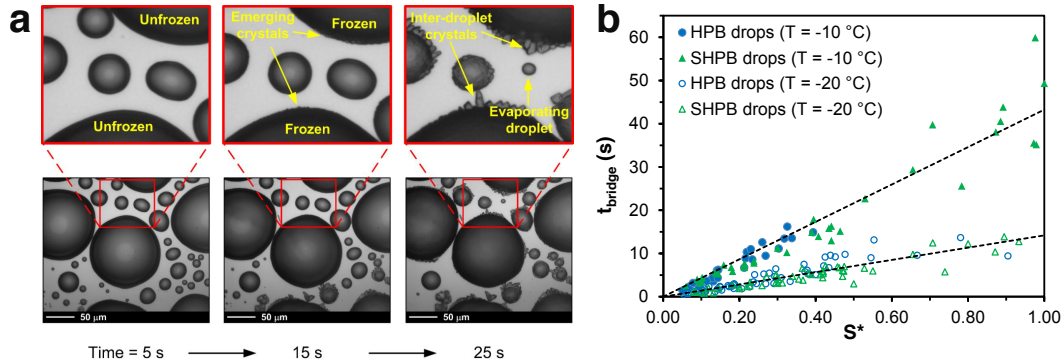
FIGURE 2.5: (a) First reported observation of inter-droplet ice bridging [5] driving frost growth across supercooled condensate on a substrate. The substrate temperature was $T_w = -10\,^\circ\text{C}$, the air temperature was $T_{air} = 5.1\,^\circ\text{C}$, and the relative humidity was $RH = 65.4\%$. Each image in the top row is a 50X magnification of the region marked in red in the bottom image. Reprinted with permission from the Ph.D. thesis of J.B. Dooley, [45]. (b) Time taken for ice bridges to connect to their targeted droplets on hydrophobic (HPB) or superhydrophobic (SHPB) surfaces as a function of the separation parameter, S^* [6]. Reprinted with permission from [46]; copyright 2013, American Chemical Society.

is true for temperatures below -40°C where the delay in nucleation time is negligible and almost all the droplets freeze simultaneously [21]. However, for temperatures higher than -40°C, the vast majority of the droplets do not freeze in isolation but rather are frozen by inter-droplet interactions.

In a population of supercooled condensate, which droplet freezes first is a probabilistic event. The droplets that freeze first have a lower vapor pressure above them owing to the fact that the saturation vapor pressure over ice is lower than that over water at the same subfreezing temperature [20]. This leads to localized vapor pressure gradients in the system where the frozen droplets start behaving as local humidity sinks. The source-sink interaction between the frozen droplets and their neighboring water droplets lead to the fascinating phenomena of inter-droplet ice bridging [5, 6, 57] and localized dry zones [9] which are the hallmarks of condensation frosting on hydrophobic surfaces. Note that inter-droplet ice bridging and dry zones are specific to surfaces which exhibit dropwise condensation. Sufficiently hydrophilic surfaces exhibit filmwise condensation and the film freezes over all at once [56].

Once a droplet freezes and equilibrates to the temperature of the substrate, the vapor pressure above it becomes lower than that over the water droplets surrounding it [20]. If there is frost halo around the frozen droplet then the microdroplets in the halo that are nearest to the ice droplet start evaporating [4]. In the absence of a frost halo, the frozen droplet starts harvesting water molecules from its nearest neighboring water droplets [5, 6, 57]. These water molecules deposit on the frozen

droplet and start growing ice bridges directed towards the water droplets that are being harvested. The neighboring liquid droplets freeze as soon as the ice bridges connect. These newly frozen water droplets now start harvesting water from their adjacent water droplets and grow ice bridges towards them. Thus frost propagates in a chain reaction of inter-connected ice bridges that form a network. The phenomenon of inter-droplet ice bridging in the context of condensation frosting was first reported by J. B. Dooley in his Ph.D. thesis in 2010 [5]. Using a SiAl substrate chilled to $T_w = -10°C$, Figure 2.5a shows the the first observation of inter-droplet ice bridging across a population of supercooled condensate. Note that in these image sequences, the frost halos are not visible, most likely because the experimental conditions were not conducive for them.

The discovery of the phenomenon of inter-droplet ice bridging brings forward a plethora of unanswered questions. When and how to ice bridges form? What drives the growth of these bridges? How does it depend on the temperature of the substrate, ambient humidity? Does it depend on the interacting droplet sizes? In Chapter 5, we thoroughly investigate the phenomenon of ice bridging, and try and answer some of these questions.

In our attempt to investigate ice bridges we found out that an ice bridge is not guaranteed to connect to the water droplet it is harvesting. This leads to the formation of dry zones around frozen droplets, and such dry zones can be as large as 1mm. The hygroscopic nature of which drives the formation of ice bridges can thus be simultaneously be responsible for spreading of frost or its inhibition by creating dry zone. In Chapter 6, we study the phenomenon of dry zones specifically, which leads us to some broader questions on the underlying mechanism of hygroscopic droplets and thee dry zones they form. We find that there exists a universal scaling law which captures the essential physics governing dry zone formation around droplets of different sizes under different ambient and substrate conditions. Subsequently, in Chapter 7, we demonstrate how thee hygroscopic property of ice can be harnessed in combatting frost itself.

2.5   Stage V – Percolation Clusters and Frost Densification

In a population of supercooled condensate, disparate droplet sizes and inter-droplet distances, after the first freezing event, ice bridges percolate globally through the entire population in a chain reaction [6, 9, 61, 117–120]. Such percolation clusters are characterized by local regions of ice bridge connections and dry regions. Figure 2.6a shows the final footprint of the chain reactions of ice bridging that are inherent in any percolating cluster of inter-droplet ice bridges. The velocity of propagation of such an inter-droplet global freeze front is typically of order 1–10μm/s [6, 57]. This growth rate has been shown independent of substrate stiffness [120]. It has also been shown that the global propagation of ice bridges can be suppressed by incorporation of three-dimensional microscale structures with inclined edges on a hierarchical
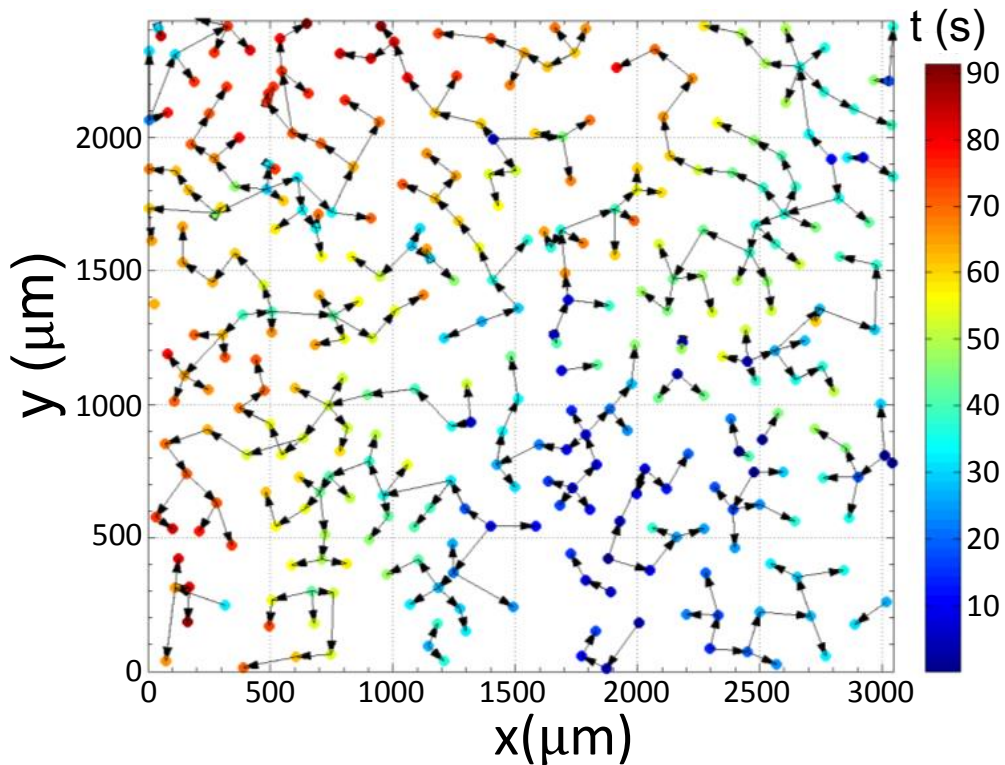
FIGURE 2.6: Inter-droplet freezing pathlines indicating in-plane ice bridge connections over time. The color contour shows the time elapsed while the arrows show the direction of propagation of individual ice bridges in the percolation cluster. Substrate temperature $T_w = -7.1°C$, air temperature $T_{air} = 5°C$ and relative humidity $RH = 64.9\%$. Reprinted with permission from the thesis J.B. Dooley, [45].

superhydrophobic surface. Microscale structures create a structural barrier for ice bridging, diminishing their global propagation rates. [61].

In Chapter 5, we show how the velocity of a global freeze front can be tuned by controlling the inter-droplet distances between the droplet. Note that the percolation process inherent to inter-droplet ice bridging is different from the growth of an isolated snow crystal at the expense of the ambient vapor. Unlike the morphology of snow crystals, that often exhibit self-similar fractal characteristics in their dendritic growth, inter-droplet ice bridging shows very specific preferential growth in the direction of the nearest neighboring water droplet that is harvested. Once the global freeze front has propagated though the entire condensate, a network of interconnected frozen droplets provide the footprint upon which out-of-plane frost growth can happen. The thermodynamics of frost densification has been studied in extensive detail for decades and has many excellent reviews and articles [11, 121–140].

3

Phase Stability

"Break on through to the other side
Break on through to the other side"

− The Doors

3.1 Introduction

Anyone who has put a lid on a coffee cup and looked at the droplets condensing underneath has observed an annular dry zone around each droplet where no new droplets appear. One possible mechanism for these apparent dry zones surrounding condensing droplets is the cooperative diffusion governing dropwise condensation, in which the out-of-plane diffusion of vapor towards the substrate is coupled with an in-plane exchange of vapor between droplets [142]. The in-plane pressure gradients are due to the diversity of droplet sizes on the condensing surface, as nanometric droplets exhibit a highly supersaturated vapor pressure due to their curvature while micrometric droplets are approximately saturated. Therefore when smaller droplets are proximal to a larger droplet, the in-plane pressure gradient driving the evaporation of these smaller droplets can dominate the out-of-plane differential driving their growth, creating a dry zone around the large droplet [63]. Another mechanism for dry zones is that nucleation itself can be suppressed around pre-existing droplets, as the critical vapor pressure to form an embryo is larger than the (near saturated) equilibrium pressure over large droplets [143, 144].

While the case of all-liquid droplets requires disparities in droplet sizes to produce inter-droplet pressure gradients, an ice droplet exhibits a lower pressure than a supercooled liquid droplet even when both droplets are same-sized. This inherent pressure differential between frozen droplets and liquid droplets is because ice has a lower saturation vapor pressure than supercooled water at the same temperature [20]. Ice is therefore a humidity sink for both nanometric (supersaturated) liquid droplets and larger (saturated) liquid droplets. As an ice droplet siphons water vapor from neighboring liquid droplets, this harvest of water molecules manifests itself as ice bridges growing from the frozen droplet toward the evaporating liquid droplets [5, 6, 57]. The liquid droplets being harvested will freeze as soon as the ice bridges connect; these newly frozen droplets will in turn grow ice bridges to the next row of supercooled condensate, thus propagating frost across the surface. Inter-droplet ice bridging is now thought to be the dominant mechanism for condensation frosting on hydrophobic [6, 57, 120] and superhydrophobic [6, 59, 61, 118, 119, 145] surfaces chilled beneath the dew point, as only a single droplet needs to freeze due to heterogeneous nucleation for the chain reaction of ice bridges to occur.

Very recently, we have shown that a stable dry zone can exist around a frozen droplet when the nucleation sites for supercooled condensation are sufficiently sparse and/or the freezing event occurs during the early growth of the condensate [63]. Under these conditions, the droplets are small and sparse, such that the liquid droplets being harvested by a frozen droplet will completely evaporate before the ice bridges can connect [63]. Therefore it is evident that the pressure gradient between ice and water can be used for the dual purposes of spreading frost or creating dry zones, depending upon the conditions of the system. In addition to using ice, it is also possible to create dry zones around humidity sinks by utilizing hygroscopic liquids such as salty water [9, 80, 146], nectar [147], or glycols [10] in conjunction with the

16

growth of condensation and/or frost. However, in these cases the depression in vapor pressure of the hygroscopic droplet(s) with respect to condensation/frost decays to zero as the hygroscopic droplets become increasingly diluted with the harvested water vapor.

Though the saturation vapor pressure of ice is always lower than water under isothermal conditions, interestingly this pressure gradient can flip when considering the initial freezing of a supercooled liquid droplet. During the first stage of freezing, known as recalescence, the rapid ($\sim 10\,\text{ms}$) formation of an ice-crystal scaffold causes the droplet to quickly heat up to approximately $0\,^\circ\text{C}$ due to the sudden input of latent heat [4]. Until this latent heat is dumped into the ambient via evaporation and into the substrate by conduction, the freezing droplet is therefore warmer than its supercooled liquid neighbors. This can be sufficient to elevate its vapor pressure above that of the water droplets. Indeed, the pressure increase induced by recalescence can cause vapor to emanate from the frozen droplet such that satellite droplets nucleate on the substrate around the droplet, which subsequently freeze over via inter-droplet ice bridging to form what is known as a frost halo [4, 62].

It should now be clear that localized, inter-droplet vapor pressure gradients are responsible for a variety of emerging phase-change phenomena such as dry zones, condensation frosting, and frost halos. However, to date most reports on these topics have been primarily experimental, and much remains to be understood regarding the thermodynamics of the pressure gradients driving these phenomena. For example, to model the pressure difference between nucleating droplets and pre-existing droplets, one must calculate the critical vapor pressure required for embryo nucleation. Yet reports that have quantified the supersaturation required for nucleating liquid or ice embryos have produced contradictory results that do not agree with each other (see Supporting Information Figures S1 and S2) [7, 11–13]. To complicate matters even further, these previous studies estimating nucleation pressures used single values for the kinetic constant of nucleation ($I_0 \sim 10^{29}\,\text{m}^2\text{s}^{-1}$) and the critical embryo formation rate for nucleation to occur ($I_c \sim 10^4\,\text{m}^2\text{s}^{-1}$) [83, 148], despite their exact values being uncertain with I_0/I_c spanning at least 3 orders of magnitude [12, 149]. To additionally estimate the supersaturation required to grow an embryo on pre-existing ice (i.e. frost growth), the study by Na and Webb [7] applied the same value of $I_o/I_c \sim 10^{25}$ used for nucleation on a dry surface, but this assumption that the ratio is the same for an ice substrate is highly questionable. Indeed, there is a sharp disagreement in the literature regarding whether the vapor pressure required for frost growth is to be considered as saturated [11, 124–126, 133, 150] or supersaturated [7, 16, 121, 123]. Considering that the emerging phenomena discussed above are typically driven by highly sensitive in-plane pressure gradients (i.e. extremely small relative to the out-of-plane pressure gradients), an improved understanding of the pressure field around nucleating and pre-existing water and ice droplets on the substrate is required to accurately model these systems.

Here, we utilize a synergistic blend of classical nucleation theory, quasi-steady diffusive growth models, and experimental results to develop a comprehensive model of

17

the contrasting vapor pressures around nucleating and pre-existing water/ice droplets and how they govern various condensation and frost phenomena. First, we calculate the critical pressure for embryo formation on a dry substrate as a function of temperature, surface wettability, and embryo formation rate. In contrast to Na and Webb's assertion that condensation is always thermodynamically favorable compared to desublimation [7], here we show that the preferred mode of embryo nucleation can switch between condensation and desublimation, depending upon the temperature and wettability of the surface. By varying the value of the I_0/I_c ratio by 3 orders of magnitude for all calculations, it is concluded that the uncertainty in this ratio can appreciably affect the nucleation pressures for some of the parameter space.

3.2 Model Formulation

3.2.1 Saturation Vapor Pressure

The primary mechanism for local vapor pressure gradients in a vapor-water-ice system is the difference in the saturation vapor pressures of water versus ice. The Clausius-Clapeyron equation shows how the saturation pressure (p_s) between two phases i and j relates to the absolute temperature (T) and the change in specific enthalpy associated with phase-change ($h_{ij}(T)$). This is given by:

$$\frac{\mathrm{d} \ln p_s}{\mathrm{d}T} = \frac{h_{ij}(T)}{RT^2},$$
(3.1)

where R is the universal gas constant. This relation can be integrated to obtain the saturated vapor pressures of water or ice at different temperatures using the vapor pressure at the triple point ($p_t = 611.657 \pm 0.01 \, \text{Pa}$, $T_t = 273.16 \, \text{K}$) as a boundary condition [151]. Also, the latent heat in Eq. 3.1 needs to be taken as a function of temperature. In a seminal review paper, Murphy and Koop discuss how the variation of molar heat capacity with temperature affects the latent heat in subzero temperatures and in turn the saturation pressures [20]. Incorporating these variations of h_{ij} with temperature, we have plotted the saturation pressure of vapor over water or ice in Figure 3.1. The saturation vapor pressure over ice is lower than that over water for all temperatures below $0 \, ^\circ\text{C}$. By itself, this is sufficient to create a vapor pressure gradient in a vapor-water-ice system that can cause vapor to flow preferentially from water towards ice. There are, however, other factors that can significantly influence the pressure differential and in some cases even reverse its direction altogether, which we discuss in the following sections.

3.2.2 Supersaturation – Nucleation on a Dry Substrate

The saturation pressure of vapor over water or ice at a given temperature, by definition, is the pressure at which the water/vapor or ice/vapor phases have the same chemical potential and are therefore in thermodynamic equilibrium. However, for

18
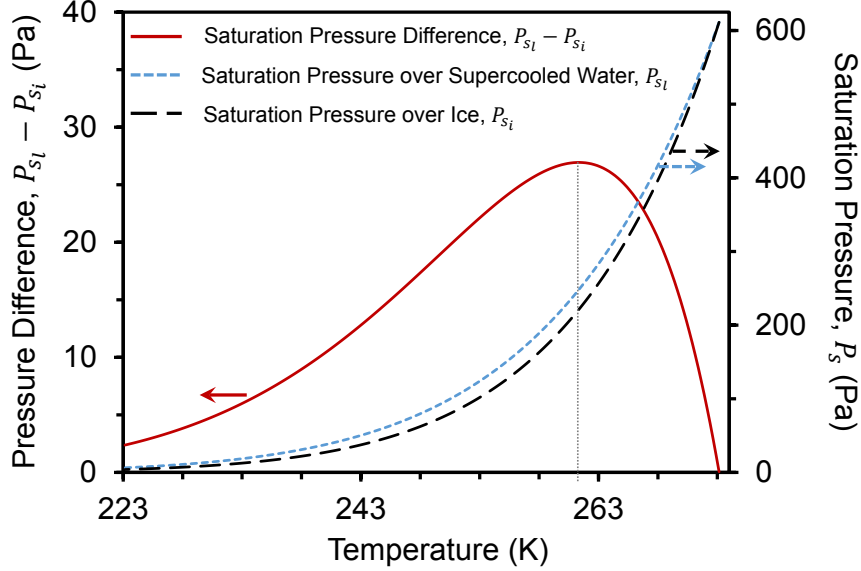
FIGURE 3.1: Saturation pressure of vapor with respect to supercooled water (blue line, right y-axis) or ice (black line, right y-axis) as a function of temperature. Note that the difference in vapor pressure between saturated water and ice (red line, left y-axis) peaks at approximately $\Delta p \approx 27\,\text{Pa}$ at $-12°$ C, as denoted by the dotted lines. Analytical expressions for these curves are available in the Supporting Information (Equations S1$-$S4).

phase-change processes such as condensation or desublimation to occur, they often require vapor pressures that exceed the saturation pressure, known as supersaturation. The supersaturation of water vapor is thermodynamically metastable up to a certain limit because condensation and desublimation both involve nucleation, that is, the creation of new interfaces that are energetically costly [16, 149]. The amount of free enthalpy required for nucleation is dependent on whether the nucleation event is homogeneous or heterogeneous. Homogeneous nucleation has been addressed in considerable depth in the fields of cloud physics and atmospheric sciences [152, 153]. For this reason, and also because the phenomena of dry zones, ice bridging, and frost halos are generally intrinsic to substrates, we limit ourselves here to the case of heterogeneous nucleation. Note that in the present discussion we have not considered the non-continuum transport effects that have been studied in previous works [154–156], which if considered would not change the formulation, but use a different value of surface tension. We will first consider the case of new water/ice embryos nucleating on a dry portion of the substrate.

Consider an embryo of radius of curvature r that nucleates upon a substrate exhibiting a wall temperature T_w (Figure 3.2a), such that the saturation vapor pressure corresponding to the wall temperature would be $p_{s,w}$. Recall from Figure 3.1 that this saturation pressure will be slightly larger for liquid embryos ($p_{s_l,w}$) versus ice
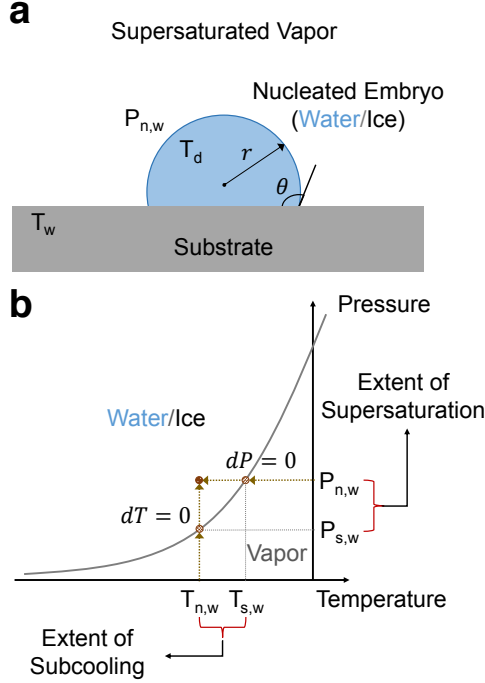
FIGURE 3.2: (a) Schematic of an embryo nucleating on a substrate by condensation or desublimation at a supersaturated vapor pressure ($p_{n,w}$). (b) p-T diagram showing the extent of supersaturation (or subcooling) required to nucleate an embryo of water or ice.

embryos ($p_{s_i,w}$). Since we are restricting ourselves to the cases of condensation or desublimation, it is a necessary but not sufficient condition that the surface is beneath the dew point ($p_\infty > p_{s_l,w}$, for condensation) or beneath the frost point ($p_\infty > p_{s_i,w}$, for desublimation) for nucleation to occur, where p_∞ is the partial pressure of water vapor in the ambient. The size of nucleating embryos is typically of order $r \sim 1 \, \text{nm}$ [149], such that conductive losses are negligible and it can be assumed that $T_d \approx T_w$, where T_d is the temperature inside of the droplet near its liquid-vapor interface.

Figure 3.2b shows the p–T diagram corresponding to the nucleation process. When the temperature of the substrate is fixed at T_w, the vapor pressure at the wall can increase along the $dT = 0$ path until nucleation occurs at a supersaturated vapor pressure: $p_{n,w} > p_{s,w}$ (vertical arrows in Figure 3.2b). The critical supersaturation required for embryo formation can therefore be formulated as:

$$SSD = \frac{p_{n,w} - p_{s,w}}{p_{s,w}}, \tag{3.2}$$

where SSD is the abbreviation for the supersaturation degree and $SSD > 0$ indicates supersaturation. To avoid confusion in terminology, note that SSD describes the metastable supersaturation of water vapor that occurs locally at the surface to overcome the nucleation energy barrier [7, 11]. This is fundamentally different from

20

another commonly used supersaturation ratio, $S = p_\infty/p_{s,w}$, which quantifies the diffusive growth rate and nucleation density of condensation/frost on a given surface but cannot comment on nucleation energy barriers [67, 157, 158]. Therefore SSD, rather than S, is the proper context for discussing supersaturation in the present work. The specific Gibbs free energy change associated with the nucleation of the supersaturated water vapor molecules can be written as [16]:

$$\Delta\tilde{g} = -\frac{RT_w}{v}\ln\frac{p_{n,w}}{p_{s,w}}, \tag{3.3}$$

where v is the molar volume of water (for condensation) or ice (desublimation).

Instead of increasing the vapor pressure at a fixed wall temperature, an alternate path to nucleation is cooling the wall while holding the vapor pressure constant at p_w, with $T_{s,w}$ being the saturation temperature corresponding to p_w. For an initially dry surface, the wall temperature can be decreased beneath $T_{s,w}$ along the $dP=0$ path until nucleation occurs at the critical temperature $T_{n,w} < T_{s,w}$ (horizontal arrows in Figure 3.2b). $\Delta T = T_{n,w} - T_{s,w}$ may therefore be looked upon as the degree of subcooling required for nucleation. Combining Eqs. 3.1 and 3.3, we can relate the change in specific Gibbs free energy upon nucleation to the degree of subcooling as

$$\Delta\tilde{g} = \frac{h_{ij}}{v}\frac{\Delta T}{T_{n,w}}. \tag{3.4}$$

Of course, the critical $p\!-\!T$ curve at which nucleation first occurs is path independent: $p_{n,w}(T_w) \equiv T_{n,w}(p_w)$.

Now that the specific free enthalpy change upon nucleation is known as a function of $p_{n,w}$ and T_w (Eq. 3.3), it is possible to estimate $p_{n,w}$ as an analytical expression in T_w provided that the value of $\Delta\tilde{g}$ could be independently solved using an additional relation. Such an expression can be obtained by equating the change in specific Gibbs energy ($\Delta\tilde{g}$) to the total Gibbs energy (ΔG). For an embryo of volume V, ΔG can be expressed as a summation of the negative change in energy inherent to supersaturated vapor becoming liquid (or ice) and the positive energy barrier associated with the creation of the interfaces (liquid–solid and liquid–vapor interfaces for condensation and ice–solid and ice–vapor for desublimation): [16]

$$\Delta G = V\Delta\tilde{g} + A_{ij}\sigma_{ij} + A_{jk}\big(\sigma_{jk} - \sigma_{ik}\big), \tag{3.5}$$

where i, j and k are the three different phases (vapor, water or ice, and the solid substrate) and A_{ij} and σ_{ij} represent the interfacial area and surface tension between phases i and j. Assuming that the nucleating embryo exhibits a uniform spherical-cap shape, the critical radius of curvature where nucleation is stable can by found by solving for $\partial\Delta G/\partial r = 0$:

$$r^* = -\frac{2\sigma_{ij}}{\Delta\tilde{g}}. \tag{3.6}$$

Young's relation can be used to collapse the three surface tension terms down to a single dimensionless variable, [159] often denoted as m:

$$m = \cos\theta = \frac{\sigma_{jk} - \sigma_{ik}}{\sigma_{ij}}, \tag{3.7}$$

where θ is the intrinsic contact angle of the water (or ice) with the smooth substrate. A point rarely mentioned in the nucleation literature is the chemical limit of hydrophobicity on smooth surfaces of around $\theta_{max} \approx 120°$ [85]. Though our calculations assume a smooth substrate, they should generally apply even for rough surfaces because the length scale of surface roughness tends to be larger than the size of nucleating embryos ($r \sim 1$–10 nm). Therefore we restrict our parameter space here to $0° \leq \theta \leq 120°$.

By combining Eqs. 3.5–3.7, we obtain the critical change in free energy required for nucleating an embryo:

$$\Delta G^* = \frac{4\pi}{3} \frac{\sigma_{ij}^3}{\Delta\tilde{g}^2} \left(2 + m\right)\left(1 - m\right)^2. \tag{3.8}$$

Using the Becker-Döring exponential relationship of the embryo formation kinetics, [83] we can solve for ΔG^* independently of Eq. 3.8 as a function of the surface temperature and embryo formation rate:

$$I = I_0 \exp\left(-\frac{\Delta G}{kT_w}\right), \tag{3.9}$$

where I is the embryo formation rate, I_0 is the kinetic constant, and $k = 1.38 \times 10^{-23}$ J/K is the Boltzmann constant. The critical change in free energy ΔG^* corresponds to the minimum value of the embryo formation rate required for nucleation to first occur, $I = I_c$. Thus, by combining equations (3.3), (3.8) and (3.9), the critical supersaturation $p_{n,w}$ required for embryo formation is finally obtained:

$$p_{n,w} = p_{s,w} \, \exp\left(\frac{v}{RT_w} \sqrt{\frac{4\pi}{3} \frac{\sigma_{ij}^3}{kT_w \ln\left(\frac{I_0}{I_c}\right)} \left(2 + m\right)\left(1 - m\right)^2}\right). \tag{3.10}$$

Note that $p_{s,w}$, σ_{ij}, and v all are purely functions of temperature; these functions are well known for both liquid water and ice (see Equations S1–S6 in the Supporting Information). Therefore $p_{n,w}$ is now a semi-analytical expression in m, I^*, and T_w, where $m = \cos\theta$ and $I^* = I_0/I_c$. It is generally agreed in the literature that the value of $I_c \sim 10^4 \, \text{m}^{-2}\text{s}^{-1}$ found for homogeneous nucleation is also valid for heterogeneous nucleation on dry substrates, for both the condensation and desublimation modes [4, 7, 83, 132, 148]. The value of the kinetic constant, I_0, is actually a weak function of T_w, $P_{n,w}$, and σ_{ij}, and is thought to vary from $I_0 \sim 10^{28} \, \text{m}^{-2}\text{s}^{-1}$ to $I_0 \sim 10^{31} \, \text{m}^{-2}\text{s}^{-1}$.
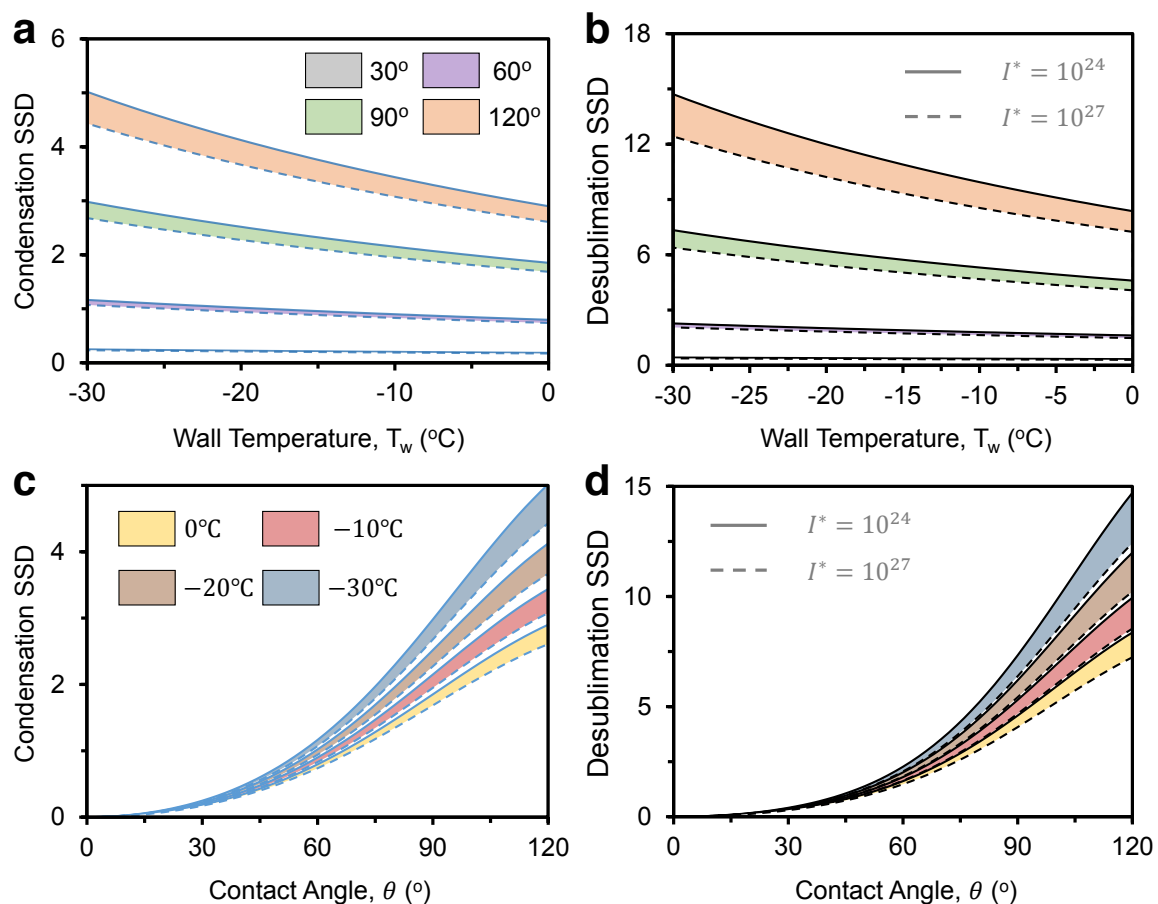
FIGURE 3.3: Supersaturation degree (SSD) required for (a) condensation or (b) desublimation embryos to nucleate on a substrate as a function of surface temperature (T_w) for different surface wettabilities ($\theta = 30°$, $60°$, $90°$, and $120°$) and embryo formation rates ($I^* = 10^{24}$ and 10^{27}). All curves were obtained by solving for Eq. 3.2 in conjunction with Eq. C.1. The gray region depicting the SSD corresponding to $\theta = 30°$ is not visible because of its extremely low variation with I^*. (c) and (d) represent the SSD required for condensation and desublimation respectively as a function of wettability (θ) for different surface temperatures ($T_w = 0\,°C$, $-10\,°C$, $-20\,°C$ and $-30\,°C$) and embryo formation rates ($I^* = 10^{24}$ and 10^{27}). While qualitatively similar, note that the SSD for desublimation is roughly $3X$ greater than the corresponding condensation SSD requirement over the entire parameter space.

[12, 16, 149] Many works choose $I_0 \sim 10^{29}\,\mathrm{m^{-2}s^{-1}}$ as a fixed constant for both condensation and desublimation; [7, 11, 132] here, we use the full span of $I_0 \sim 10^{28}\,\mathrm{m^{-2}s^{-1}}$ to $I_0 \sim 10^{31}\,\mathrm{m^{-2}s^{-1}}$ to vary I^* by 3 orders of magnitude: $I^* = 10^{24} - 10^{27}$.

Figure 3.3 shows the supersaturation degree required for condensation and desublimation as a continuous function of temperature for four different values of θ and also as a continuous function of wettability for four different values of T_w, while varying I^* over three orders of magnitude for all cases. To our knowledge, we are the first to present SSD as a function of T_w and I^* in addition to θ; other reports simply present SSD vs. θ for a fixed value of T_w (typically 0°C) and I^* (typically 10^{25}) [7, 11, 132]. It can be seen that the degree of supersaturation required for embryo formation is much larger for hydrophobic surfaces (for $\theta = 120°$ and T_w spanning from 0° to $-30°\,\mathrm{C}$, $SSD \approx 3$–5 for condensation and $SSD \approx 8$–15 for desublimation) than for hydrophilic surfaces ($SSD \to 0$ as $\theta \to 0°$). It follows that for a chemically heterogeneous surface exhibiting both hydrophobic and hydrophilic features, nucleation events will preferentially occur within the hydrophilic patterns, which can be exploited to increase condensation heat transfer [64, 66, 67], enhance water harvesting [69–71], or to control icing/frosting behavior [63, 72, 73]. Note that in reality, though, no surface is perfectly smooth and chemically homogeneous everywhere. As such even a chemically functionalized smooth surface has intrinsic defects that expose high surface energy sites beneath the coating. Hence condensation can initiate at these sites at a significantly lower SSD even for hydrophobic substrates [63, 160]. In Figure 3.3, we also see that for a fixed wettability, the value of SSD decreases with increasing temperature, the effect being more pronounced on hydrophobic surfaces. This is because at higher temperatures, the specific Gibbs energy required for nucleation is lower. Consequently the supersaturation requirement for nucleation is also less. However, for two substrates at the same temperature, the one that is hydrophobic would have a higher energy barrier and therefore a higher SSD requirement for nucleation.

Figure 3.3 also demonstrates how a variance in I^* by 3 orders of magnitude can moderately affect the SSD estimations of both condensation and desublimation. For instance desublimation SSD values can vary by more than 18% at $T_w = -30°\mathrm{C}$ for $\theta = 120°$ and $I^* = 10^{24} - 10^{27}$. This effect is more severe on hydrophobic surfaces, especially at colder temperatures. Only the condensation SSD values for hydrophilic surfaces remain fairly constant. Therefore we suggest that it could be fruitful for future works to remeasure the embryo formation rates standardized by Volmer and Flood in 1934 [148] and Becker and Döring in 1935 [83] using modern equipment. Also, note that the value of I_c measured by Volmer and Flood was for homogeneous nucleation, so modern measurements of I_c could benefit from explicitly characterizing heterogeneous nucleation on a substrate instead of simply applying the rate obtained from homogeneous nucleation. One final observation from Figure 3.3: the desublimation mode SSD is always higher than that of the condensation mode SSD, in agreement with Na and Webb [7]. Recall that an alternate way to conceptualize supersaturation is to quantify the subcooling degree required for nucleation, this

analogous representation can be seen in Figure S3 in the Supporting Information.

a

b
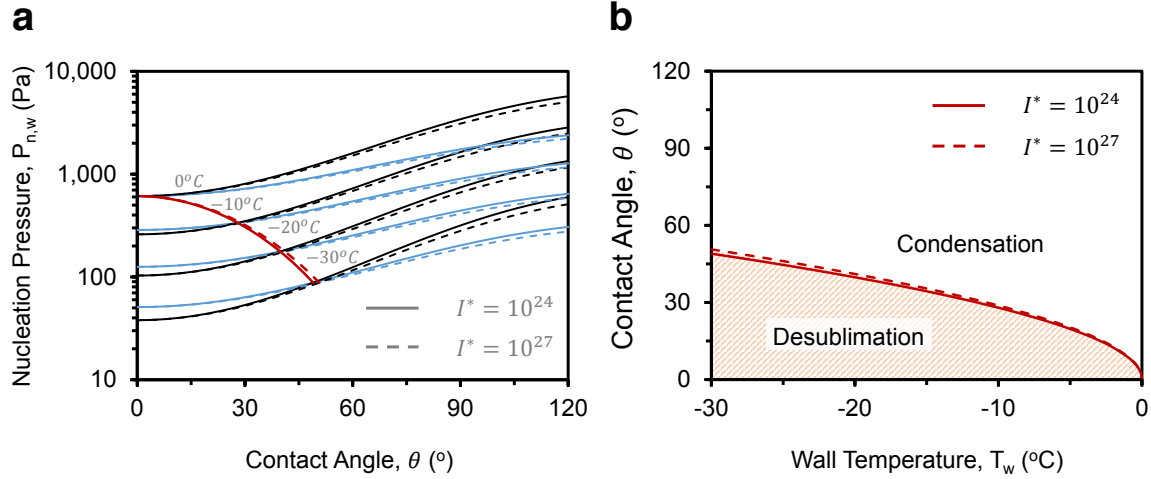
FIGURE 3.4: (a) Nucleation pressure ($p_{n,w}$, Eq. C.1) required for condensation (blue lines) and desublimation (black lines) as a function of θ for different wall temperatures ($T_w = 0\,°\text{C}$, $-10\,°\text{C}$, $-20\,°\text{C}$, and $-30\,°\text{C}$) and embryo formation rates ($I^* = 10^{24}$ and 10^{27}). The red dotted line is the locus of the intersection points of $p_{n,w}$ for the desublimation and condensation curves for wall temperatures ranging continuously from $0\,°\text{C}$ to $-30\,°\text{C}$, where desublimation is favored to the left and condensation to the right. (b) Phase diagram for the preferred mode of nucleation for any surface temperature and wettability, where supercooled condensation is thermodynamically favorable in the phase space above the critical line and desublimation is favorable below.

Since the SSD of condensation is always less than for desublimation, it would appear tempting to assume that condensation is always the dominant mode of nucleation. Previously Sanders [11] and Na [7] have argued that for vapor pressures below condensation SSD, there is no nucleation, for pressures greater than condensation SSD but less than desublimation SSD, condensation is the favored mode of nucleation, and for pressures greater than desublimation SSD, both modes of nucleation are possible. However, recall that the pressure curve for saturated water is slightly larger than the curve for saturated ice (cf. Fig. 3.1), so the SSD being larger for desublimation does not necessarily mean that $p_{n,w}$ itself is always larger. Indeed, here we show for the first time that the pressure required for desublimation can be less than that for condensation if the substrate is hydrophilic enough. Figure 3.4a shows $p_{n,w}$ versus θ for several different temperatures, and it can be seen that $p_{n,w}$ is actually lower for desublimation compared to condensation when θ is beneath a critical value that depends upon T_w (red line). This can also be shown by plotting $p_{n,w}$ versus T_w instead, which is depicted in Figure S4 (see Supporting Information). By solving for the intersection point of $p_{n,w}$ between the condensation and desublimation curves for any given surface temperature and wettability, a $\theta - T_w$

phase map is created in Figure 3.4b while complementary $p_{n,w}-T_w$ and $p_{n,w}-\theta$ phase maps are provided in the Supporting Information Figure S5. It can be concluded that the preferred mode of nucleation for chilled substrates is liquid condensation for hydrophobic or moderately hydrophilic substrates. However, desublimation becomes thermodynamically favorable for sufficiently hydrophilic surfaces, especially at colder temperatures. Note that for a given surface, a direct comparison of the SSD for condensation versus desublimation becomes complicated by the fact that the contact angle of ice is slightly larger than for water [11]. Therefore the T_w-θ phase diagram in Figure 3.4 serves as a conservative limit and in reality the red line will be shifted lower by a small amount.

3.2.3 Supersaturation – Pre-existing Water Droplet

The vapor pressure about the interface of a pre-existing water droplet is also supersaturated. However the extent of supersaturation depends on the curvature of the droplet and its temperature at its liquid-vapor interface (T_d). In the previous section we assumed that conductive losses across the droplet were negligible, such that $T_d \approx T_w$. However, this is not always true for pre-existing droplets, which at sufficiently large sizes and/or heat fluxes can exhibit $\Delta T_{cond} = T_d - T_w = Q_d\theta/(4\pi r \sin\theta k_w)$ across the bulk of the droplet, where Q_d is the rate of heat transfer (in Watts) and k_w is the thermal conductivity of water (in W/m·K) [161, 162]. Thus for a given droplet size, T_d can be calculated if the wall temperature, wettability, and heat transfer rate are all known.

Once the temperature at the interface of the droplet is calculated, the supersaturated vapor pressure can be found using the Kelvin-Laplace equation:

$$\Delta\tilde{g} = -\frac{2\sigma}{r} = -\frac{RT_d}{v}\ln\frac{p_{a,d}}{p_{s,d}}, \qquad (3.11)$$

where σ is the surface tension of the water/vapor interface, $P_{s,d}$ is the saturated vapor pressure corresponding to T_d, and $p_{a,d}$ is the actual (supersaturated) vapor pressure around the droplet. Note that $p_{a,d}$ represents the droplet's vapor pressure regardless of whether the droplet is growing ($p_\infty > p_{a,d}$) or shrinking ($p_\infty < p_{a,d}$). Figure 3.5 gives the variation of SSD with T_d for different droplet sizes, where $SSD = (P_{a,d} - p_{s,d})/p_{s,d}$. It can be seen that the supersaturation is quite significant for nanometric droplets (for example $SSD > 1$ when $r \sim 1\,\text{nm}$), but becomes insignificant ($< 0.1\,\%$ supersaturation) for micrometric droplets whose vapor pressure can be approximated as saturated. Note that in order to obtain better estimates of SSD, curvature-induced changes in surface tension [154–156] should be considered when the droplet curvature becomes comparable to the thickness of the liquid-vapor interface.

3.2.4 Supersaturation – Nucleation on Ice

Nucleation on pre-existing ice (i.e. frost growth) is different from nucleation on other substrates because ice is perfectly hydrophilic. The contact angle of water
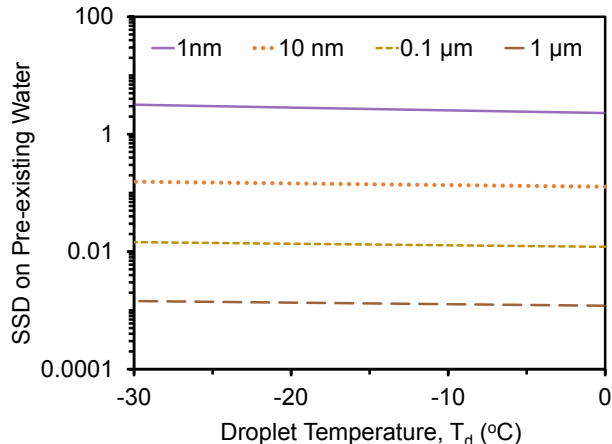
FIGURE 3.5: Supersaturation degree (SSD) versus droplet temperature (T_d) for a pre-existing liquid droplet. Each data series represents a different radius of curvature, ranging from highly supersaturated nanodroplets to approximately saturated microdroplets.

on ice at $T_w = 0\,°C$ is $\theta \approx 1°$ [23]. Therefore ice is, in some sense, the hydrophilic limit $\theta \to 0°$ of the heterogeneous nucleation curves in Figure 3.3c. Historically, models of frost growth typically assumed a saturated vapor pressure at the interface of the growing ice [11, 124–126, 133], but more recently many works have vigorously argued that the ice interface is supersaturated [7, 16, 121, 123]. The proponents of supersaturation give an argument that is perfectly analogous to embryo formation on a dry substrate: to nucleate more water or ice onto pre-existing ice requires the creation of new interfaces, which creates an energy barrier for the phase-change. Therefore we will begin by considering the supersaturation required to nucleate a fresh embryo onto a pre-existing body of ice. Note that because water completely wets the surface of ice, it would be appropriate to adapt a 2D nucleation model in this case.

Analogous to a dry substrate, nucleation occurring on pre-existing ice could occur in either the condensation mode or desublimation mode. Consider an ice droplet of temperature T_i resting on a substrate of temperature T_w. Note that the temperature T_i of the so-called "ice droplet" could equally apply to that of a sheet of ice; our droplet terminology here is simply due to the fact that we are often dealing with recently frozen condensate. For sufficiently large ice droplets/sheets, the temperature at the ice/vapor interface (T_i) is larger than the wall temperature and could be estimated in the same manner as the previous section. Assuming that the embryo nucleating on the ice manifests itself in the shape of a monolayer-thick disk [7], the total Gibbs energy change for embryo formation is:

$$\Delta G = \pi r_d^2 a \Delta \tilde{g} + 2\pi a r_d \sigma_{ij}, \qquad (3.12)$$

where $a \approx 1$ Å and r_d are the thickness and width of the disk and σ_{ij} is the surface

27

tension of the liquid-vapor (condensation) or ice-vapor (desublimation) interface. Note that since the "substrate" itself is already composed of ice, the only new interfacial area that had to be considered in Eq. 3.12 was the sides of the disk embryo. While it is true that a condensing embryo will replace an ice-vapor interface with an ice-liquid liquid-vapor dual interface, these are energetically equivalent according to Young's equation (Eq. 3.7) when $\theta \approx 0°$ which is the case for water on ice. By setting $\partial \Delta G / \partial r_d = 0$ to solve for the critical size of a stable embryo (r_d^*), the critical Gibbs free energy for nucleation is obtained:

$$r_d^* = -\frac{\sigma_{ij}}{\Delta \tilde{g}}, \tag{3.13}$$

$$\Delta G^* = -\frac{\pi \sigma_{ij}^2 a}{\Delta \tilde{g}}. \tag{3.14}$$

Using equations (3.3), (3.9) and (3.14) and replacing T_w by T_i and $p_{s,w}$ by $p_{s,i}$ we can write the critical supersaturation pressure for nucleation on pre-existing ice ($p_{n,i}$) as an analytical expression in T_i:

$$p_{n,i} = p_{s,i} \, \exp \left(\frac{N_a v \pi \sigma_{ij}^2 a}{R^2 T_i^2 \, \ln I^*} \right), \tag{3.15}$$

where N_a is Avogadro's number. Note that this disk embryo model does not consider the energetics of the quasi-liquid melt layer that can exist at an ice interface when p_∞ is sufficiently large [23, 150].

Before Eq. S4 can be used, a value for $I^* = I_0/I_c$ needs to be chosen for the case of nucleation onto an ice substrate. Na and Webb [7] used the same values of $I_0 \sim 10^{29} \, \text{m}^2\text{s}^{-1}$ and $I_c \sim 10^4 \, \text{m}^2\text{s}^{-1}$ as for the case of nucleation onto a dry substrate, but do not provide any justification for doing so [7]. In Figure 3.6, we show the implications of using the same I^* values for ice as were used for dry surfaces (I^* ranging from 10^{24} to 10^{27}). Firstly, this shows that even on pre-existing ice, there is a change in the preferred nucleation mode between condensation and desublimation, with the inflection point denoted by the intersection of $P_{n,i}$. Also, note that despite the fact that ice is perfectly hydrophilic, the nucleation pressure is supersaturated for all ice temperatures. This is in sharp contrast to what we obtained from our 3D nucleation model for nucleation on a dry smooth surface, where the nucleation pressure becomes saturated ($SSD \rightarrow 0$) as $\theta \rightarrow 0°$ (cf. Figure 3.3). Though this may be true for the specific case of nucleation on ice, it is extremely important that the choice of I^* for an ice substrate is further scrutinized before proceeding any further with this model. We will revisit this choice of I^* in Chapter 5, where we will use experimentally measured inter-droplet ice bridge growth rates to answer the question whether the vapor pressure at the interface of growing ice is at all supersaturated.
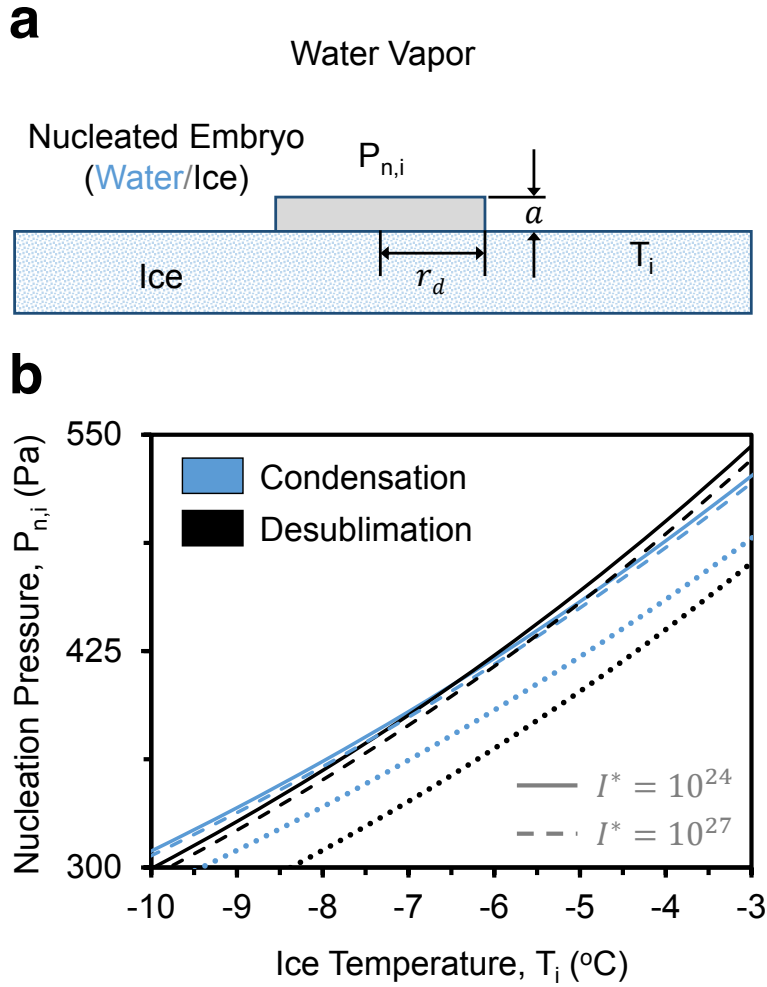
FIGURE 3.6: a) Schematic of a nucleation process on pre-existing ice. b) Vapor pressure required for nucleation on pre-existing ice as a function of the ice temperature (Eq. S4). Blue/black lines represent the pressure to nucleate water/ice on ice when $I^* = 10^{24}$ (solid lines), $I^* = 10^{27}$ (dashed lines), or under saturated conditions (dotted lines). Assuming supersaturated conditions, condensation becomes the favorable mode of nucleation on ice above a critical temperature ($T_i > -6\,°C$ for $I^* = 10^{24}$ or $I^* = 10^{27}$), while desublimation always exhibits a lower $P_{n,i}$ for nucleation occurring under approximately saturated conditions. Note that the range of temperatures depicted here was intentionally constrained to better visualize the intersecting $p_{n,i}$ curves; see Supporting Information Figure S6 for the full parameter space.

4
Frost Halos

"But all around me, everybody's multiplying..."

− The Kinks

The phenomena of frost halos was first reported in 1970 by Roger Cheng as a spontaneous ejection of microdroplets during the freezing event of a droplet [116]. However, in light of a recent report by Jung et al. [4], it appears that these microdroplets were not directly ejected at all, but rather are nucleated condensate fostered by a recalescence-induced local supersaturation in the vicinity of the freezing droplet.

The freezing of a milimetric droplet consists of two stages - a) a rapid kinetically controlled stage called recalescence and b) isothermal freezing of the droplet and subsequent conductive cooling to the substrate temperature. During the first stage the droplet turns opaque, with the formation of an ice scaffold filled with partially frozen liquid. Due to the sudden release of latent heat, the temperature of the droplet quickly increases from its supercooled temperature $T_d \approx T_w$ up to $T_i \approx 0\,^\circ\mathrm{C}$ [110–113, 116]. This leads to an explosive evaporation from the freezing liquid droplet that manifests itself as an annular ring of condensate microdroplets around the frozen droplet that can quickly freeze over, hence the designation of frost halos (Figure 2.4a). Once the droplet has finished freezing, it grows bridges to freeze the surrounding ring of satellite condensation, hence the term "frost halo" [4, 62].

So, what are the criteria for frost halos to form?

First, the substrate has to be wettable enough that the vapor can nucleate. This criterion can be met if the pressure required to nucleate on the substrate, $p_{n,w}$ is less than the vapor pressure about the droplet. Since the temperature of the droplet during recalescence is $T_i \approx 0\,^\circ\mathrm{C}$, therefore the vapor pressure around this recalescent droplet corresponds to the saturation pressure of ice: $p_{i,0} \approx (p_{s,i})_{T=0\,^\circ\mathrm{C}} = 611.2\,\mathrm{Pa}$. Therefore, this criterion is satisfied when $p_{n,w} < p_{i,0}$. For condensation, one may thus write,

$$p_{i,0} > p_{s,w} \, \exp\left(\frac{v}{RT_w} \sqrt{\frac{4\pi}{3} \frac{\sigma_{ij}^3}{kT_w \, \ln\left(\frac{I_0}{I}\right)} \left(2+m\right)\left(1-m\right)^2} \right), \tag{4.1}$$

where the right hand side of the equation corresponds to the critical pressure $p_{n,w}$ required for condensation (cf. Eq. C.1).

This however is just the necessary condition for the formation of frost halos, but not sufficient. There is an added survivability constraint for the ensuing condensate, which deals with the second stage of freezing. This condition is essentially that the duration of freezing τ_f, when $T_i \approx 0\,^\circ\mathrm{C}$ is much greater than the diffusion time scale τ_D. From the saturation vapor pressure curves, we know that the vapor pressure over ice is lower than that over water at the same subzero temperature. If the droplet quickly cools down from $0\,^\circ\mathrm{C}$ to the substrate temperature, the emanated vapor will change direction and instead of diffusing radially outward, would go toward the lower pressure region of the ice droplet itself. In the critical case of when the two time scales are the same, even if a condensate nucleates, it will instantly evaporate out. As such no frost halos would be observable, even if the wettability of the substrate is amenable for nucleation the vapor. Thus the necessary and sufficient criteria for
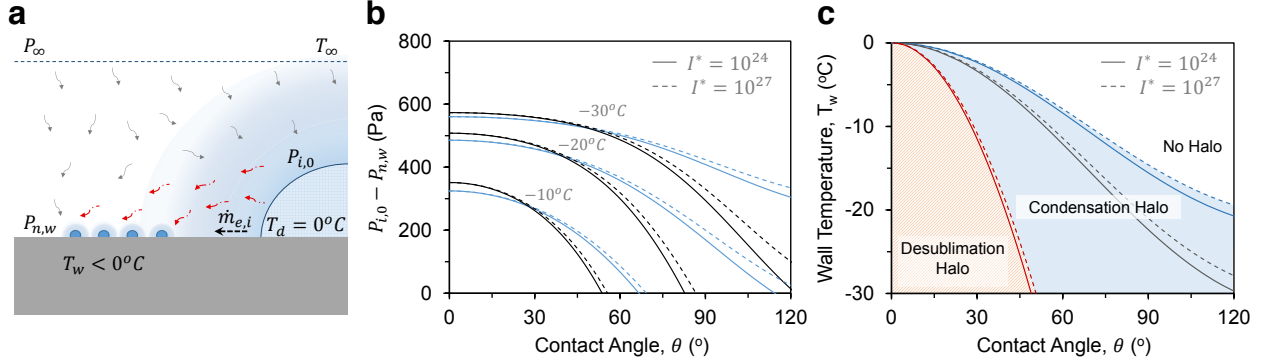
FIGURE 4.1: a) Schematic of a supercooled droplet after its initial stage of freezing, where the droplet temperature and vapor pressure are rapidly increased to $T_i \approx 0\,^\circ\mathrm{C}$ and $P_{i,0} \approx 611\,\mathrm{Pa}$, respectively. b) The difference between the vapor pressure of the freezing droplet and the pressure required to nucleate an embryo on the substrate, calculated from Eq. C.1 and plotted as a function of the substrate wettability. Blue and black curves correspond to the nucleation pressure for condensation versus desublimation; positive values correspond to when nucleation is possible. c) Phase map that predicts when desublimation halos (red region), condensation halos (blue), or no halos (white) should form around a freezing droplet, as a function of the surface temperature and wettability.

formation and survivability of frost halos are given by

$$p_{n,w} < p_{i,0}$$
$$\tau_D < \tau_f \tag{4.2}$$

The time of conductive cooling of the frozen droplet can be controlled by tuning the conductivity of the substrate as has been shown by Jung et. al. [4], while the nucleation pressure can be changed by changing the wettability and/or the temperature of the substrate.

Now, from our previous discussion on nucleation theory (Chapter 3) we know that it is not necessary that condensation be the dominant mode of nucleation always. Desublimation, too can ensue, if the critical nucleation pressure associated with desublimation be less than that for condensation, that is, if $p_{n,i} < p_{n,l}$. Should that be the case, we would in fact see a desublimation halo, where the emanated vapor from the freezing droplet directly transitions to an annular ice ring around the mother droplet.

In Figure 4.1b we show where $p_{i,0} - p_{n,w}$ attains a positive value (thus fulfilling the criteria for nucleation) as a function of θ for multiple values of T_w. Both the condensation (blue lines) and desublimation (black lines) modes of nucleation are considered, where the preferred mode corresponds to whichever curve exhibits a lower value of $p_{n,w}$ (and hence a larger value of $p_{i,0} - p_{n,w}$) for a given value of θ and T_w. Figure 4.1b reveals that for a given surface temperature, there exists a

critical contact angle above which nucleation cannot occur; this critical θ corresponds to where each curve intercepts the x-axis. These findings suggest that the halo effect should be suppressed for sufficiently hydrophobic surfaces (aside from surface defects), particularly for wall temperatures approaching $T_w \to 0\,^{\circ}\text{C}$. As a validation of our theoretical predictions, we compare our findings with the experimental conditions where Jung et al. observed frost halos [4]. In their experiments $T_w = -14.5\,^{\circ}\text{C}$ and $\theta \approx 72°$. For a surface temperature of $T_w = -14.5°\text{C}$, our model predicts that the largest contact angle surface where the halo effect can be observed should correspond to $86° < \theta_{max} < 90°$ for $10^{24} < I^* < 10^{27}$. Therefore their observation of halos forming for a surface wettability of $\theta = 72°$ is in agreement with our model.

By calculating the critical wettability for every possible wall temperature, a complete phase map was constructed as shown in Figure 4.1c. The blue and black lines represent the critical $T_w - \theta$ curves beneath which condensation and desublimation can occur, respectively. In other words, beneath these critical curves the $p_{i,0} > p_{n,w}$ condition for nucleation is fulfilled. To determine which mode of nucleation is favorable, the critical $T_w - \theta$ curve from Figure 3.4b is added to the phase map (red lines), where the condensation mode is favored above the curve and desublimation is favored below. By considering these critical curves in conjunction with each other, the phase map can theoretically predict whether no halo, a condensation halo, or a desublimation halo should occur upon the freezing of a supercooled droplet. It should be noted that the experiments of Jung et al. were over a narrow parameter space that only demonstrated a condensation halo [4], so the prediction of a desublimation halo has yet to be experimentally validated.

5

Ice Bridges

"Connection, I just can't make no.
Connection, but all I want to do... "

− The Rolling Stones

The content of this chapter is derived from a subection of previously published journal manuscript in [141] and an unpublished manuscript, reproduced here with appropriate modifications. This chapter deals with the underlying mechanism of the formation of ice bridges, experiments and scaling laws.

5.1 Introduction

As we discussed in Chapter 2, the underlying mechanism of frost incipience at a microscopic level is inter-droplet ice bridging, where ice bridges percolate through the entire population of supercooled condensate forming an interconnected network of frozen droplets and ice bridges [5, 6, 57]. The challenge is to now understand what dictates whether an ice bridge growing from a frozen droplet can eventually freeze its nearest neighbor. To answer this, we perform extensive experiments with droplet pair interactions with sizes ranging from $1\,\mu m - 10\,mm$. Surprisingly, we find that the answer is almost always independent of the growth rate of ice bridge, substrate temperature, ambient temperature and humidity and just dependent on the droplet sizes and inter-droplet distance. We construct a phase map, identifying five possible modes of ice bridging based on their relative sizes and derive the scaling laws that govern their dynamics in these regimes. Thereafter, we formulate a velocity model, validate it with experimentally measured growth rate values and discuss how it resolves the long-standing debate on whether the vapor pressure at the interface of ice is saturated or not. Subsequently, we also experimentally demonstrate how in-plane frost growth can be controlled and even halted by tuning inter-droplet distances.

5.2 Critical Condition for Connection and Dependence on Relative Sizes

A frozen droplet is like a humidity sink to its neighboring liquid droplets because the saturation vapor pressure over ice is lower than that above water at the same sub-freezing temperature [20]. Vapor from the nearest neighboring liquid water droplet evaporates toward the frozen droplet and deposits on its surface to form a growing ice bridge directed toward the liquid droplet being harvested (see Figure 5.1). This can end in two possibilities– the ice bridge can connect to the evaporating droplet, freezing it in the process, or the liquid droplet can completely evaporate before the ice bridge connects to it. For the former, a chain reaction of ice bridging ensues where the newly frozen droplets grow ice bridges toward their nearest neighbor liquid droplets and so on leading to a percolating network of interconnected frozen droplets [5, 6, 57]. For the latter, the ice bridge can keep growing toward the next set of liquid droplets which were previously shielded by frozen droplet's nearest neighbor. However, if the liquid droplets are too far away to diffusively interact with the ice droplet, then there remains a dry zone between the frozen droplet and the condensate population, where there is no condensation or frost growth [63, 141].

Therefore we see that the nature of propagation of in-plane frost depends on the interdroplet network of successful ice bridge connections. This leads to two broad questions that one may ask. First, what is the percolation dynamics of the global in-plane freeze front that propagates through a condensate population? This question relates to the macroscopic picture of front propagation in a mixed-mode
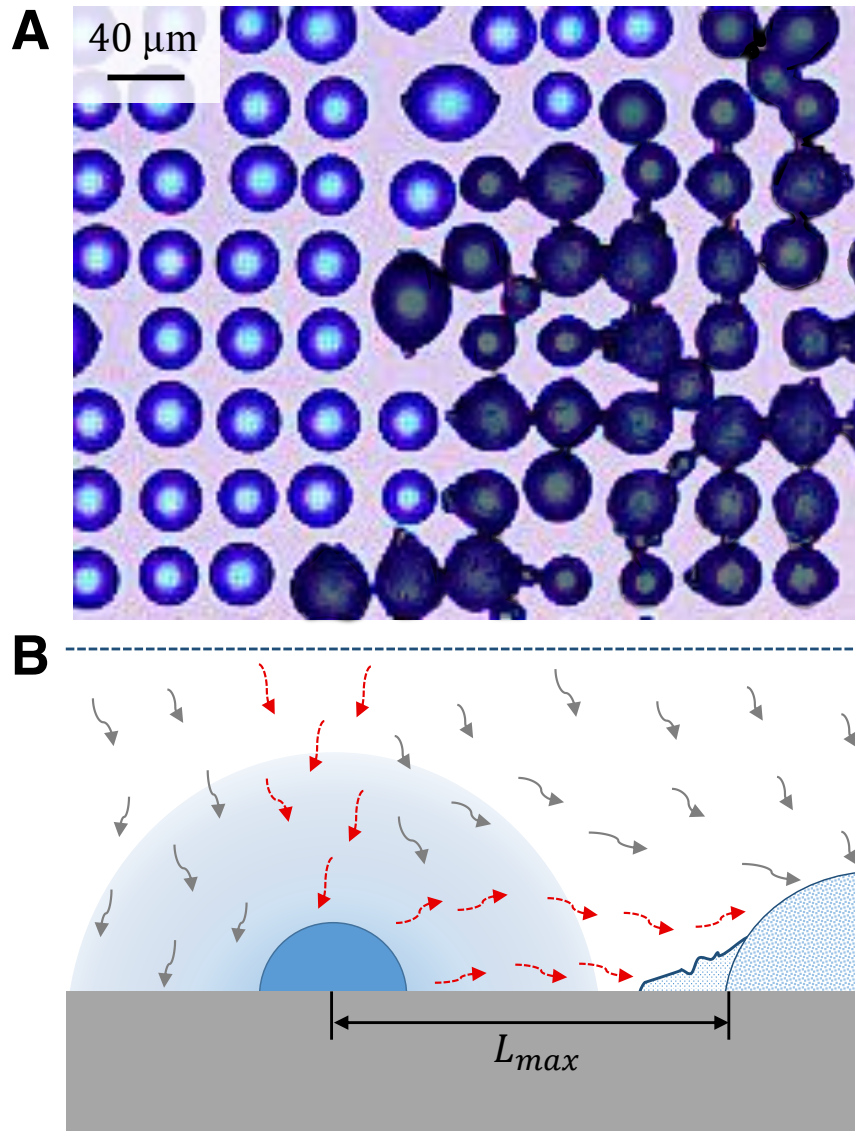
FIGURE 5.1: a) Condensation frosting percolating through a supercooled condensate population at a steady-state substrate temperature of $T_s = -10\,°\text{C}$ and supersaturation $S = 2.7$. The frozen droplet and ice bridges have been false-colored black. b) Schematic of diffusive vapor exchange between a pair of frozen droplet and a liquid water droplet, leading to the formation of a directed ice bridge.
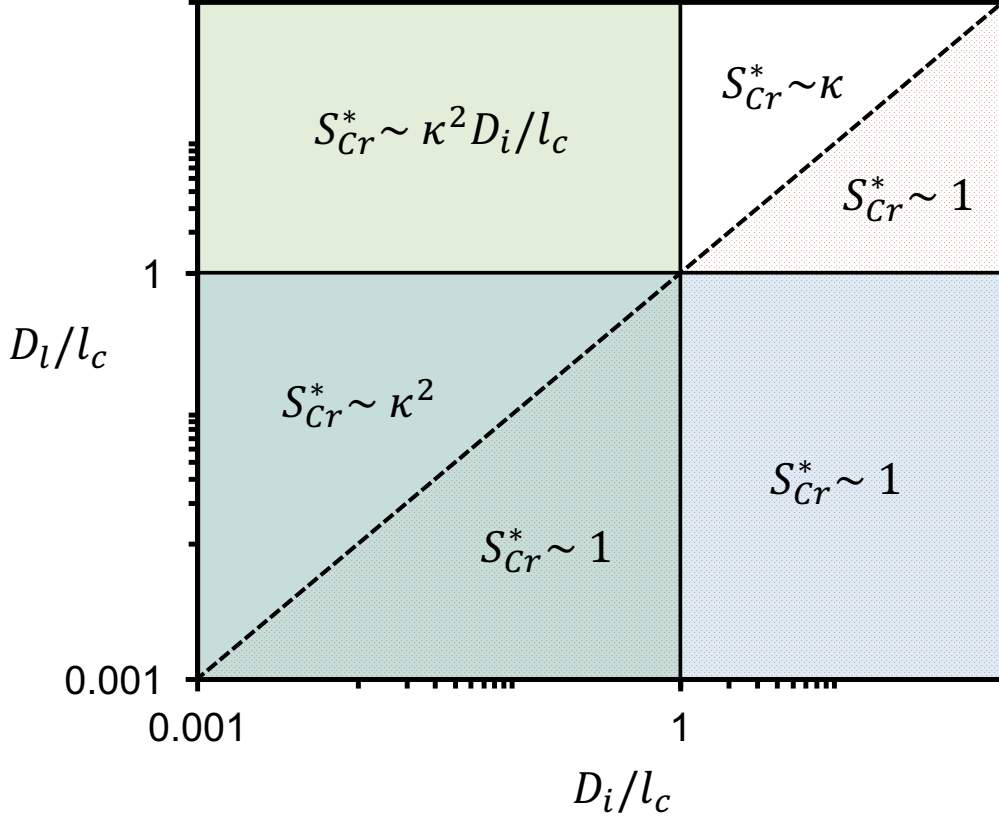
FIGURE 5.2: Theoretically obtained scaling laws for ice bridge connections, based on conservation on mass, for different sizes of the liquid and frozen droplet. However not all of these laws are experimentally observed. Here, the X and Y axes represent the frozen droplet and liquid droplet diameters, nondimensionalized by the capillary length scale, l_c. The 45° line divides the phase map into two regions: $\kappa < 1$ (dotted) and $\kappa > 1$ (not dotted).

phase change system. The other question relates to the microscopic picture where we may ask what governs the kinetics of individual ice bridge connections and failures. The eventual goal would be do find out how the microscopic physics of interdroplet ice bridge connections can be reconciled with the macroscopic behavior of the global freeze front. In this section, we take the first steps in understanding the microscopic picture of inter-droplet ice bridging– more specifically, what governs whether an ice bridge can successfully connect to its nearest neighboring liquid droplet.

In a droplet pair interaction, the maximum extent to which an ice bridge can grow is geometrically constrained by the distance L_{max} from the edge of the frozen droplet (base of the ice bridge) to the center of the liquid droplet. Due to the axisymmetric receding of the liquid droplet's contact line during evaporation, L_{max} is constant over time. Since the growth of an interdroplet ice bridge is entirely fueled by the evapora-

37

A

$$S^*_{Cr} \sim 1$$

$$m_l \sim \rho_l D_l^3 \qquad m_b \sim \rho_i D_l^2 L_{max}$$

B

$$S^*_{Cr} \sim \kappa^2$$

$$m_b \sim \rho_i D_i^2 L_{max} \qquad m_l \sim \rho_l D_l^3$$

C

Bridge Fails

$$S^*_{Cr} \sim \kappa^2$$

$$S^*_{Cr} \sim 1$$

Bridge Succeeds

Separation Parameter, S^*

$\kappa = D_l/D_i$
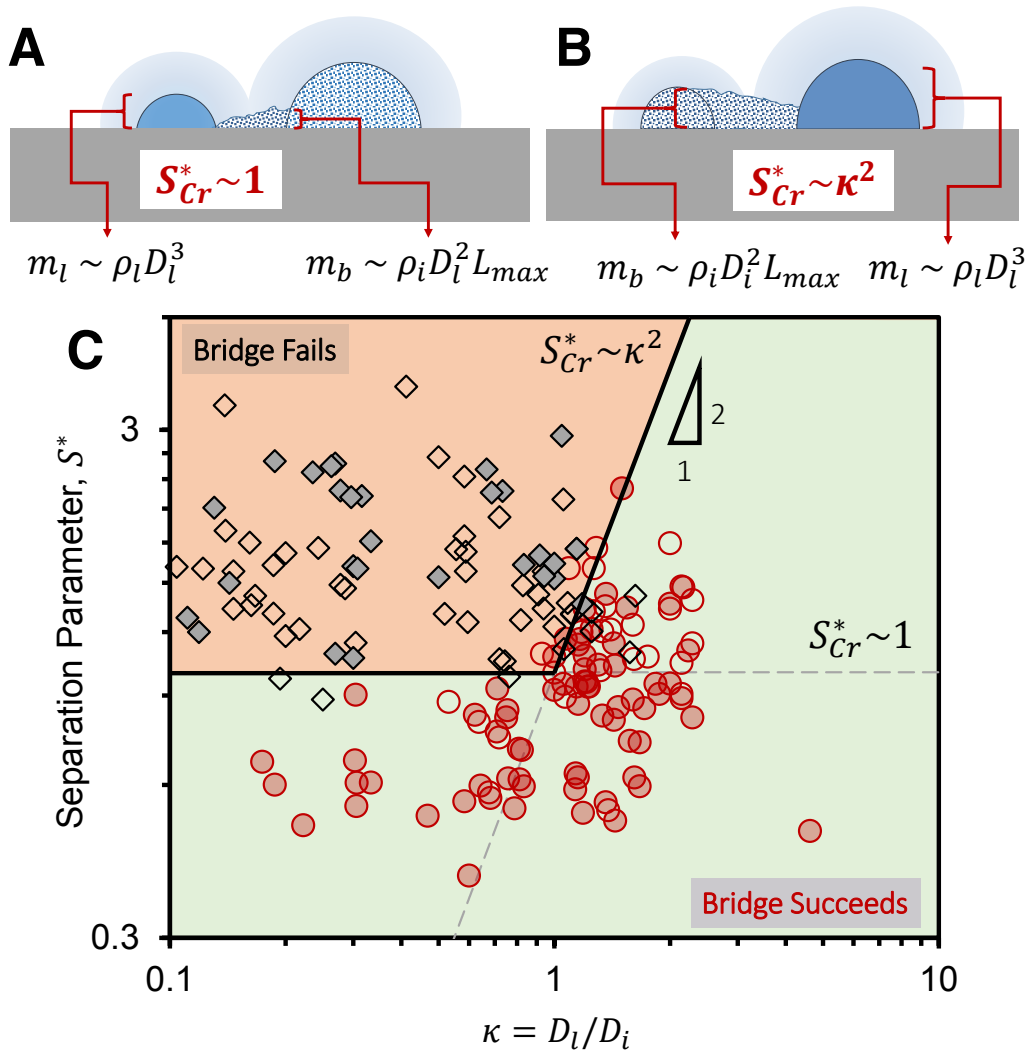
FIGURE 5.3: a) Schematic corresponding to the case of droplet pair interaction with liquid microcondensate, where the frozen droplet is larger in size b) Schematic for the same, but when the liquid droplet is larger in size. c) Phase map of success and failure of ice bridge connections. Experiments were performed on a hydrophobic substrate at $T_s = -10\,^{\circ}\mathrm{C}$. Circles denote successful bridge connections, while diamonds indicate failure. Hollow markers correspond to multi-droplet interactions, while solid markers indicate exclusive droplet pair interactions. The phase map demonstrates that for $\kappa < 1$, that is when the frozen droplet is larger in size, $S^*_{Cr} \sim 1$, and when $\kappa > 1$, $S^*_{Cr} \sim \kappa^2$, thus validating our scaling law predictions.

tion of the neighboring liquid droplet, we can find out the maximum extent to which a bridge can grow by equating the mass of the ice bridge with the mass of evaporated liquid droplet. Let the liquid and ice droplet contact line diameters be D_l and D_i respectively. The mass of the liquid droplet $m_l \sim \rho_l D_l^3$, if the $D_l << l_c$, where l_c is the capillary length scale. For the cases when the frozen droplet is larger than the liquid drop, $m_b \sim \rho_i L D_l^2$, while for the cases where the frozen droplet is smaller than the liquid drop, $m_b \sim \rho_i L D_i^2$, where L is the total length of the bridge and D_i is the initial (projected) diameter of the frozen drop. This is because the vapor flux emanating from the liquid drop is proportional to its area $A_l \sim D_l^2$, but the frozen drop can only accommodate for an area $A_i \sim D_i^2$, if $D_i < D_l$. Using conservation of mass we obtain the limiting condition for ice bridge connection, which can be written concisely as

$$
\begin{array}{ll}
S^* < S_{Cr}^* & \text{for ice bridge to connect} \\
S^* > S_{Cr}^* & \text{for ice bridge to fail}
\end{array}
\qquad
\text{where } S_{Cr}^* =
\begin{cases}
1 & \text{,if } \kappa < 1 \\
\kappa^2 & \text{,if } \kappa > 1
\end{cases}
\qquad (5.1)
$$

and $S^* = L_{max}/D_l$. Thus S^* and κ are the two nondimensional parameters that are sufficient to capture the physics of the ice bridging phenomenon and predict the success and failure of ice bridge connections. The above scaling law only holds true when $D_l, D_i << l_c$. Note that if either of the interacting droplet is larger than l_c, then the droplet takes the shape of a puddle [163], whose height $h \approx 2l_c$. Correspondingly the scaling laws would change, which have been summarized in Figure 5.2. Figure 5.3 shows a phase map of the success and failure of ice bridge connections and the two different modes of success as predicted by Equation 5.1. Figure 5.3 shows two droplet pair interactions corresponding to success and failure respectively.

Two of the five scaling laws as summarized in Figure 5.2 could not be experimentally verified by our experiments. The first one of these cases corresponds to a liquid puddle-frozen cap pair interaction, where $S_{Cr}^* = \kappa^2 l_c/D_w$. Experiments in this domain showed ice bridge connections were always successful. Now, from the definition of S^*, we see that $S^* = L_{max}/D_l = (D_l + \delta)/D_l = 1 + \delta_0/D_l$, where δ_0 is the edge-to-edge inter-droplet separation. Now inter-droplet distances δ typically scale as 1-10μm, whereas $D_l \sim l_c \sim 1$ mm in this particular case. This implies for a liquid puddle-frozen cap pair interaction, S^* is always close to 1, but $S_{Cr}^* >> 1$, as $\kappa >> 1$ and $l_c >> D_l$. Therefore, $S^* < S_{Cr}^*$, which means all ice bridge connections in this domain would be successful. This is precisely what we saw in our experiments, but the lack of failed bridge connections also implies that it is impossible to trace the $S_{Cr}^* = \kappa^2 l_c/D_w$ line on a phase map as could be done for the other cases, as seen in Figure 5.3. The second of these cases corresponds to a puddle-puddle interaction, where $\kappa \approx 1$. The reason for not observing any bridging in this case is entirely different. When two milimetric liquid droplets were deposited in the vicinity of each other, there inevitably formed a liquid ring of microcondensate around them. To eliminate this we performed experiments inside a humidity chamber where the humidity was decreased to near-zero, microcondensqate between the two adjacent

39
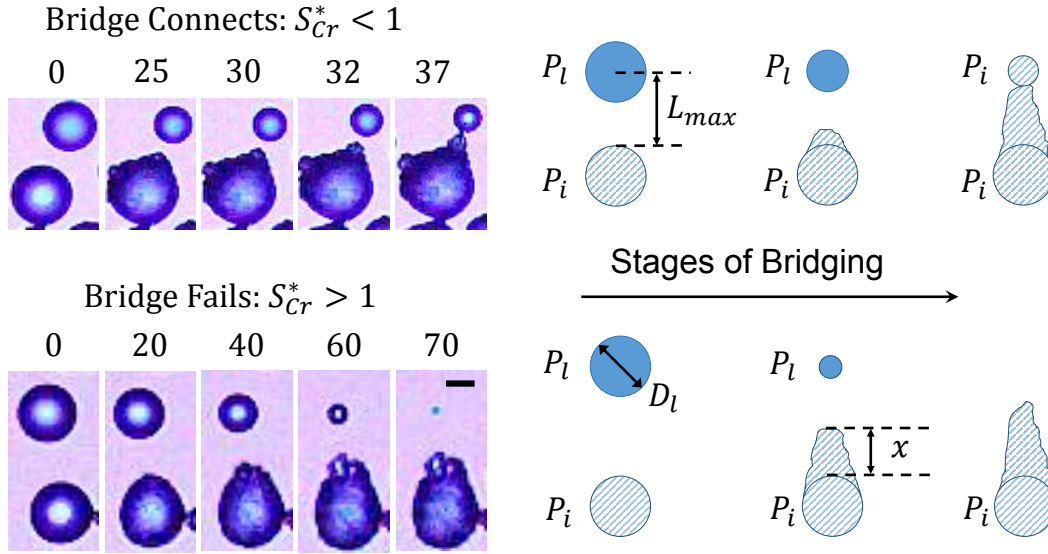
FIGURE 5.4: Experimental and schematic depiction of the two different regimes of ice bridging that occur between a frozen droplet and supercooled liquid droplet. Experiments performed at $T_w = -10\,^{\circ}\text{C}$ and $p_\infty = 776.3\,\text{Pa}$; time stamps are in seconds and scale bar represents $20\,\mu\text{m}$.

milimetric liquid droplets did not evaporate. This is because of the local supersaturation engendered by the liquid droplets placed next to each other. As such, once one of the two droplets froze, it started interacting with the liquid microcondensate. A direct frozen puddle-liquid puddle par interaction is thus practically impossible on a substrate. It however should be possibly if the droplets are suspended in air, but that changes the entire nature of bridging and does not constitute condensation frosting and thus such experiments were not conducted. All the scaling laws for the different droplet sizes as observed experimentally are depicted in the Figure 5.4.

We need to now discuss the various implicit assumptions associated with the above derivation. How appropriate is the assumption of a single droplet pair interaction, given that the ice bridging phenomenon happens in a condensate population? The experimental fact that an ice bridge is directed toward the nearest neighbor itself justifies that the pairwise interaction is the predominant cause for the growth of the ice bridge. The secondary effects of multi-droplet interaction can however become important in two distinct ways– the multi-sink effect and the multi-source effect. The multi-sink effect is observed when a single water droplet is surrounded by multiple ice droplets from all sides, in which case the mass of the evaporated liquid droplet is used to grow ice bridges from all the different ice droplet. This would serve to decrease the S_{Cr}^* as predicted using a pairwise interaction model. The multi-source effect on the other hand is when multiple liquid droplets (typically two) that are almost touching each other are the nearest neighbors of the ice droplet. This allows for
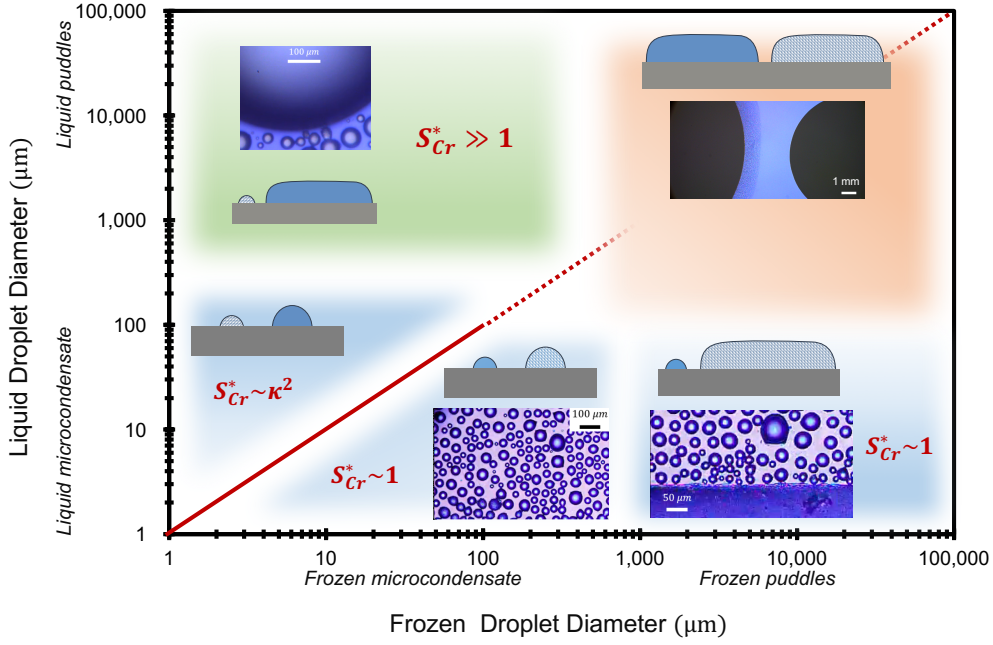
FIGURE 5.5: Phase map of the different experimentally observed scaling laws for the critical condition for ice bridge connections, based on the different sizes of droplets in the interacting pair. The blue shaded region indicates that ice bridge connections might succeed or fail depending on the conditions. The green shaded region, corresponding to a pair interaction between a frozen microcondensate and a liquid puddle, is where ice bridges, if initiated, are always successful in connecting. The red shaded region, corresponding to the a puddle pair interaction is never successful.

a longer bridge to be possible, thus increasing the value of S_{Cr}^*. Note that if a single frozen droplet is surrounded by liquid droplets, the inter-droplet separation between all the droplets being roughly the same, then the ice droplet would grow directed ice bridges toward all of the liquid droplets. Each of these ice bridges constitutes a single droplet pair interaction, as long as the liquid droplets themselves are not close to each other.

5.3 The Velocity Model and Observations

How can the inter-droplet pressure gradient be related to the growth rate of an ice bridge? Consider a liquid droplet adjacent to another droplet that has frozen over at some initial time $t_0 = 0$; the in-plane mass flux of the evaporating liquid droplet scales as:

$$\dot{m}_{l,e} \sim J_{l,e} A_\parallel \sim \frac{D}{\bar{R} T_w} \frac{p_{s,l} - p_{n,i}}{\delta_0} A_\parallel, \tag{5.2}$$

41
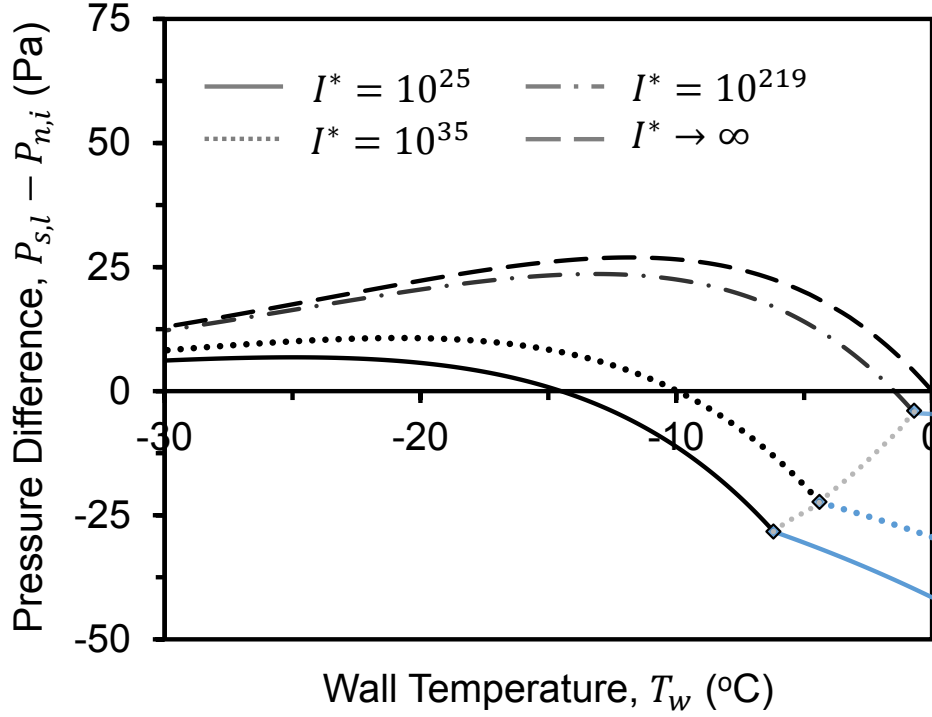
FIGURE 5.6: Theoretical difference between the saturation vapor pressure of water and the pressure required to nucleate on ice plotted with respect to temperature for different values of I^* (Eq. S4). The blue and black lines represent the condensation and desublimation modes of nucleation on ice respectively. The gray line tracks the inflection points where the change in the favorable mode of embryo nucleation on ice occurs for different I^* values. The solid line corresponds to $I^* = 10^{25}$, as used by Na et al. [7] for nucleation on ice. This gives a negative value of $p_{s,l} - p_{n,i}$ for $T_w > -15\,°C$ which is implausible given that ice bridging occurs at warmer temperatures. The dotted line represents $I^* = 10^{35}$ which is the lowest value of I^* that allows for ice bridging up to $T_w = -10\,°C$. The $I^* = 10^{219}$ curve (dot-and-dash) corresponds to the minimum value of $p_{s,l} - p_{n,i} = 264.6\,Pa$ inferred from experimental measurements of bridge growth rates at $T_w = -10\,°C$ as obtained previously by Boreyko and Collier [6] and correlated with our diffusive scaling model (Eq. 5.5). Finally, $I^* \to \infty$ (dashed) corresponds to saturated conditions at the growing ice interface ($p_{n,i} \approx p_{s,i}$), which we suggest is the best approximation.

42

where $p_{s,l}$ is the saturation pressure of the (presumably micrometric) liquid droplet and $p_{n,i}$ is the unknown vapor pressure adjacent to the interface of the ice droplet and growing ice bridge, where δ_0 is the edge-to-edge inter-droplet separation, and $A_\parallel$ is the in-plane projected area of the liquid droplet, and it is presumed that the droplet temperatures are approximately equal to the wall temperature. The in-plane mass flux of vapor growing the ice bridge is:

$$\dot{m}_{i,c} \sim \rho_i v_b A_\parallel, \tag{5.3}$$

where v_b is the in-plane growth rate of the bridge and $A_\parallel$ is the in-plane projected area of the frozen droplet. By conservation of mass, $\dot{m}_{l,e} \sim \dot{m}_{i,c}$. When the frozen droplet and (initial) liquid droplet are approximately same-sized, equating Eqs. 5.2 and 5.3 yields the following characteristic velocity of ice bridge growth:

$$v_b \sim \frac{D}{\rho_i \bar{R} T_w} \frac{p_{s,l} - p_{n,i}}{\delta_0}. \tag{5.4}$$

Note that the pressure differential $p_{s,l} - p_{n,i}$ is a function of temperature, so Eq. 5.4 reveals that v_b should simply scale inversely with δ_0 while also exhibiting a more analytically complex dependence on T_w. An interesting observation regarding Eq. 5.4 is that the partial pressure of water vapor in the ambient (p_∞) does not appear to have any effect on the propagation speed of the ice bridge, which is logical given that the bridge is entirely fueled by the liquid droplet [6]. However, note that extremely large values of P_∞ would serve to reduce the net evaporation rate of the liquid droplet being harvested by an ice droplet/bridge, such that the rule that bridging fails for $L_{max} > D_l$ may eventually break down.

Recall that it remains an open question whether the vapor pressure at the interface of growing frost is saturated or supersaturated. This issue is difficult to settle for the more conventional case of a macroscopic sheet of ice growing out-of-plane on a substrate, because matching the experimentally measured growth rates with a theoretical model can be simultaneously accomplished by assigning a supersaturated vapor pressure to the model or by modifying the diffusion resistance factor which is a function of the porosity/density of the ice sheet used in the model [131]. Here, we will demonstrate that the phenomenon of inter-droplet ice bridging can resolve this long-standing question of the vapor pressure required to grow ice.

Over the past several years, it has been repeatedly observed that ice droplets are able to grow ice bridges by siphoning water vapor from neighboring liquid droplets over a wide range of subfreezing surface temperatures, surface wettabilities, and ambient vapor pressures [6, 57, 59, 61, 63, 118–120, 145]. It should be emphasized that the ambient water vapor is not contributing appreciably to the growth of these inter-droplet ice bridges, as bridge growth is in-plane and exactly in the direction of the liquid droplet being harvested [6]. Therefore it can be asserted with extreme confidence that the vapor pressure around the ice droplets (and bridges) must be lower than the vapor pressure around the liquid droplets; otherwise, this source-sink behavior would be impossible. Previous reports have observed inter-droplet ice
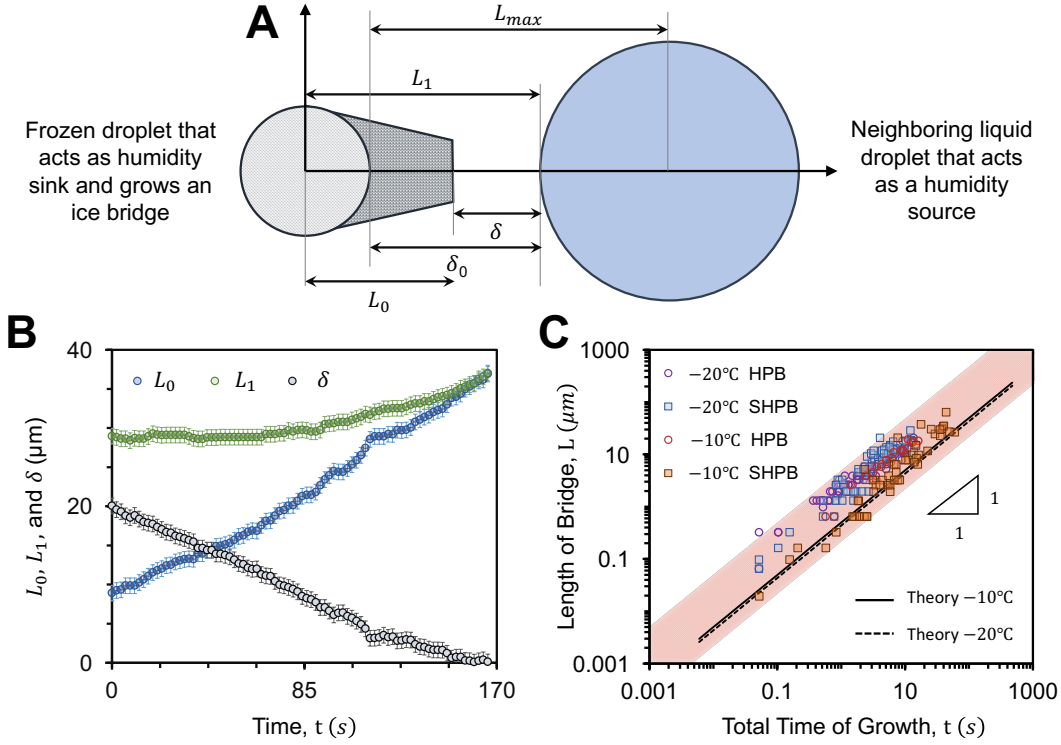
FIGURE 5.7: a) Definition sketch of droplet pair interaction. b) Dynamic evolution of ice bridge (L_0), the contact line of the liquid water droplet and intermittent distance between the bridge and the contact line (δ) for a droplet pair interaction with $\kappa > 1$ at a substrate temperature of $T_s = -10\,°C$. Note how the ice bridge growth rate remains constant. A straight line fit through L_0 gives a slope of 0.159 μm/s which is remarkably close to our theoretical estimate of 0.163μm/s. c) Lengths of ice bridges corresponding to both successful and failed connection plotted against the total time of growth Data points correspond to experiments performed on hydrophobic and superhydrophobic substrates at temperatures $T_s = -10\,°C$ and $-20\,°C$. The black theory lines correspond to an average inter-droplet separation of 10μm, while the shaded band corresponds to the minimum and maximum inter-droplet separation of 1μm and 20μm respectively.

bridging across populations of microscopic or even macroscopic condensate droplets [6, 57]; recall from Figure 3.5 that liquid droplets of this size exhibit a saturated vapor pressure. However, when using Na's assumption of $I^* = 10^{25}$ to estimate the vapor pressure around growing frost [7], $p_{s,l} - p_{n,i}$ is negative for all temperatures $T_w > -15\,°C$ (Figure 8.2b, solid line), which implies that inter-droplet ice bridging is impossible above $-15\,°C$. This is in contrast with the findings of Boreyko and Collier, where inter-droplet ice bridging was readily observed at $T_w = -10\,°C$ [6].

Therefore we now have experimental evidence that $I^* \sim 10^{25}$ is not a good assumption when considering nucleation on ice. In order to satisfy the criteria $p_{s,l} - p_{n,i} > 0$

at $T_w = -10\,°C$, the lowest possible value of the embryo kinetics is $I_{Cr}^* \sim 10^{35}$ (dotted line in Figure 8.2b). This corresponds to a maximum possible SSD over ice of $SSD_{Cr} \approx 0.1$ at $T_w = -10\,°C$. By referring to experimentally measured bridge growth rates ($v_{b,exp} = L(\tau)_{exp}/\tau_{exp}$), inter-droplet spacings (δ_{exp}), and wall temperatures ($T_{w,exp}$) previously obtained from Boreyko and Collier [6], the vapor pressure difference driving the growth of inter-droplet frost growth can be estimated as:

$$p_{s,l} - p_{n,i} = \delta_{0,exp} \left(\frac{\rho_i \bar{R} T_{w,exp}}{D} \right) v_{b,exp}. \tag{5.5}$$

At $T_w = -10\,°C$, experimental measurements plugged into Eq. 5.5 predict a pressure differential of $p_{s,l} - p_{n,i} = 21.8\,\text{Pa}$, corresponding to the experimentally obtained minimum bridge growth rate of $v_b = 0.4\,\mu m/s$ for an average $\delta_{exp} = 9.8\,\mu$m. This corresponds to $I^* \sim 10^{219}$ (Figure 8.2b, dash-and-dot line) and $SSD = 0.018$. For $I_0 = 10^{29}\,\text{m}^{-2}\text{s}^{-1}$, it follows that $I_c = 10^{-190}\,\text{m}^{-2}\text{s}^{-1}$. Such a small value of I_c means that the threshold rate at which embryos spontaneously nucleate is essentially zero. Correspondingly, for $I_c \to 0$, we have $p_{n,i} \to p_{s,i}$, such that the vapor pressure at the interface of a growing ice can be considered to be saturated for all intents and purposes (dashed line in Figure 8.2b). This is also consistent with our observation that for heterogeneous nucleation on a substrate, $SSD \to 0$ in the hydrophilic limit $\theta \to 0$ (Figure 3.3). The same inferences can be drawnfrom Figure 5.6 which shows that the evolution of ice bridges over a wide parameter space for both hydrophobic and superhydrophobic substrates at two different substrate temperatures are accurately captured with our velocity model where saturation vapor pressure of ice is used as the vapor pressure at the ice interface. Thus we propose that the vapor pressure adjacent to growing frost is approximately saturated, in agreement with an extremely recent work that used laser confocal microscopy and differential interference contrast microscopy to observe that the equilibrium pressure of ice is indeed aligned with the saturation curve [150].

5.4 Experimental Methods

4 in. silicon wafers (Silicon Quest) were silanized with Trichloro(1H, 1H, 2H, 2H–perfluorooctyl) silane (Sigma-Aldrich) by vapor deposition in a covered glass petri dish that was placed on a hot plate set to $70\,°C$ for 1 hr. The contact angles were measured with a ramé-hart 590 Goniometer using the shrink-swell method. The receding angle was measured as $\theta_r = 89°\pm 1°$ and the advancing angle was $\theta_a = 113°\pm 1°$.

A freshly prepared hydrophobic surface was thermally bonded to a Peltier stage (Linkam Scientific PE120) and placed under a top-down optical microscope (Nikon Eclipse LV150) connected to a digital camera (Phantom v711). The ambient temperature was $T_\infty = 24.0\,°C$ and the relative humidity was $H = 26\,\%$ which corresponds to a dew point of $T_{DP} = 3.3\,°C$. The sample was cooled to $T_w = -10\,°C$ to grow supercooled condensate. Once freezing initiated in at least one of the condensate

droplets (often at the edges of the silicon wafer), inter-droplet ice bridges propagated across the population of supercooled condensate which was recorded with the digital camera. A separate set of similar experiments were performed at $T_\infty = 22.0\,°C$ and the relative humidity was $H = 45\,\%$, where two different substrate temperatures $T_w = -10$ and $-20\,°C$ were used. For puddle-puddle interaction experiments, two $100\,\mu L$ droplets were deposited in the vicinity of each other on the hydrophobic substrate inside the humidity chamber. The humidity chamber was set to near-zero humidity and the sample was cooled to $T_w = -10\,°C$.

5.4.1 Estimation of Thermal Losses

The thickness of our silicon wafer samples was $t_{silicon} \approx 550\,\mu m$ and that of the silane monolayer was $t_{silane} \approx 1$ nm. The thermal conductivity of silicon and a silane monolayer are known to be $k_{silicon} = 150$ W/m·K and $k_{silane} = 0.2$ W/m·K respectively [162]. For our experimental conditions, the typical velocity of vapor was $v_v \sim D\left(p_\infty - p_{s,w}\right)/\left(\rho_v \bar{R} T_w \zeta\right) \sim 1$ cm/s where D and ρ_v are the diffusivity and density of water vapor, $\bar{R}$ is water vapor gas constant, T_w is the temperature of the substrate, p_∞ is the vapor pressure at the boundary layer, $p_{s,w}$ is the saturation vapor pressure corresponding to the wall temperature and ζ is the boundary layer thickness [164]. For the experimental conditions described above, where $T_w = -10\,°C$ and $p_\infty = 776\,Pa$, we obtain $v_v \approx 3.9\,cm/s$ which corresponds to a low heat flux of $q = \rho_v v_v h_{l,v} \approx 0.56$ kW/m^2. The surface coverage of droplets in dropwise condensation typically plateaus around 65%, assuming which the average heat flux flowing through the condensate can be estimated as $q_d \approx 0.87$ kW/m^2. The amount of heat flux flowing through each droplet can be estimated as $Q_d = q_d \pi r^2 \sin^2 \theta$ (in Watts) where r is the radius of curvature and θ is the contact angle of the drop. The temperature drop across the silicon wafer was estimated to be $\Delta T_{silicon} = Q_d t_{silicon}/(\pi r^2 k_{silicon} \sin^2 \theta) \approx 0.003\,°C$ and the temperature drop across the silane coating was $\Delta T_{silane} = Q_d t_{silane}/(\pi r^2 k_{silane} \sin^2 \theta) \approx 4.3 \times 10^{-6}\,°C$. Furthermore, the thermal loss due to conduction through a micrometric droplet ($r = 10\,\mu m$ and $\theta \approx 90°$) was estimated as $\Delta T_{cond} = Q_d \theta/(4\pi r k_w \sin \theta) \approx 0.006\,°C$. Therefore, as the thermal losses across the substrate, the coating and the drop in our system are extremely small, we can assume the droplet temperature to be the same as the temperature at which the Peltier stage was set at, that is, $T_d \approx T_w$ for our experiments on condensation dry zone, inter-droplet ice bridging and dry zones around frozen droplet.

6

Controlling
Frost Growth

"There is another organism on this planet that follows the same pattern.
Do you know what it is?
A virus. "

$-Agent\ Smith$

6.1   Intoduction

In the previous chapter, we saw how the success of local inter-droplet ice bridge connection depends on the inter-droplet spacing. Here, we demonstrate that when the separation between adjacent nucleation sites for supercooled condensate is properly controlled with chemical micropatterns prior to freezing, global frost propagation can be slowed and even halted entirely. Since the edge-to-edge separation between adjacent supercooled droplets decreases with growth time, deliberately triggering an early freezing event to minimize the size of nascent condensation was also necessary. These findings reveal that inter-droplet frost growth can be passively suppressed by designing surfaces to spatially control nucleation sites and by temporally controlling the onset of freezing events.

Previous works on anti-frosting have almost exclusively concentrated on delaying ice nucleation as it was widely assumed that the primary mechanism of condensation frosting for surfaces promoting dropwise condensation was the heterogeneous nucleation of ice at the solid-liquid interface of each individual supercooled droplet [53–56]. Numerous reports have observed that heterogeneous nucleation can be delayed by minutes or even hours for supercooled droplets deposited on superhydrophobic surfaces compared to traditional surfaces, due to the hydrophobicity increasing the energy barrier for nucleation [89, 91, 94] and because the air pockets trapped by a suspended Cassie droplet reduce the heat transfer rate [91, 93, 102] and minimize the solid-liquid contact area where nucleation events can occur [84, 86, 89, 91, 93, 94]. Condensed droplets can also grow in a Cassie state on nanostructured superhydrophobic surfaces [160, 165, 166], such that supercooled condensate can exhibit delayed heterogeneous nucleation in the same manner as with deposited droplets [54–56]. Furthermore, the minimal contact angle hysteresis of Cassie droplets on superhydrophobic surfaces can be exploited to dynamically remove supercooled droplets before heterogeneous nucleation occurs at all. Examples include deposited droplets that were gravitationally removed by sliding [86, 102] or rebound [105, 106, 167] and condensed droplets that were removed by gravity at millimetric length scales [95, 103] or by coalescence-induced jumping at micrometric length scales [6, 58, 59]. It would therefore seem that nanostructured superhydrophobic surfaces should be able to completely prevent the onset of condensation frosting, by delaying heterogeneous nucleation long enough to dynamically remove supercooled condensate from the surface.

Curiously, it was observed that even when supercooled condensate was continually removed from a superhydrophobic surface via coalescence-induced jumping before heterogeneous nucleation occurred, frost still grew over the surface [6]. This was attributed to an unexpected phenomenon where only a single droplet had to freeze due to heterogeneous nucleation (typically at edge defects where jumping did not occur), at which point the frozen droplet harvested water from nearby liquid droplets, growing ice bridges that connected across the forming condensate in an unstoppable chain reaction [6, 57]. This source-sink vapor interaction between an evaporating

liquid droplet and a bridging frozen droplet is most likely due to the higher water vapor pressure over liquid water compared to frozen water [5, 9, 20]. Since the mass of the ice bridge is harvested from the liquid droplet, it follows that the liquid droplet can completely evaporate before the ice bridge connects when the inter-droplet spacing is sufficiently large [6, 57]. To date, no surface has been able to completely stop the inter-droplet growth of frost when a freezing event occurs near the population of supercooled condensate [57, 61, 118–120]; typically ice bridges connect for nearly every droplet on smooth hydrophobic surfaces and for approximately 1/3 of droplets on jumping-droplet superhydrophobic surfaces [6].

Inspired by the *Stenocara* desert beetle [168], the nucleation sites for condensation can be spatially controlled on engineered surfaces exhibiting chemical patterns of contrasting hydrophobic and hydrophilic regions, due to the dramatically lower energy barrier for nucleation on the hydrophilic features [72, 143, 169–172]. Chemically patterned substrates have been shown to enhance water harvesting [69–71] and phase-change heat transfer [64, 66, 173], and are also useful for controlling liquid morphology [174, 175], tuning droplet hysteresis [176, 177], controllably depositing micro/nano-materials [178], and lab-on-a-chip applications [179, 180]. Now that it is understood that condensation frosting is dependent upon the spatial distribution of droplets, the ability of a chemically patterned surface to control nucleation sites seems ideal for characterizing and controlling inter-droplet frost growth. However, to date there have been no reports using chemically patterned surfaces to characterize the spatial distribution of condensation or the related dynamics of inter-droplet frost growth.

Here, we demonstrate that chemical patterns can be used to tune the spatial distribution of supercooled condensation and subsequently control the geometry and speed of inter-droplet frost growth. The success and rate of inter-droplet frost growth was found to be dependent upon two primary factors: the extent of spacing between hydrophilic regions where liquid nucleation occurred and the time allowed for condensation growth prior to the initial freezing event. For the first time, inter-droplet ice bridging could be completely halted by utilizing sufficiently sparse hydrophilic patterns and by quickly triggering a freezing event near the patterned condensation.

6.2   Methods

6.2.1   Sample fabrication

Silicon wafers (4 in., Silicon Quest) were first cleaned with Piranha solution (3:1 H_2SO_4:H_2O_2 at 25 °C for 10 min), rinsed extensively in deionized water, and dried with nitrogen. Clean wafers were functionalized with trichloro(1H, 1H, 2H, 2H − perfluorooctyl) silane (Sigma-Aldrich) through vapor deposition in a covered glass petri dish heated to 80 °C for 1 hr. Parylene was then deposited onto the silanized wafers using 800 mg of 2,2-paracyclophane precursor (Sigma) loaded into a parylene coater (SCS Labcoter 2, Specialty Coating Systems) run under standard operating

conditions. Next, MP−P20 adhesion promoter (MicroChem) and S1818 photoresist (Shipley) were respectively spin-coated onto the wafer, both at 3,000 rpm for 45 s. After a 60 s bake at 115 °C, the wafer was exposed to ultraviolet light at 10 mW/cm^2 at 365 nm for 5 s (Quintel Mask Alignment System) and developed in CD−26 for 2 min, rinsed with deionized water, and dried with nitrogen gas.

The wafer was then etched with oxygen plasma in an inductively coupled plasma ion etching system (Oxford Plasmalab 100, Oxford Instruments) for 30 min The etch rate under these conditions was approximately 62 nm/min, such that 30 min was sufficient to etch through the exposed parylene (1.25 μm thick) and the remaining photoresist (1.75 μm thick) while preserving the parylene that was underneath the photoresist. Immediately before use, the wafer was etched in oxygen plasma for 1−3 min to ensure that the exposed silicon oxide regions were hydrophilic, followed by a dry peel-off of the parylene film using tape and tweezers [181] to expose the hydrophobic silane monolayer.

6.2.2   Condensation experimental procedure

A freshly prepared silicon sample was bonded to a Peltier stage (Deben MK3 Coolstage) with thermal paste and placed under a top-down optical microscope (Nikon Eclipse LV150). The ambient temperature was $T_\infty = 21.3 \pm 0.3$ °C and the relative humidity was $H = 40 \pm 3\%$, corresponding to a dew point of $T_{DP} = 7.2 \pm 1.3$ °C. The substrate was initially kept dry at 10 °C and was then cooled beneath the dew point to 5 °C to allow condensation to form in order to make the patterns visible. The desired pattern type (circles, triangles, or stripes) was centered and focused under a 5× objective lens, such that the 2P, 4P and 8P arrays were all visible within the microscope's field-of-view.

Once the field-of-view was set, the sample was immediately heated to 40 °C to dry the surface. The wafer was then cooled back down to 10 °C, followed by further cooling to either 5 °C or −10 °C to observe the resulting condensation with a digital camera (Nikon DS-5M) attached to the microscope. The transient of the Peltier stage was 5 ± 1 s to cool from 10 °C to 5 °C and 30 ± 1 s to cool from 10 °C to −10 °C. The forming condensation was imaged for 10 min, and the surface was then heated back to 40 °C to dry out the surface for the next trial. Three trials were obtained for both condensation temperatures and a new chip was used for each pattern type to minimize surface contamination.

6.2.3   Image Analysis of Condensation

A stack of images from each condensation video were analyzed in ImageJ, with a time interval of 3.0 s between each frame. For arrays of circles or triangles, there were 140, 507, and 1,925 hydrophilic features within the field of view for $P = 2$, 4, and 8 respectively. For arrays of stripes, there were 20, 39, and 77 stripes in the field of view for $P = 2$, 4, and 8 respectively. Each stack was cropped to analyze each

array (2P, 4P, or 8P) in isolation. Each cropped stack was digitally sharpened and then converted to a binary mask. For the 4P and 8P arrays, the 'Fill Holes' process was performed to fill in holes in the droplets caused by reflected light, followed by the 'Watershed' process to ensure that droplets that were close to coalescing were not counted as a single droplet. The 'Analyze Particles' procedure was then performed to measure droplet diameters and surface coverage. For the 2P array, the droplets were too small for the 'Fill Holes' process to work accurately, so the following alternate approach was taken for the image processing. After sharpening the image and converting to binary, the 'Close' process was used to fill in the holes of the droplets, followed by 'Erode,' 'Watershed,' 'Dilate,' and 'Watershed,' respectively to separate nearby droplets from each other.

6.2.4   Condensation frosting experimental procedure

Under the same atmospheric conditions as with the condensation experiments ($T_\infty = 21.3 \pm 0.3\,°C$ and $H = 40 \pm 1\%$), the desired pattern was centered and focused under the microscope by condensing water at $5\,°C$, followed by drying at $40\,°C$ and holding steady at $10\,°C$. The field-of-view under the microscope included a large rectangular hydrophilic region that bordered the hydrophilic arrays on one edge of the wafer. A $2.5\,\mu L$ droplet of deionized water was deposited onto this rectangular hydrophilic pad, followed by cooling down to $-10\,°C$ to induce the growth of supercooled condensation on the hydrophilic array. The array in the field-of-view included 2P, 4P, and 8P features that were either circles, triangles, stripes running parallel to the deposited water droplet, or stripes running perpendicular to the deposited water droplet. To trigger inter-droplet ice bridging across the patterned condensation, a small piece of ice was gently touched against the side of the wafer containing the deposited water film to freeze it. To vary the rate of frost growth, the water pad was frozen at different times ($0\,s$, $30\,s$, $60\,s$, $90\,s$, $120\,s$, or $270\,s$), where time zero corresponds to the instant where the surface finishes cooling to the set point temperature of $-10\,°C$. The resulting frost growth was characterized by dividing the square root of the total area of each array by the time required for it to frost over. It should be noted that in addition to inter-droplet ice bridging, the frost growth for these experiments was also affected by ice shrapnel, where freezing droplets sprayed small particles of ice over the surface that induced non-local ice bridging events in addition to those caused by the initial freezing event.

Condensation frosting was characterized a second time in a less humid environment that suppressed the ice shrapnel, in order to isolate the kinetics of localized inter-droplet ice bridging from a single freezing event. This second set of experiments was nearly identical to the methods described above, except now $T_\infty = 24.0 \pm 0.9\,°C$ and $H = 26 \pm 2\%$ corresponding to a dew point of $T_{DP} = 3.3 \pm 1.9\,°C$. The surface was initially held at 3 degrees above the dew point, and cooled down to a steady-state temperature of $T_s = -10\,°C$ which took approximately $30\,s$. The hydrophilic pad of deposited water was frozen at three different times ($1\,min$, $3\,min$, or $5\,min$) after

reaching the steady-state temperature for all 2P and 4P shapes, with three trials performed for each parameter. The resulting frost growth was imaged to measure the averaged velocity of frost growth, in an identical manner to the first set of experiments. Finally, to capture a stable dry zone (Fig. 8), the surface was initially held at the lowest possible temperature of $T_s = 1\,°C$ where no condensation formed; while this was below the theoretical dew point by a few tenths of a degree, this can be attributed to the small thermal resistance between the Peltier stage and the substrate or because vapor can become supersaturated at a surface without condensing due to the energy barrier for nucleation. The surface was then cooled down to $T_s = -5\,°C$ and the water pad was immediately frozen, to minimize the value of S^*. Once the pad was frozen and the ice began to harvest water from the condensation, the surface was then cooled to a final temperature of $T_s = -12.5\,°C$ to demonstrate the long-term stability of the dry zone even under highly supersaturated conditions.

6.3   Results

6.3.1   Chemical micropatterns

Arrays of hydrophilic features were patterned against a hydrophobic backdrop on a silicon wafer using photolithography (see Methods and Supplementary Fig. S1). The hydrophilic areas were composed of bare silicon oxide and the hydrophobic areas were comprised of a silane monolayer. Immediately before experimental characterization, each wafer was exposed to an oxygen plasma to restore the full hydrophilicity of the silicon oxide features, followed by a dry peel-off of the patterned parylene coating [181] that was protecting the hydrophobic monolayer. Atomic force microscopy revealed that the silanized regions were uniformly elevated by $1.5 \pm 0.5\,nm$ relative to the bare hydrophilic features, confirming the presence of a self-assembled monolayer (Supplementary Fig. S2). This extreme smoothness is ideal for characterizing the effects of wettability patterns on condensation and frost growth without any conflating topological effects such as polymers [70, 171], surface deformation from a focused ion beam [182], or structured superhydrophilic and/or superhydrophobic surfaces [64, 66, 69, 71, 72, 170–172]. Indeed, the patterns were completely invisible even when observed under an optical microscope, and could only be revealed via condensation which preferentially formed on the hydrophilic features (Fig. 1).

The hydrophilic features exhibited a characteristic length scale of $a = 10\,\mu m$ and were shaped like circles, triangles, horizontal stripes, or vertical stripes. The pitch between features is defined as $P = b/a$, where b is the center-to-center separation between features. The geometry and pitch were systematically varied by fabricating arrays of pitch $P = 2$, 4, or 8 for each shape. The total width of each array is $490\,\mu m$, with $250\,\mu m$ of space between arrays, such that the field-of-view of the microscope can simultaneously observe three different arrays (Fig. 1). For the circles, triangles, and vertical stripes, this corresponded to 25, 13, and 7 features per row for $P = 2$, 4, and 8 respectively, whereas horizontal stripes compose the entire width of their array.
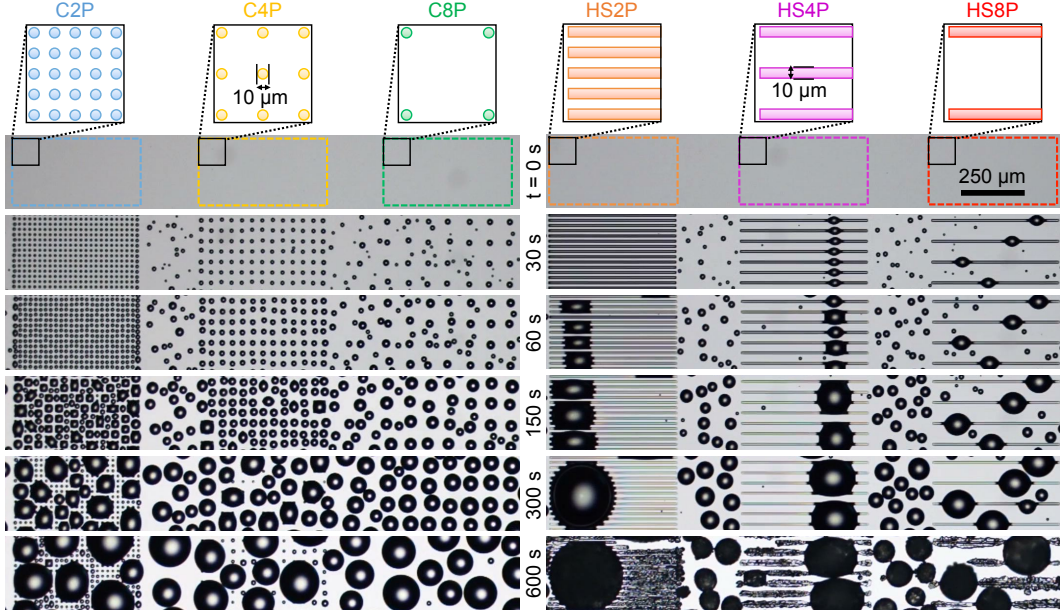
FIGURE 6.1: Spatial control of condensation on smooth chemical micropatterns composed of arrays of circles or stripes. The colored shapes in the schematics represent the hydrophilic features while the white background is hydrophobic. Time zero corresponds to the onset of cooling from 10°C down to a steady-state temperature of $T_s = -10\,°\text{C}$ from 30 s onward.

For simplicity, arrays will henceforth be referred to by a notation corresponding to their shape and pitch. For example, when $P = 2$, circles are C2P, triangles T2P, horizontal stripes HS2P, and vertical stripes VS2P.

6.3.2 Spatial Control of Condensation

Condensation was grown on the patterned surface by cooling the substrate to either $T_s = 5\,°\text{C}$ (Supplementary Fig. S3) or $T_s = -10\,°\text{C}$ (Fig. 1) in a clean room where the ambient temperature was $T_\infty = 21.3 \pm 0.3\,°\text{C}$ and the relative humidity was $H = 40 \pm 3\%$. The nucleation density of condensation is dependent upon the supersaturation of the system's water vapor, which is typically defined as:

$$S = \frac{P_\infty}{P_s(T_s)}, \tag{6.1}$$

where P_∞ is the partial pressure of water vapor in the ambient, while $P_s(T_s)$ is the saturation vapor pressure corresponding to the temperature of the condensing surface. Here, $S = 1.2$ for $T_s = 5\,°\text{C}$ and $S = 3.9$ for $T_s = -10\,°\text{C}$. Note that the growth of patterned condensate on the triangle arrays was nearly identical to that on the circle arrays (Supplementary Figs. S4−S6), and that the distinction between horizontal stripes and vertical stripes is only important for the later experiments

involving frost growth. To avoid redundancy, discussion of patterned condensation will therefore be confined to the arrays of circles and horizontal stripes.

From classical nucleation theory [149], the energy barrier for heterogenous nucleation of condensate is a function of surface wettability:

$$\Delta G = \frac{\pi\gamma r_c^2(2 - 3\cos\theta + \cos^3\theta)}{3}, \tag{6.2}$$

where γ is the liquid-vapor surface tension, r_c is the critical radius for stable nucleation, and θ is the contact angle of the nucleated droplet. Here, the receding contact angle was $\theta_r = 12° \pm 2°$ and the advancing angle was $\theta_a = 45° \pm 2°$ for the hydrophilic regions, while $\theta_r = 89° \pm 1°$ and $\theta_a = 113° \pm 1°$ for the hydrophobic regions. Assuming that a freshly nucleated droplet exhibits θ_r to minimize the energy barrier, ΔG is larger for the hydrophobic regions by a factor of $\approx 1{,}370$.

For each array it was observed that every hydrophilic feature promoted the early, preferential nucleation of condensate that conformed to the shape of the feature during early droplet growth (Fig. 1). However, whether any condensation additionally nucleated on the hydrophobic background between the hydrophilic features depended upon two primary factors: the pitch of the hydrophilic patterns and the supersaturation. At $S = 1.2$, condensation exclusively nucleated on the hydrophilic patterns when $P = 2$ or $P = 4$, while a tiny minority of droplets nucleated on the hydrophobic backdrop for $P = 8$. At $S = 3.9$, spatial control was only perfect for $P = 2$, while droplet nucleation on the hydrophobic background was occurring to a very small extent for $P = 4$ and to a much larger extent for $P = 8$, such that the pattern of wetted hydrophilic features became somewhat difficult to discern. The magnitude of the dry zone was stochastic in nature; for example, at $S = 1.2$ a droplet occasionally nucleated only $\approx 15\mu$m from a hydrophilic feature, but at the same time, the $250\,\mu$m of hydrophobic space between arrays tended to remain almost completely dry (Supplementary Fig. S3). Assuming that the lower extreme of dry zone lengths is influenced by minor chemical or physical defects (evidenced by the tendency of the nearest condensate to appear in the exact same place over multiple trials), an order of magnitude approximation of the dry zone length about a hydrophilic feature in the absence of defects scales as $\sim 100\,\mu$m for $S = 1.2$ and $\sim 10\,\mu$m for $S = 3.9$.

The dry zone on the hydrophobic surface can be modeled as a competition between the system's in-plane and out-of-plane vapor pressure gradients. These pressure gradients could facilitate a dry zone in two different ways: by inhibiting the nucleation or by inhibiting the growth of liquid condensate. Let's consider both in turn, beginning with an inhibited-nucleation dry zone of critical length δ_{IN}. From classical nucleation theory [7, 149], the supersaturated vapor pressure required to overcome the free energy barrier for liquid nucleation on the hydrophobic surface can be estimated as $P_n = 1{,}072$ Pa for $T_s = 5\,°$C and $P_n = 371$ Pa for $T_s = -10°$ C. Assuming an isolated, hemi-spherical droplet filling a hydrophilic feature ($r = 5\,\mu$m), there is a hyperbolic pressure distribution, $\nabla^2 P = 0$, extending radially from the droplet's saturated interface ($P_s = 873$ Pa for $T_s = 5\,°$C and $P_s = 286$ Pa for $T_s = -10°$ C [20])

toward the ambient ($P_\infty = 1{,}194\,\mathrm{Pa}$). The critical distance from the perimeter of the droplet to where nucleation can first occur on the hydrophobic surface is $\delta_{IN} = 8.2\,\mu\mathrm{m}$ for $5\,^\circ C$ and $\delta_{IN} = 0.5\,\mu\mathrm{m}$ for $-10\,^\circ C$.

Even when the vapor pressure is sufficient for nucleation to occur, it is possible that the nucleated droplet will simply evaporate under certain conditions. Nucleating embryos are typically $\sim 1\,\mathrm{nm}$ in size [149]. For droplets exhibiting nanometric radii of curvature, the vapor pressure is significantly modified by the Kelvin-Laplace Equation:

$$\frac{2\gamma}{r} = \frac{RT}{v}\ln\frac{P_a}{P_s},\tag{6.3}$$

where r is the radius of curvature of the droplet, R is the universal gas constant, $T \approx T_s$ and v are the temperature and molar volume of the water droplet, and P_s and P_a are the saturated and actual vapor pressures about the droplet. Consider an isolated $r = 10\,\mathrm{nm}$ hemi-spherical droplet that has recently nucleated on the hydrophobic surface and is situated near a wetted hydrophilic feature on either side. The vapor pressure about the droplet is $P_a = 909\,\mathrm{Pa}$ at $T_s = 5\,^\circ\mathrm{C}$ and $P_a = 301\,\mathrm{Pa}$ at $T_s = -10^\circ\,\mathrm{C}$, such that $P_\infty > P_a > P_s$. Thus, even when nucleation is possible, the region will remain microscopically dry if the in-plane gradient driving evaporation exceeds the out-of-plane gradient facilitating condensation. The out-of-plane mass flow rate of vapor into the droplet scales as $\dot{m}_c^w \sim r^2 J_c^w \propto r^2 (P_\infty - P_a)/\zeta$, where J_c^w is the mass flux and ζ is the concentration boundary layer thickness, while the in-plane (evaporation) mass flow rate gives $\dot{m}_e^w \sim r^2 J_e^w \propto r^2 (P_a - P_s)/\delta$, where δ is the edge-to-edge distance from the droplet to a wetted hydrophilic feature. The critical length scale of the inhibited-growth dry zone, δ_{IG}, can be estimated by balancing the evaporation and condensation rates, $\dot{m}_c^w \sim \dot{m}_e^w$ [9], which gives:

$$\frac{\delta_{IG}}{\zeta} \sim \frac{P_a - P_s}{P_\infty - P_a}.\tag{6.4}$$

For diffusive transport, the concentration boundary layer scales as:

$$\zeta \sim \left[\frac{D\delta_h^{3/2}}{\left(4\sqrt{\beta g(T_\infty - T_s)}\right)}\right]^{1/3},\tag{6.5}$$

where D is the diffusion coefficient of water vapor, $\delta_h \sim L_s\left(g\beta(T_\infty - T_s)L_s^3/\nu^2\right)^{-1/5}$ is the hydrodynamic boundary layer, β and ν are the volumetric thermal expansion coefficient and kinematic viscosity of air, and $L_s \approx 1\,\mathrm{cm}$ is the characteristic length of the condensing surface [8]. This yields $\zeta \approx 0.9\,\mathrm{mm}$ and $\delta_{IG} \approx 115\,\mu\mathrm{m}$ for $T_s = 5\,^\circ\mathrm{C}$, and $\zeta \approx 0.8\,\mathrm{mm}$ and $\delta_{IG} \approx 13\,\mu\mathrm{m}$ for $-10^\circ\,\mathrm{C}$.

Therefore $\delta_{IG} > \delta_{IN}$ for the conditions used in the present experiments, such that nanometric condensate is able to nucleate within the majority of the dry zone, but subsequently evaporates. For $T_s = 5\,^\circ\mathrm{C}$, the predicted length of the inhibited-growth dry zone ($\delta_{IG} \approx 115\,\mu\mathrm{m}$) agrees with the experimental trend ($\sim 100\,\mu\mathrm{m}$), as does the prediction of $\delta_{IG} \approx 13\,\mu\mathrm{m}$ with the empirical observation of $\sim 10\,\mu\mathrm{m}$ for $T_s = -10\,^\circ\mathrm{C}$.
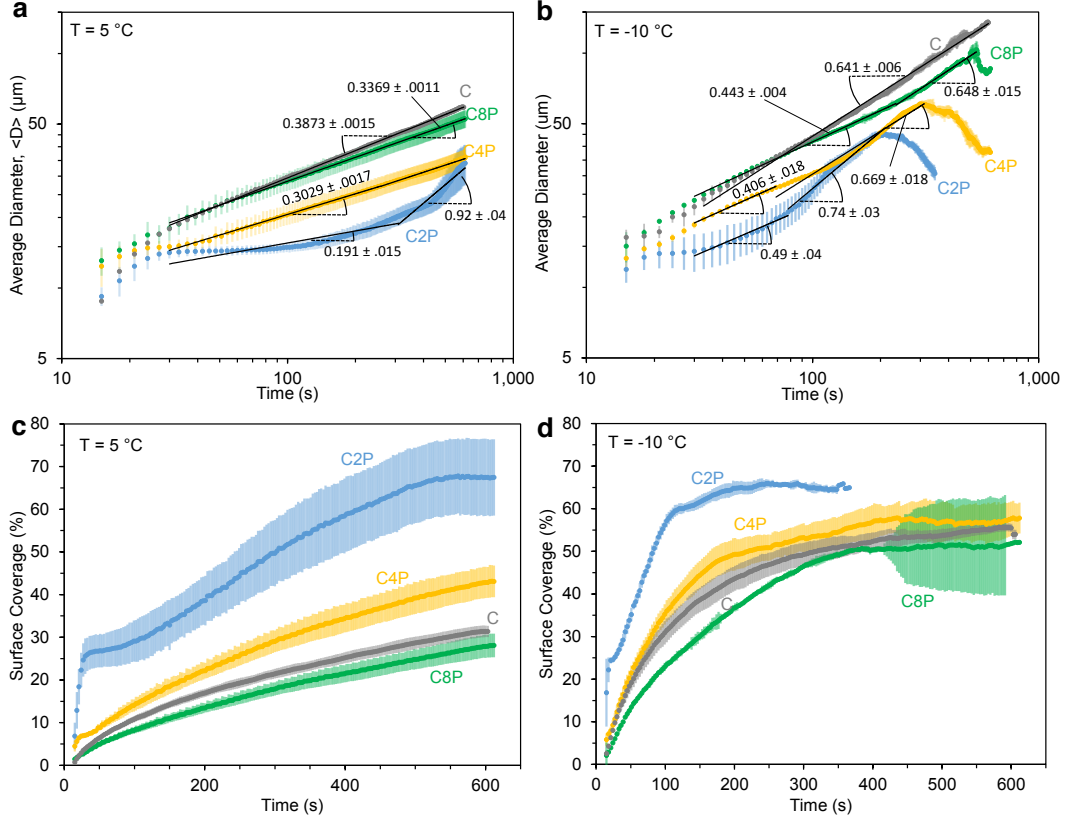
FIGURE 6.2: Growth of condensation on hydrophilic circle arrays of varying pitch (C2P, C4P, and C8P) or a uniformly hydrophobic control surface (C). (**a,b**) Average diameter of condensation growing at a supersaturation of $S = 1.2$ ($T_s = 5\,°C$) or $S = 3.9$ ($T_s = -10\,°C$), respectively. Slopes of trendlines correspond to the power law exponent α (Equation (6.6)) within a 95% confidence interval. (**c,d**) Projected surface coverage of condensation at $S = 1.2$ or $S = 3.9$, respectively. For all plots in this section, data points correspond to an average of three trials and all error bars correspond to a standard deviation.

6.3.3 Growth of Patterned Condensation

The average diameter ($<D>$) and surface coverage (ϵ^2) of condensate growing on the circle arrays was quantitatively extracted from the microscopy videos using ImageJ and compared to a control surface (C) that was uniformly hydrophobic (Fig. 2). On homogenous surfaces, it is now well established that dropwise condensation exhibits a power-law growth:

$$<D> \sim t^\alpha \tag{6.6}$$

where isolated droplet growth follows $\alpha \approx 1/3$ and $\alpha \approx 1$ once regular coalescence events occur at a near-constant surface coverage (i.e. self-similar growth) of $\epsilon^2 \approx 0.55$ [8, 78]. Note that $<D>$ was only measured for $t \geq 30\,s$ to ensure that the substrate temperature had finished cooling to its steady-state temperature.

56

For $S = 1.2$, $\alpha = 0.3878$ for C (Fig. 2a), which is slightly higher than $\alpha \approx 1/3$ most likely due to the onset of some early (but not self-similar) coalescence events. No coalescence events occurred in the recorded time range (600 s) for C8P, and the resulting $\alpha = 0.3369$ is in perfect agreement with the $\alpha \approx 1/3$ rule for isolated growth. Interestingly, the isolated growth of condensate followed $\alpha = 0.3029$ for C4P and $\alpha = 0.191$ for C2P, the latter of which is significantly lower than the $\alpha \approx 1/3$ rule for homogeneous surfaces. Compared to the control surface (C), the nucleation density was observed to be about 3 times larger for C4P and 13 times larger for C2P (Supplementary Fig. S7); we hypothesize that at low supersaturations, this dramatic increase in nucleation density caused by the hydrophilic features can increase the thickness of the water vapor concentration boundary layer, resulting in the reduced growth rate. For $S = 1.2$, only the C2P surface was able to reach a plateau surface coverage within the 600 s of recording; the growth rate of $\alpha = 0.92$ is in good agreement with the $\alpha \approx 1$ rule.

For $S = 3.9$, the isolated growth of condensate on the patterned surfaces ranged from $0.4 < \alpha < 0.5$ (Fig. 2b), somewhat larger than the $\alpha \approx 1/3$ rule. It is therefore likely that hydrophilic patterns serve to enhance the growth rate of isolated condensation at high supersaturations, as the patterns serve to funnel the vapor diffusing toward the surface almost exclusively toward the hydrophilic regions. In other words, hydrophilic patterns can either enhance (by funneling vapor) or diminish (by increasing the boundary layer) the growth rate of condensation, depending upon the extent of supersaturation. However, even with the enhanced growth rates, it should be noted that the patterned surfaces exhibited smaller values of $< D >$ compared to the control surface because the nucleation events were synchronized to minimize the variance in droplet volumes. At later times, where coalescence events were occurring at a steady-state surface coverage, $0.6 < \alpha < 0.75$. While this is lower than the theoretical trend of $\alpha \approx 1$, experimental measurements often hew closer to $\alpha \approx 0.75$; this discrepancy could be attributed to the presence of non-condensable gas, an over-simplified assumption of constant vapor flux, or the smallest droplets not being visible under the microscope objective [78]. After several minutes of coalescence-induced growth on the patterned surfaces, the value of $< D >$ actually decreased due to the coalesced droplets re-exposing many of the hydrophilic features to promote fresh nucleation events. This is in sharp contrast to condensation on the uniformly hydrophobic regions (cf. hydrophobic region between C2P and C4P in Fig. 1 at 600 s), where dry zones exist about the larger droplets [143, 144] due to inhibited nucleation and/or growth as modeled in the previous section.

Surface coverage generally varied as $\epsilon_{C8P}^2 < \epsilon_C^2 < \epsilon_{C4P}^2 < \epsilon_{C2P}^2$ (Fig. 2c, d). While C2P, C4P, and C8P all exhibited smaller $< D >$ than C, only C8P was able to achieve a smaller ϵ^2 than C. This observation reveals that chemical patterns are not very effective for minimizing surface coverage relative to a uniformly hydrophobic surface, as the benefit of the hydrophilic patterns keeping the hydrophobic background dry is offset by the enhanced nucleation and growth of condensation on the hydrophilic regions. Indeed, the plateau value of surface coverage for C2P was

$\epsilon^2 \approx 0.65$ (Fig. 2d), which is larger than the typically observed value of $\epsilon^2 \approx 0.55$ for a uniform hydrophobic surface.

While the concept of $< D >$ does not translate to the striped patterns, the surface coverage of HS2P, HS4P, and HS8P was analyzed (Fig. 3a, b). It was observed that $\epsilon^2(t)$ exhibited dramatically different behavior for the arrays of stripes compared to the arrays of circles or the control surface. First, condensation that nucleated within each hydrophilic stripe almost immediately spread out to cover the entire area of the stripe, resulting in very large plateau values of ϵ^2 (particularly for HS2P) at unusually early time scales ($t < 60$ s). This initial plateau value of ϵ^2 was eventually disrupted by a sudden jump to a slightly larger plateau value, which corresponds to the moment where the growing volume of water can no longer be confined entirely within the hydrophilic stripe (i.e. the contact angle of the water at the borders of the stripe reaches its advancing value). It can be observed that the water overflow from each stripe is always managed in the form of a single droplet spontaneously bulging out, in order to minimize the system's surface energy [174, 183].

While the exact location along a stripe where a droplet bulges out seems be random for the first stripe where overflow occurs, a fascinating chain reaction follows where adjacent stripes proceed to bulge out droplets at the exact same location (Fig. 3c, d). In other words, the formation of a bulge in one stripe causes the preferential condensation of water on adjacent stripes in the region closest to that bulge, resulting in the overflow and formation of a bulge at the same axial location. It was observed that this chain reaction occurs more rapidly for denser patterns due to the closer proximity of the bulging droplet to the neighboring stripes; for example, in Fig. 3 a chain of seven droplets forms approximately 4 times faster for HS4P compared to HS8P. To our knowledge, this is the first time that a chain reaction of aligned droplets bulging out from adjacent stripes of water has been observed during condensation. It is an open question as to what is driving this phenomenon. The bulge configuration exhibits a smaller mean curvature compared to a non-bulged stripe of water [183]; therefore one possibility is that the bulged droplet exhibits minimal interfacial resistance and capillary resistance for condensation heat transfer [149], which serves to maximize the flow and concentration of water vapor in the region of the bulge. Note that while the conduction resistance would be larger in the bulged droplet compared to a stripe of water, this resistance is expected to be negligible for the micrometric condensate observed here [184]. Another possibility is that inertial effects from the initial bulging of a droplet could induce a net flow in the vapor field toward the neighboring stripes. Assume that a bulging droplet exhibits a capillary-inertial velocity of $v_i \sim \sqrt{\gamma/\rho_l r}$ during its expansion, where ρ_l is the density of liquid water and $r \sim 10\,\mu$m is the radius of the bulge protruding from the stripe of water.

The Reynolds number of the air then scales as $\text{Re} \sim (\rho_g/\mu_g)\sqrt{\gamma r/\rho_l} \sim 1$ (where ρ_g and μ_g are the density and viscosity of the air/vapor surrounding the water), which might be sufficient to induce a vapor flow toward the neighboring stripes.
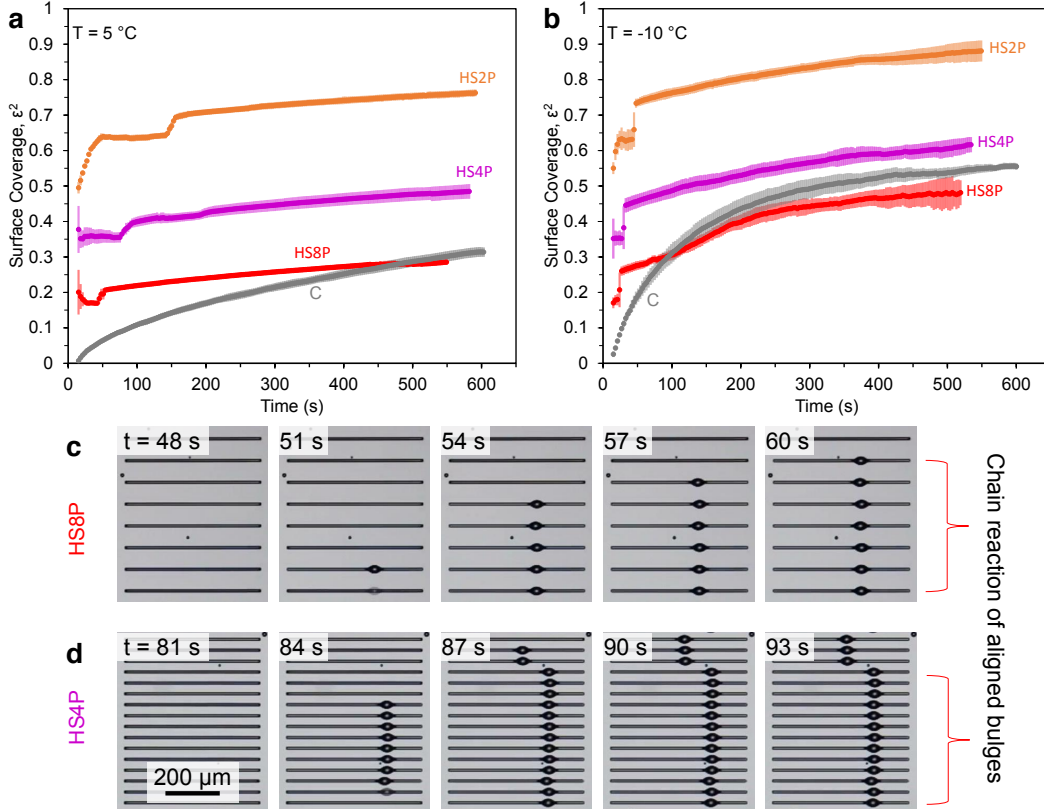
FIGURE 6.3: Growth of condensation on patterns of hydrophilic stripes of varying pitch (HS2P, HS4P, and HS8P) compared to a uniformly hydrophobic control surface (C). (**a,b**) Surface coverage versus time for supersaturations of $S = 1.2$ ($T_s = 5\,^\circ\mathrm{C}$) or $S = 3.9$ ($T_s = -10\,^\circ\mathrm{C}$), respectively. (**c,d**) When a hydrophilic stripe overflows with water and bulges out a single droplet, neighboring stripes proceed to bulge out droplets at the same axial location in a chain reaction. Images depict chain reactions occurring for HS4P or HS8P at $S = 1.2$. Since more dilute patterns of stripes are able to collect water at a faster rate than denser patterns, it follows that droplet bulging occurs first for C8P, followed by C4P and finally C2P.

To date, very little is known regarding the ability of patterned substrates to spatially manage condensate over a period of time. In addition to measuring $< D >$ and ϵ^2, we therefore introduce two additional metrics to better quantify the spatial control of condensation on wettability patterns. A dimensionless measure of the quality of spatial control, $Q^*(t)$, is given by:

$$Q^*(t) = \frac{N_d(t)}{N_f} \tag{6.7}$$

where $N_d(t)$ is the number of condensed droplets and N_f is the number of hydrophilic features within the same surface area. For a low supersaturation ($S = 1.2$), initially

59
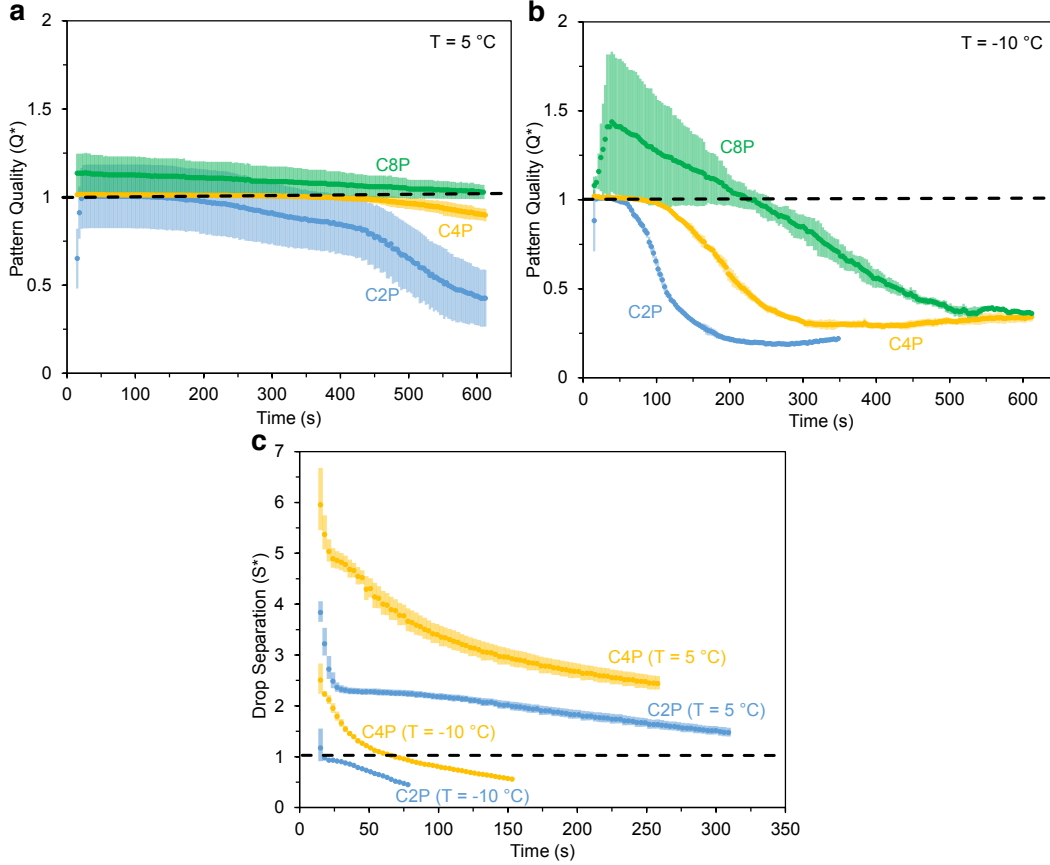
FIGURE 6.4: Characterizing the spatial control of patterned condensation. (**a,b**) The quality, $Q^*(t)$, represents the ratio of condensed droplets to the number of hydrophilic features (Eq. 6.7). (**c**) The drop separation coefficient, $S^*(t)$, relates the size of condensate to the inter-droplet separation (Eq. 6.8); for times where $S^* > 1$, inter-droplet frost growth is expected to be suppressed.

$Q^* \approx 1$ for C2P and C4P, followed by $Q^* < 1$ upon the onset of coalescence (Fig. 4a). An advantage of the C4P array is that coalescence occurred at a later time compared to C2P, such that $Q^* \approx 1$ for approximately 500 s rather than only 100 s. Conversely, $Q^* > 1$ at early times for C8P, due to the nucleation of droplets on the hydrophobic regions between the dilute hydrophilic features. Results were qualitatively similar for $S = 3.9$, except that C4P exhibited an extremely small degree of condensation on hydrophobic regions ($Q^* \approx 1.02$ at early times) and the reduced quality of C8P was more exaggerated (up to $Q^* \approx 1.44$ compared to $Q^* \approx 1.14$ for $S = 1.2$).

Finally, when spatially controlling condensation for the express purpose of tuning inter-droplet frost growth, the most relevant metric is the separation between the droplets relative to the size of the droplets. Previously, we have demonstrated that a dimensionless droplet separation coefficient, $S^* \sim L/D$, predicts with high accuracy whether a frozen droplet is able to grow a frost bridge to a neighboring su-

percooled liquid droplet of initial diameter D and distance L from the frozen droplet [6]. This scaling model is based off the observation that an ice bridge requires a two-dimensional area of roughly $A_b \sim DL$ to connect to a neighboring supercooled droplet with an initial (prior to harvesting) area of $A_b \sim D^2$. Therefore, when $S^* > 1$, the liquid droplet being harvested will completely evaporate before the ice bridge accumulates enough mass to connect, resulting in the stoppage of localized in-plane frost growth [6]. For the random growth of dropwise condensate on a homogeneous surface, measuring S^* requires either tedious manual measurements of D and L for every droplet [6] or a complex image analysis program. For condensation spatially controlled by chemical micropatterns, on the other hand, the inter-droplet distance can now be easily calculated:

$$S^*(t) = \frac{b - (<D(t)>/2)}{<D(t)>} \tag{6.8}$$

which applies to every droplet within the pattern, provided that $Q^*(t) \approx 1$. Note that L is signified by $(b - (<D(t)>/2))$ because the longest possible ice bridge is when the liquid droplet has almost entirely evaporated, which adds the radius of the droplet to the total length of the connecting bridge. It can be observed in Fig. 1 that D and L are approximately equal for all droplets at a given time for the C2P and C4P patterns (prior to coalescence events), with the minor exception of droplets at the edge of the pattern which have fewer hydrophilic neighbors and are therefore slightly larger. By plotting $S^*(t)$ vs. t, it was observed that P and S both played significant roles regarding the length of time where $S^*(t) > 1$ (Fig. 4c). Indeed, the duration of $S^*(t) > 1$ was extended by over an order of magnitude for $S = 1.2$ compared to $S = 3.9$, and by several times for C4P compared to C2P at the same supersaturation. These findings have important ramifications for the subsequent growth of frost over supercooled patterns of condensation.

6.3.4 Observation of Non-Local Frost Growth

The growth of frost was characterized at $T_s = -10\,°C$ for chemical patterns of pitch $P = 2$ or $P = 4$, such that the quality of spatial control for the supercooled condensate was $Q^* \approx 1$. When the atmospheric conditions were kept identical to the previous experiments characterizing condensation ($T_\infty = 21\,°C$ and $H = 40\,\%$), inter-droplet frost growth could not be measured repeatably due to an unexpected second mechanism of frost growth. In addition to the expected ice bridges that were grown locally from frozen droplets to neighboring liquid droplets, a surprising long-range freezing mechanism was consistently observed where a piece of ice suddenly appeared on a region of the surface far away from any pre-existing sources of ice (Fig. 5). Once these ice crystals suddenly appeared on the surface, they were able to grow in size by harvesting water from nearby liquid droplets until connecting to them, in a manner henceforth identical to locally grown ice bridges. We hypothesize that these non-local appearances of ice crystals are deposits ejected from the explosive freezing of

supercooled droplets somewhere on the surface. This hypothesis of "ice shrapnel" is deduced from the following observations: (1) the region of the surface where the ice crystal suddenly appeared was often completely dry just a moment prior, ruling out the possibility of supercooled water nucleating into ice; (2) these non-local ice crystals were exclusively and abundantly observed to appear in the seconds after the freezing of a droplet(s) elsewhere on the surface, and never occurred prior to the first freezing event even over a span of several minutes; (3) the explosive freezing of supercooled water droplets has been previously observed and identified as a mechanism for increasing the amount of ice particles in clouds [116, 185]. Note that this "ice shrapnel" effect, which was observed on a highly conductive substrate ($k_{Si} \approx 150$ W/m·K) and ejects ice far away from the mother droplet, would appear to be fundamentally different from the recently reported "frost halo" effect, which was exclusive to a highly insulating surface ($k_{PMMA} \approx 0.19$ W/m·K) and involves the localized evaporation and re-freezing of water vapor around the mother droplet [4].

For the present study, it was found that the rate of frost growth was inconsistent when the effects of localized inter-droplet ice bridging were combined with the non-local ice shrapnel effect (Supplementary Fig. S8). Interestingly, it was observed that when the same experiments were repeated in a different laboratory under less humid conditions ($T_\infty = 24.0 \pm 0.9$ °C, $H = 26 \pm 2\%$, $S = 3.1$), the ice shrapnel effect never occurred. It is likely (but not certain) that the decrease in humidity was directly responsible for the disappearance of the ice shrapnel, as this is in agreement with a previous report that shattering did not occur for droplets freezing at sufficiently cold (and therefore less humid) air temperatures [185]. Therefore, all experiments in the proceeding sections were performed at these new environmental conditions, such that localized inter-droplet ice-bridging was isolated as the sole mechanism of in-plane frost growth.

6.3.5   Tuning Inter-Droplet Frost Growth

The separation between droplets (S^*) exhibits a strong dependence upon both the pitch of the chemical pattern and the time allowed for condensation to grow (Fig. 4c); therefore, it is now clear that the onset of freezing must be temporally controlled to properly tune the rate of inter-droplet frost growth. To control both the time and location at which freezing first occurred on the surface, a large hydrophilic rectangle was patterned along the edge of each silicon chip, such that a thin film of water could be deposited onto the surface that bordered one end of the chemical arrays. Regardless of the pitch or shape of the chemical arrays, the edge-to-edge separation between the water film and the first row of patterned features was $10\,\mu$m. Once the edge of the wafer was primed with this thin film of water, the surface was cooled beneath the dew point to a subfreezing temperature in order to grow the patterned condensation as usual. At the desired time, the supercooled film of water was frozen by gently touching a small piece of ice to the edge of the wafer, and frost proceeded to propagate across the arrays of chemical patterns via inter-droplet ice bridges (Fig. 6,
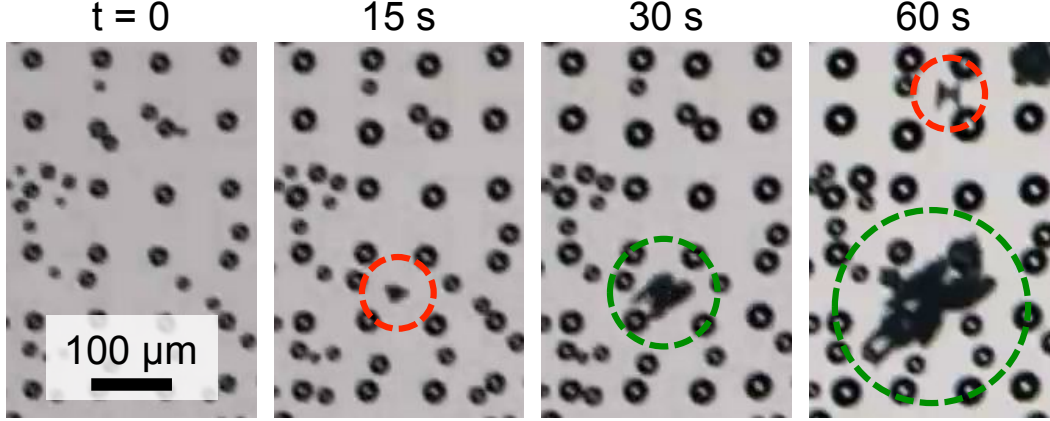
FIGURE 6.5: Observation of the ice shrapnel effect. Supercooled condensation growing on T8P (1st frame) is disrupted by ice shrapnel thrown from a freezing droplet (off screen) onto a dry region of the surface (2nd frame). The ice shrapnel proceeds to freeze neighboring droplets via inter-droplet ice bridging (3rd frame) and subsequent freezing events eject more ice shrapnel onto the surface (4th frame). Time zero corresponds to reaching a steady-state temperature of $T_s = -10\,^{\circ}\mathrm{C}$ ($S = 3.9$), red circles indicate the initial appearance of ice shrapnel, and green circles denote the subsequent inter-droplet growth.

Supplementary Figs. S9−S11). In this manner, the patterned arrays of supercooled condensation now resemble race tracks, where the propagation speed of frost growth can be characterized as a function of the pattern geometry and the time elapsed before the onset of freezing.

The average speed of inter-droplet frost growth across supercooled condensation patterns was measured for arrays of circles (C2P/C4P), triangles (T2P/T4P), and stripes running parallel (HS2P/HS4P) or perpendicular (VS2P/VS4P) to the frozen water film (Fig. 7). In each trial, the deposited film of water adjacent to the arrays was frozen either 1, 3, or 5 min after the surface reached a steady-state temperature of $T_s = -10\,^{\circ}\mathrm{C}$. The velocity of the inter-droplet freezing front is expressed as $v = \sqrt{A}/t$, where A is the total area enclosing a particular array and t is the time required for frost to completely grow over A. Depending upon the shape and pitch of the array and the time of initial freezing, the value of v could vary by at least an order of magnitude. As expected, frost was able to grow faster when $P = 2$ compared to $P = 4$, due to the closer proximity of the nucleation sites greatly decreasing the value of S^* (cf. Fig. 4c). The values of v increased with later times of freezing onset for arrays of circles or triangles, and the extent of the difference in v between $P = 2$ compared to $P = 4$ also became amplified at later freezing times. In contrast, the freezing time was not nearly as important for the striped patterns, as the surface coverage of the stripes reaches a plateau value at extremely early time scales and is not as sensitive to time (cf. Fig. 3). Furthermore, the average speed of the frost growth was much more inconsistent for the HS patterns, as it could vary widely
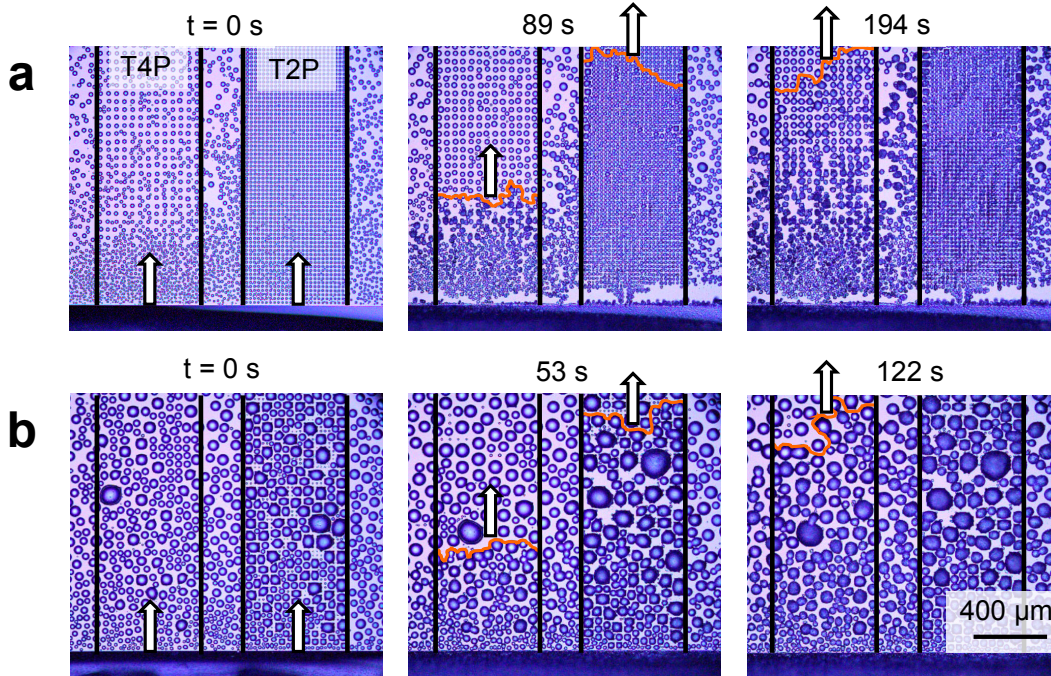
FIGURE 6.6: Inter-droplet frost growth across patterns of supercooled condensation (T4P on left and T2P on right). Freezing was initiated **(a)** 1 min or **(b)** 5 min after reaching a steady-state temperature of $T_s = -10\,^{\circ}\mathrm{C}$ ($S = 2.7$) by touching a piece of ice to a rectangular film of water (bottom of the images) bordering the droplet arrays. In each figure, the 1st frame shows the onset of freezing (called time zero), while the 2nd and 3rd frames represent the times where the inter-droplet frost grew to the top of the field-of-view in the T2P and T4P arrays, respectively. Measured velocities of frost growth were **(a)** $v_{T4P} = 4.38\,\mu\mathrm{m/s}$ and $v_{T2P} = 10.01\,\mu\mathrm{m/s}$; **(b)** $v_{T4P} = 6.05\,\mu\mathrm{m/s}$ and $v_{T2P} = 16.73\,\mu\mathrm{m/s}$.

depending upon how many of the bulged droplets were axially aligned to minimize the spacing between each body of water. Note that the geometry of the chemical patterns not only controls the velocity of frost growth, but also the macroscopic shape of the ice. This was characterized in terms of the surface coverage of the frost, which is defined as the fraction of the projected area that contains ice. Recall that the surface coverage of supercooled condensation at any given time was smaller for $P = 4$ arrays compared to $P = 2$; since in-plane frost growth is essentially an inter-droplet phenomenon, it therefore follows that the surface coverage of the frost is also lower for $P = 4$. In short, both the speed and surface coverage of in-plane frost growth is dependent upon S^*, which in turn can be tuned by chemical patterns and controlling the time of initial freezing.
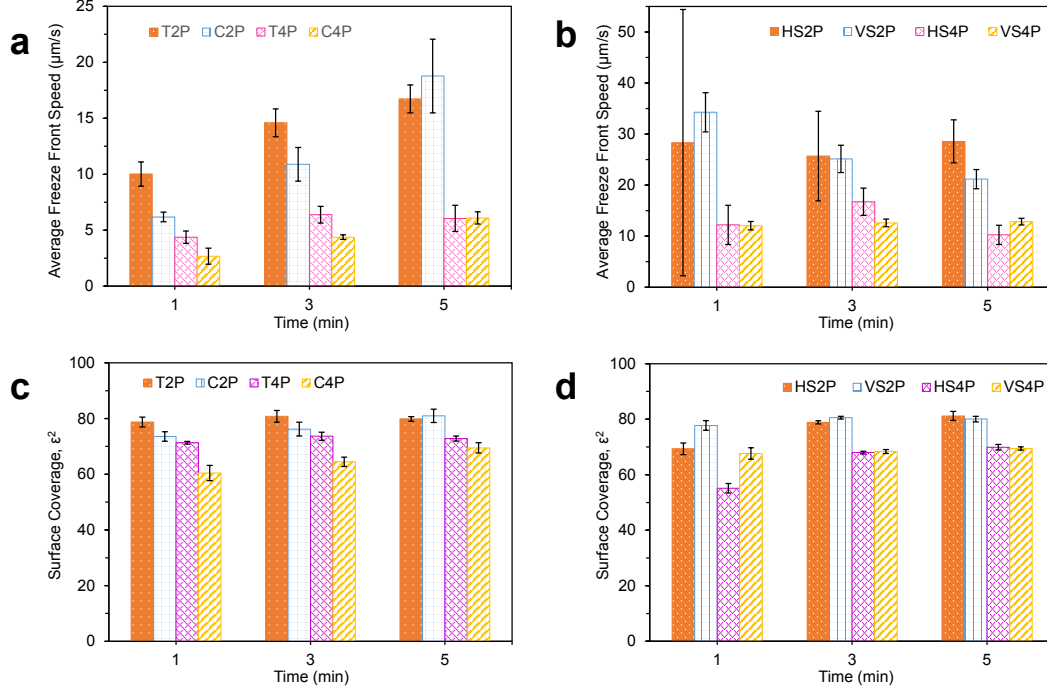
FIGURE 6.7: Propagation velocity (v) and surface coverage (ϵ^2) of frost growing over various patterns of supercooled condensation at $T_s = -10\,°C$ and $S = 3.1$. (**a, b**) The average velocity of frost growth could be tuned by the geometry and spacing of the patterns and also depended upon the time of the initial freezing event. (**c, d**) After the pattern of condensation visible in the field-of-view had completely frozen over, the surface coverage of frost was measured; ϵ^2 was approximately 0.2 times lower for the $P = 4$ patterns compared to the $P = 2$ patterns.

6.3.6   Halting Inter-Droplet Ice Bridging

In the previous experiments, where freezing was initiated either 1, 3, or 5 min after cooling to $T_s = -10\,°C$, the frost was always able to grow across the surface. This is because as the surface is cooled to $T_s = -10\,°C$, $S^* > 1$ is only true for roughly 20 s of condensation growth for $P = 2$ patterns and 60 s for $P = 4$, including the 30 s required for the cooling transient (cf. Fig. 4c). Therefore, to completely stop inter-droplet frost growth via ice bridging, the onset of freezing needs to occur as early as possible, such that $S^* > 1$ and water droplets will completely evaporate before the ice bridges can connect. To demonstrate that inter-droplet ice bridging can be completely halted, a surface exhibiting VS2P and VS4P patterns was frozen immediately after reaching $T_s = -5\,°C$ and then cooled all the way down to $T_s = -12.5\,°C$. The water contained in the stripes proceeded to evaporate and recede away from the ice, creating a dry zone that reached a maximal value of approximately $L = 180\,\mu m$ that was stable for over 5 min (Fig. 8). This would appear to be the first report of halting inter-droplet ice bridging between ice and its neighboring supercooled condensate. While one

recent report did observe the inability of ice to connect to supercooled condensate on a hydrophobic surface [57], the ice was isolated at an edge of the substrate at least $80\,\mu$m away from the nearest condensate and the dry zone was only monitored for $2\,$min. Here, the initial separation between the ice and condensate was a mere $10\,\mu$m, and the freezing of the ice served to increase this gap by a factor of 18 for at least $5\,$min.

While successful in preventing the ice from bridging to neighboring condensate, a single dry zone does have two long-term limitations. Firstly, far from the dry zone, the supercooled condensation is still free to grow, and will eventually freeze and grow ice bridges across the surface. This was evident in Fig. 8, where the dry zone itself was stable but frost was able to invade across the droplet arrays from elsewhere on the surface. Secondly, while the condensation growing beyond the edge of the dry zone does exhibit a net influx of vapor, these droplets still exhibit a partial outflux of vapor that migrates across the dry zone and is harvested by the ice. It is for this reason that the film of ice continues to grow in-plane over time even after the dry zone has formed, as can be observed in the graph in Fig. 8. It should be emphasized that the in-plane growth of the isolated ice patch is of order $v \sim 0.1\,\mu$m/s (Fig. 8), two orders of magnitude slower than $v \sim 10\,\mu$m/s observed for traditional frost growth via inter-droplet ice bridging (Fig. 7a,b). Furthermore, the advancement of the ice serves to translate the dry zone upward, resulting in the continued evaporation and receding of the nearest water region. Sometimes, the water is not able to recede quite as quickly as the ice advances, as evidenced from the very slowly decaying dry zone length (L) plotted in Fig. 8. The slower receding of the water is attributed to two factors: contact angle hysteresis causing a stick-slide behavior, and the evaporating water being replenished by more water further up the patterns in the case of the stripes. Finally, it is interesting to note that the shape of the advancing ice front depends upon the geometry of the water being harvested: a fingering shape results for ice growing toward discontinuous patterns (Supplementary Fig. S12), while the ice front is more uniform when growing toward horizontal stripes of water (Supplementary Fig. S13).

The length of the dry zone about the ice, δ_{IG}, can be theoretically estimated using the same flux balance approach used for calculating the condensation dry zones (see 'Spatial Control of Condensation' section). The pressure gradients are driven by $P_\infty > P_s > P_{s,i}$, where P_s and $P_{s,i}$ are the saturation pressures of water and ice, respectively. The perimeter of the dry zone corresponds to the point where the net mass flux condensing into a liquid droplet from the ambient air is equal to the net mass flux evaporating from the droplet towards the ice. The condensed droplets bordering the dry zone can be approximated as an equivalent film of water of height h [9], where $h \sim r$, r being the mean droplet radius (see schematic in Fig. 8). This film has at its top a pressure P_s corresponding to the saturation pressure of water at T_s. Let us take a thin strip of the film of length L along the perimeter, height h and width r. Then the mass flow rate of vapor condensing onto the droplets due to the out-of-plane pressure gradient scales as $\dot{m}_c^w \sim (rL)J_c^w \propto (rL)\left(P_\infty - P_s\right)/\zeta$.
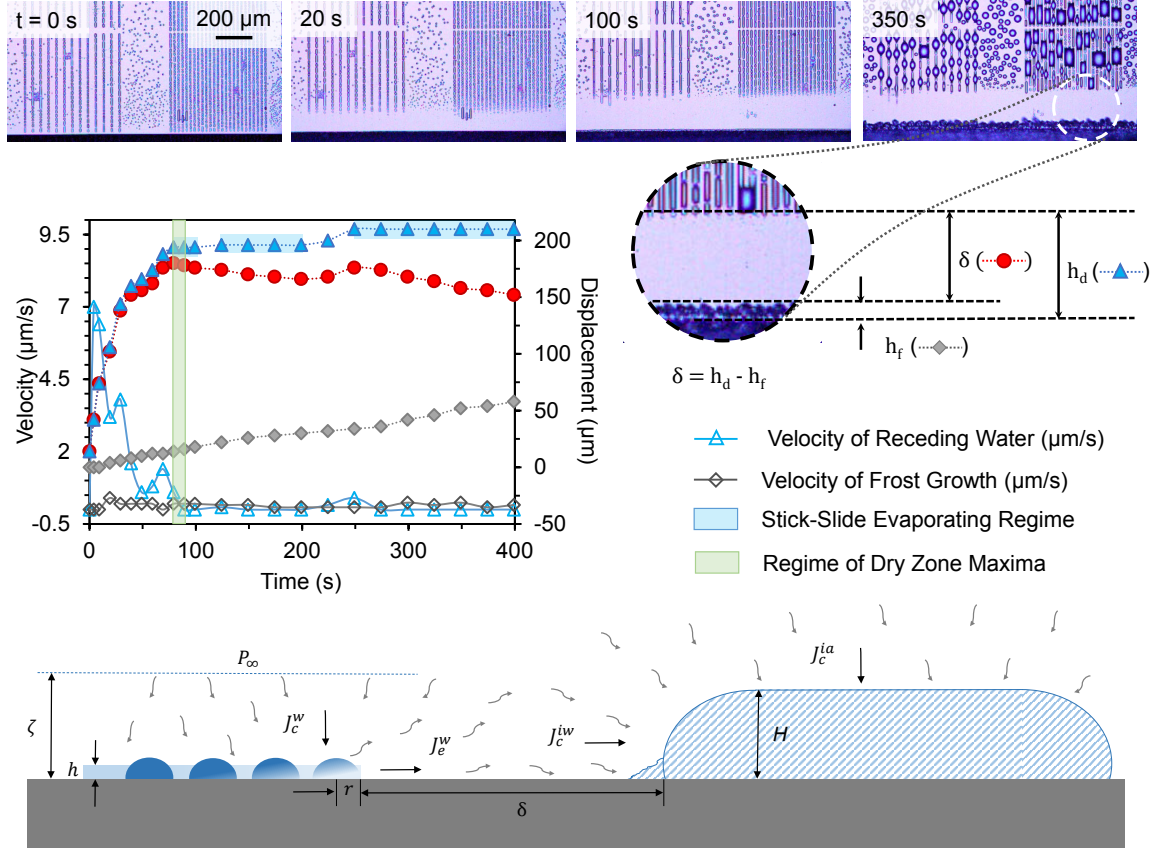
FIGURE 6.8: Demonstration of halted inter-droplet frost growth. By freezing the film of water (visible at the bottom of the pictures) immediately after cooling down to $T_s = -5\,°C$, the size of the water droplets was sufficiently small to prevent the success of ice bridging. Even when the substrate was subsequently cooled to $T_s = -12.5\,°C$, the surface area adjacent to the frozen film remained dry for over 5 min The dry zone would have lasted even longer, but frost eventually invaded the surface from the side, due to frost propagation from an uncontrolled region of the surface. The schematic illustrates the dry zone between ice and the condensate; the border of the dry zone corresponds to the point where the condensation and evaporation rates of the supercooled droplets are perfectly balanced.

The in-plane mass flow rate of vapor evaporating out towards the ice scales as $\dot{m}_e^w \sim (hL)J_e^w \propto (hL)\,(P_s - P_{s,i})\,/\delta$. Equating the condensation and evaporation rates at the border of the dry zone:

$$\frac{\delta_{IG}}{\zeta} \sim \frac{P_s - P_{s,i}}{P_\infty - P_s}.\qquad(6.9)$$

For the experimental conditions $T_s = -12.5\,°C$, $T_\infty = 24\,°C$, and $H = 26\%$, the corresponding vapor pressures are $P_\infty = 776\,Pa$, $P_s = 235\,Pa$ and $P_{s,i} = 208\,Pa$. Using Eq. 6.9, the experimentally observed dry zone length of $\delta_{IG} \approx 180\,\mu m$ corresponds to a

concentration boundary layer thickness of $\zeta \approx 3.7\,\text{mm}$. This agrees with a theoretical estimation of ζ using Eq. 6.5, where $\zeta \sim 1\,\text{mm}$ is obtained.

6.4 Discussion

Several recent reports on delaying frost growth with superhydrophobic surfaces have focused on maximizing the elapsed time before any freezing events occur within the population of supercooled condensation [54–56]. Our observations from the present study suggest rather counterintuitively that the exact opposite approach is preferable: by intentionally triggering an extremely early freezing event on the surface, the spacing between droplets is maximized to slow or even halt the inter-droplet growth of frost. Indeed, far from being undesirable, early freezing events can create dry zones, where all of the adjacent water droplets are harvested by the ice due to the localized gradient in vapor pressures (Fig. 8).

The present study characterized condensation and frost formation with the ambient environment at room temperature and fixed humidity, in contrast to natural systems where the air and surface temperatures are similar and the humidity can fluctuate widely. A recent study utilized an environmental chamber to chill the ambient air and widely vary the humidity, and confirmed that inter-droplet ice-bridging remains the primary driver of in-plane frost growth over this wider parameter space [120]. Cooler and/or drier ambient conditions would correspond to a decreased supersaturation (S), which would likely increase the critical pitch of the hydrophilic patterns to maintain spatial control and magnify the effects of the pressure gradient between water and ice responsible for the dry zones. Therefore, the highly supersaturated conditions used here are actually somewhat extreme; it should be easier to pattern condensation and/or prevent inter-droplet ice bridging in a more natural environment. It should also be emphasized that silane monolayers, while ideal for fundamental studies, are prone to degradation under long-term condensation or frosting conditions. More durable hydrophobic coatings, such as grafted polymers [186], graphene [158], or intrinsically hydrophobic materials would therefore seem more appropriate for practical applications. The surfaces used for the present study were thermally conductive and extremely smooth; it would be interesting for future studies to characterize how the spatial control of condensation and frost could be modified by practical materials that exhibit varying degrees of roughness and thermophysical properties.

In the present work, we triggered an early freezing event to locally dry out condensate and create a single dry zone on the chilled surface. While stable for several minutes at the very least, the long-term durability of the dry zone is doubtful due to the continued growth of water and ice far away from the dry zone. We suggest that a possible solution to this problem is triggering multiple freezing events simultaneously at an early time scale, for example creating an array of thin stripes of ice, such that multiple dry zones are created that overlap to permanently dry all of the liquid water

away from the regions between the ice arrays. In other words, rather than patterning the supercooled condensation and triggering an isolated freezing event, it would now appear to be advantageous to pattern the freezing water itself!

In conclusion, the spatial control of liquid condensation on chemical patterns, as well as the formation of a dry zone between ice and supercooled water, are both driven by a fascinating competition between in-plane and out-of-plane gradients in vapor pressure. Smooth chemical micropatterns can spatially control both the nucleation and growth of condensation even at very large supersaturations, provided that the distance between hydrophilic features is not too large. Compared to a uniform hydrophobic surface, condensation on a chemically patterned surface exhibited smaller average diameters and more homogeneous droplet volumes and inter-droplet separations. Therefore chemically patterned surfaces serve to maximize the spacing between condensate, such that the in-plane growth of frost via inter-droplet ice bridging can be delayed or even completely halted. Since the separation between droplets decreases with increasing duration of condensation, it was demonstrated that intentionally triggering an early freezing event on the surface is also crucial for halting ice bridging. Indeed, extremely early freezing events were shown to halt inter-droplet frost growth even on the non-patterned regions of the surface. Therefore, the inter-droplet growth of frost across a surface can be minimized or even stopped by spatially and/or temporally maximizing the separation between supercooled condensate upon the onset of freezing.

7
Dry Zones

"Why don't you all f–fade away...? "

− The Who

7.1 Introduction

In the 1480-s, da Vinci invented the first hygrometer using cellulose fibers to attract moisture from the atmosphere [187]. Five hundred years later, Williams and Blanc showed that a hygroscopic droplet can create a macroscopic dry zone around itself owing to its depressed vapor pressure [146]. What remains unresolved still is whether these regions of inhibited condensation around hygroscopic droplets are regions of inhibited nucleation [8, 10, 80, 188] or regions of inhibited growth [9, 63, 141]. We try to investigate this by considering frozen water droplets as our hygroscopic agents, placed on a subcooled hydrophobic substrate. Following extensive experiments for different ice droplet sizes, supersaturation varying two orders of magnitude, and substrate temperatures varying from $-30°C \leq T_w < 0°C$, we discuss how nucleation dry zones compete with flux-governed dry zones. Finally we show how all the dry zones collapse on a new scaling law, reminiscent of that proposed by Guadarrama-Cetina et al. [9].

Hygroscopic substances preferentially absorb (or adsorb) water molecules from the surrounding humid air. In cases where the ambient humidity or surface temperature fluctuates, the resulting sorption/desorption cycles enable seed-dispersal mechanisms for pine cones and wheat plants [189, 190] and enable engineered systems such as heat pumps [191], thermal batteries [192], and hygromorphic actuators and engines [193–196]. For conditions where a surface is beneath the dew point but the accumulation of dew or frost is undesirable, hygroscopic chemicals such as glycols, salts, and silica gels have been used as sacrificial materials to render a surface dry [9, 10, 80, 146, 197]. It is therefore surprising that the physics governing the extent of a dry zone about a hygroscopic agent remain somewhat unclear to this day.

Our current lack of understanding is partly due to the inability to obtain steady-state dry zones, as traditional hygroscopic materials necessarily become diluted over time which leads to the decay and collapse of dry zones [9, 10, 80, 147, 197]. A further complication is the possibility of two competing mechanisms for dry zone formation – inhibition of nucleation versus inhibition of growth of condensate. The critical length of a region of inhibited nucleation corresponds to the distance from the hygroscopic droplet where the vapor concentration becomes high enough to overcome the nucleation energy barrier [8, 10, 80, 147, 188, 197]. As such, this kind of dry zone would be a function of the critical Gibbs free energy $\Delta \tilde{g}$ required to nucleate, alongside other physical parameters such as the substrate temperature T_w, frozen droplet size R, and ambient concentration c_∞ [80, 141]. Here, we will call this type of dry zone a nucleation dry zone, δ_N, for short. Historically, the formation of dry zones was solely attributed to the inhibition of nucleation. However, in 2015 Guadarrama-Cetina et al. proposed a second mechanism of inhibited growth [9]. For a region of inhibited growth, the dry zone length corresponds to the critical distance where a droplet's out-of-plane condensation flux balances its in-plane evaporative flux toward the hygroscopic droplet. We will call this second type of dry zone a flux dry zone, denoted by a critical length δ_F. To date, no reports have directly

71

compared models of δ_N and δ_F against experimental dry zones obtained over a wide parameter space. Thus, which physical mechanism wins the duel of the dry zones remains unknown.

Here, we obtain steady-state dry zones around ice droplets and reveal the underlying physics by comparing all results to refined models of nucleation and flux dry zones. Our ability to obtain stable dry zones was enabled by the unique choice of ice as the hygroscopic material [14, 63], whose saturation vapor pressure remains constant as it harvests water vapor and is therefore always lower than that of liquid water at the same temperature [20]. We placed a $10\,\mu\text{L}$ water droplet on hydrophobic silicon and subsequently froze it using the underlying Peltier stage. The humidity chamber enclosing the system was made sufficiently dry to prevent any condensate or frost from forming on the surface. Subsequently, the surface temperature was decreased or the ambient humidity was increased to promote the formation of supercooled condensation on the surface. The steady-state length of the annular dry zone, δ_{Cr}, that formed between the ice droplet and the condensate was measured under a microscope (Figure 7.1a).

7.2 Results and discussion

7.2.1 Experimental Results

A nuance not discussed in previous works is the path dependency of dry zone formation (see Figure S1 in Supporting Information). If the dry zone forms by evaporating pre-existing liquid condensate, then δ_{Cr} always corresponds to δ_F. In other words, when condensate has already nucleated prior to the steady-state test conditions, evaporating these droplets to create the flux dry zone is the only option. However, by freezing the deposited water droplet in a sufficiently dry environment where the surface is above the dew point, we can suppress any transient condensation effects including the recalesence-induced halo [4]. We can now increase c_∞ (or decrease T_w) to allow condensate to form, now the dry zone can correspond to either the nucleation dry zone or the flux dry zone, whichever is larger. Therefore, only by doing experiments in our controlled humidity chamber where $\delta(t=0) \to \infty$ shrinks down to δ_{Cr} can we rigorously compare the dueling dry zones over a wide parameter space. The latter protocol requires the careful evaporation of any frost halos, which are condensate droplets nucleated by a recalescence-induced local supersaturation in the vicinity of the freezing droplet

The steady-state value of δ_{Cr} was measured for surface temperatures ranging from $T_w = -30\,°\text{C}$ to $-2.5\,°\text{C}$ and ambient vapor concentrations ranging from $c_\infty = 5.6 \times 10^{-4}$ to $0.7 \times 10^{-2}\,\text{kg/m}^3$ (Figure 7.2a, b). For a given humidity, the value of δ_{Cr} peaked around $T_w = -12.5\,°\text{C}$, as the difference in saturation vapor pressures between water and ice is thermodynamically maximal at this temperature [20]. The magnitude of δ_{Cr} increased by an order of magnitude with decreasing ambient humidity. This is intuitive, as reducing c_∞ makes it more difficult to overcome the
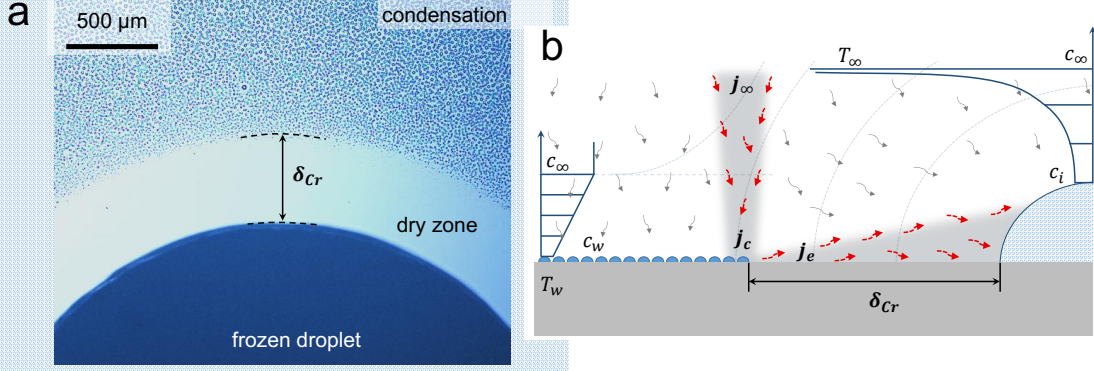
FIGURE 7.1: Dry Zone around a Frozen Water Droplet. a) A micrograph of a frozen water droplet evaporating surrounding droplets to create a stable dry zone of length $\delta_{Cr} = 507\,\mu$m, even though the surface temperature ($T_w = -10°$C) is 16 degrees beneath the dew point. The mechanism is the depressed vapor pressure over ice relative to supercooled water at the same temperature. The frozen droplet has a contact line radius of $R = 1.7\,$mm, while the liquid condensate beyond the dry zone length are of the order $a \sim 1 - 10\,\mu$m. b) Schematic of the vapor flow around the frozen droplet. Far from the frozen droplet, amidst the population of supercooled condensate, the concentration profile is linear in the vertical direction [8]. The droplet pattern in such a case can be approximated as a homogeneous water film with an average thickness h. It follows $c \sim c_w + (c_\infty - c_w)z/\zeta$, where ζ is the concentration boundary layer thickness. Close to the frozen droplet, the concentration profile has a hyperbolic variation as $c \sim c_\infty - (c_\infty - c_i)R/r$.

nucleation energy barrier close to the ice (increasing δ_N) while simultaneously reducing the out-of-plane condensation that is competing with in-plane evaporation (increasing δ_F).

In a separate set of experiments, we varied the volume of the ice droplet from 1–100 μL and found that the dry zone increases with the size of the hygroscopic droplet (Figure 7.2c,d). Unlike the experiments where humidity was varied, these experiments were performed without a controlled humidity chamber. Instead, the droplet was frozen in a dry freezer and then quickly transferred to a nearby Peltier stage in an ambient environment ($c_\infty = 1.2 \times 10^{-2}\,$kg/m^3). The brief exposure of the surface to room temperature conditions before getting cooled by the Peltier ensured that condensation nucleated everywhere on the surface before a steady-state dry zone could subsequently form. This removes the possibility of a nucleation dry zone, which allows us to isolate the physics of a flux dry zone and compare to the aforementioned case where both nucleation and flux dry zones are possible (Figure 7.2a, b).
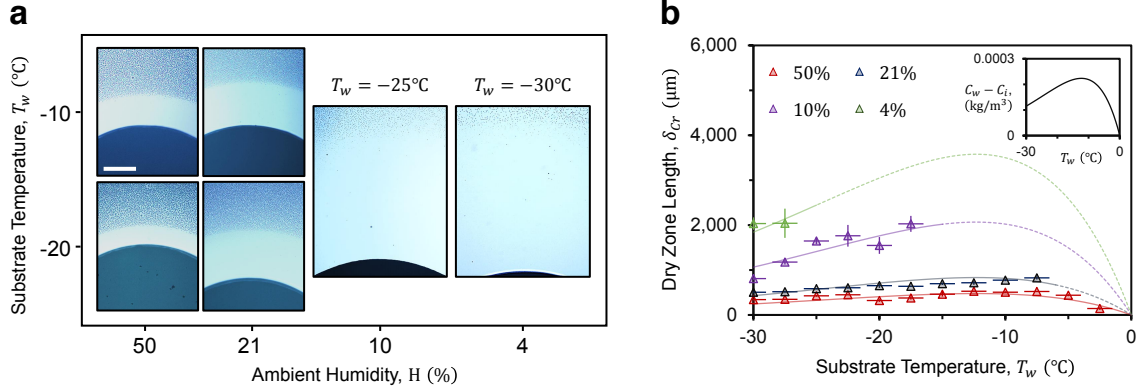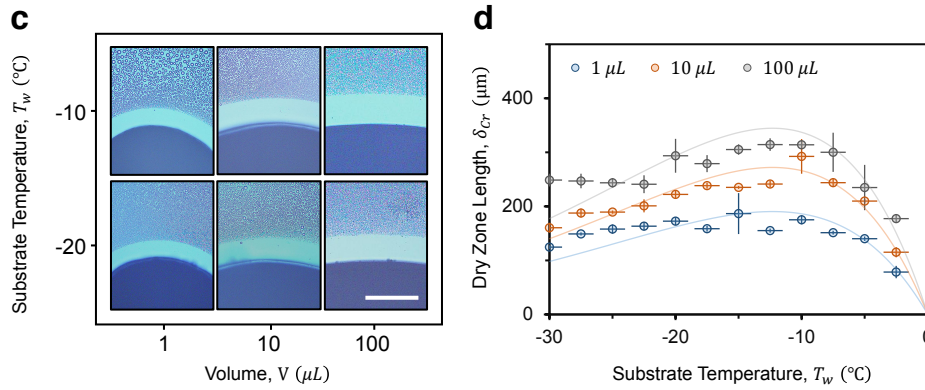
FIGURE 7.2: Dry Zone Variation with Temperature, Humidity and Droplet Size. a,b) Humidity Chamber experiments with a fixed frozen droplet volume $10\,\mu$L and varying humidity. Experimental micrographs show that the dry zone length increases with decreasing humidity. When plotted against the substrate temperature, the $\delta-T$ curves for different humidities qualitatively trace out the variation in $(c_w - c_i)$ with temperature (inset), where c_w and c_i are the saturation vapor concentrations over water and ice respectively. Note that there are no data points corresponding to 4, 10 and 21% humidities above a critical temperature corresponding to the nucleation threshold. c,d) Ambient Experiments where the humidity was fixed, but the size of the frozen droplet was varied. Experimental images show that the dry zone length increases with droplet size. The scale bars in a) and c) represent $500\,\mu$m, while the curved lines in b) and d) are fits to Equation 7.5 indicating the dominance of flux dry zones.

7.2.2 Nucleation Dry Zone Model

To capture the physics underlying the experimental dry zones, we used a quasi-steady diffusion driven model to estimate the nucleation dry zone (δ_N). Extending radially from the surface of the frozen droplet, the concentration profile exhibits a hyperbolic profile:

$$c = c_\infty - (c_\infty - c_i)R/r, \tag{7.1}$$

where r is the radial coordinate and $r = R$ at the droplet interface. Let c_N represent the critical vapor concentration required to nucleate a new embryo, such that $(r - R) = \delta_N$ when $c = c_N$. Using the definition of the supersaturation degree, $SSD = (c_N - c_w)/c_w$, we can now rewrite the above equation as:

$$\delta_N \sim \frac{R\left((SSD + 1)(c_w - c_i)\right)}{\left(c_\infty - (SSD + 1)c_w\right)}. \tag{7.2}$$

Noting that the saturation concentrations c_w and c_i are purely functions of the surface temperature, we see that δ_N is a function of four variables: R, c_∞, T_w, and SSD. From a separate set of nucleation experiments, we determined SSD values on our surface to be of the order of 0.1 or less (see Section 1 of Supporting Information). Using classical nucleation theory to relate SSD to the (receding) intrinsic contact angle [141] we found that this corresponded to an effective surface wettability of $\theta_r = 32.9° \pm 5.3°$ at the nucleation sites. While this is more hydrophilic than the global wettability of our hydrophobic surface ($\theta_r = 89° \pm 1°$ and $\theta_a = 113° \pm 1°$), this is readily explained by intrinsic surface defects inherent to all real-life surfaces that are well-known to locally decrease the SSD [63, 160].

When plotting the theoretical values of δ_N against the experimentally measured values of δ_{Cr}, the model did not match quantitatively or even qualitatively (Figures S2 and S3 in Supporting Information). We therefore hypothesize that the flux dry zone is dominant over the nucleation dry zone, at least when using ice as the hygroscopic agent. To test this hypothesis, we must now develop a theory for the flux dry zone.

7.2.3 Flux Dry Zone Model

To obtain a quantitative understanding of the flux dry zone, the in-plane evaporative flux (J_e) and out-of-plane condensation flux (J_c) of a liquid droplet at the periphery of the dry zone must be evaluated and balanced. The supercooled liquid condensate visible along the periphery of the dry zone is typically of radius $a \sim 1\text{-}10\,\mu\text{m}$, which is one hundred times smaller than the frozen droplet radius $R \sim 1\,\text{mm}$. As the liquid droplets defining the dry zone are micrometric, their Laplace pressure is small enough to approximate their vapor pressure as saturated [141]. We can then estimate the evaporative flux as $J_e \sim D(c_w - c_i)/\delta$, where D is the diffusivity of water vapor in air and δ is the edge-to-edge separation between a water droplet and ice droplet. The net

mass per unit time of the vapor condensing onto a liquid droplet is $\mathring{M} \sim (J_c - J_e)a^2$. Normalizing the total amount of matter condensing by $J_e a^2$, we get:

$$\mathring{M}^* \sim \frac{\delta J_c}{D(c_w - c_i)} - 1 \ . \tag{7.3}$$

Regarding the condensation flux, Beysens and co-workers proposed that $J_c \sim D(c_\infty - c_w)/\zeta$, where c_∞ is the ambient vapor concentration and ζ is concentration boundary layer thickness [9, 63]. This scaling assumes that the concentration profile above a population of micrometric condensates is linear [8]. The droplet pattern in such a case can be approximated as a homogeneous water film with an average thickness h. It follows that $c = c_w + (c_\infty - c_w)(z - h)/\zeta$, where ζ is the concentration boundary layer thickness. Setting $\mathring{M}^* = 0$ to, this yields a flux dry zone of

$$\delta_F \sim \zeta \, (c_w - c_i)/(c_\infty - c_w) \ . \tag{7.4}$$

For a purely diffusive system with negligible convective effects, the concentration boundary layer thickness can be estimated as $\zeta \sim \left[(D\zeta_h^{3/2})/(4\sqrt{\alpha g(T_\infty - T_w)}) \right]^{1/3}$, where $\zeta_h \sim L_s \left(\alpha g(T_\infty - T_w)L_s^3/\nu^2 \right)^{-1/5}$ is the hydrodynamic boundary layer thickness, α and ν are the volumetric thermal expansion coefficient and kinematic viscosity of air, and L_s is the characteristic length scale of the condensing surface [8]. For our experiments, $L_s \approx 8\,\text{cm}$ and $\zeta \sim 1\,\text{mm}$ over the entire range of $(T_\infty - T_w)$, varying from $1.06 - 1.39$ mm. Plotting Equation 7.4 against our experimental values of δ_F obtained mixed results (Figure 7.3a). For smaller values of $(c_w - c_i)/(c_\infty - c_w)$, there was indeed a linear trend with δ_F as predicted by Eq. 7.4. However, the value of $\zeta = 1.3\,\text{cm}$ that captured the linear trend is an order of magnitude higher than expected. Further, the experimental δ_{Cr} values increasingly moved away from the linear regime as $(c_w - c_i)/(c_\infty - c_w)$ was increased by 3 orders of magnitude and c_∞ approached c_w. These discrepancies suggest that the scaling model developed by Beysens et al. may not be universally true.

The root of the apparent conundrum can be realized by revisiting the stipulations of Equation 7.4. First, the assumption of a constant ζ holds as long as the droplets on the substrate are all much smaller than ζ. The radius of our frozen droplet scales with the boundary layer above the micrometric droplets, $R \sim \zeta \sim 1\,\text{mm}$, and therefore would locally extend the boundary layer over its free interface. Second, the assumption of a linear concentration profile only holds in the limit of $\delta \gg R$, that is, far from the frozen droplet. However, experimentally observed dry zone lengths are smaller than R or, at best, scale as $\delta_{Cr} \sim R$ (cf. Figure 7.2), undermining the ability to assume a linear out-of-plane concentration profile.

We now abandon the linearity assumption and instead note that the mass flux condensing onto the substrate is equal to the mass flux at infinity: $J_c \sim J_\infty \sim c_\infty U$, where U is the velocity of the ambient vapor far from the substrate. This in combination with Equation 7.3 for $\mathring{M}^* = 0$ yields a new scaling for the flux dry zone:

$$\delta_F \sim l_D(c_w - c_i)/c_\infty \ , \tag{7.5}$$
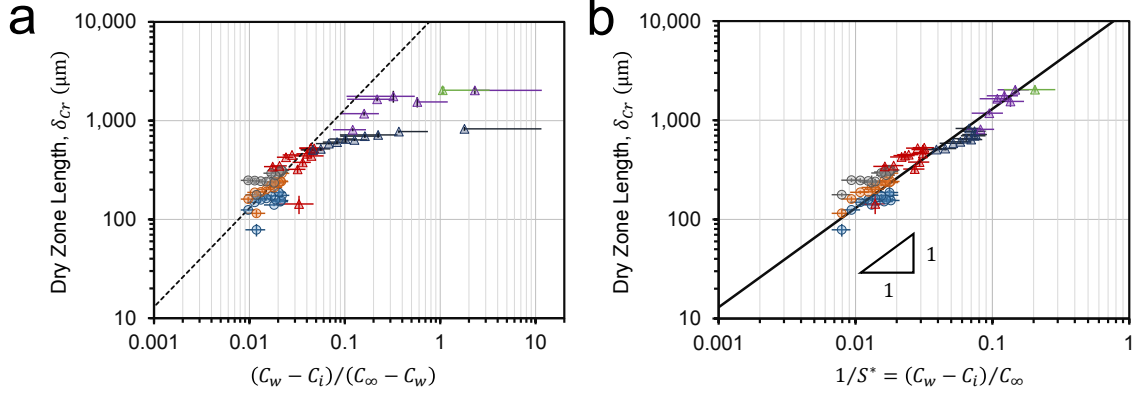
FIGURE 7.3: Dry Zone Scaling Laws. a) When dry zone lengths are plotted against $(c_w - c_i)/(c_\infty - c_w)$, corresponding to the original model for flux dry zones (Eq. 7.4) [9], they increasingly move away from the power law slope of 1 at higher values. b) When instead plotting against $(c_w - c_i)/c_\infty$, which corresponds to our new model for flux dry zones (Eq. 7.5), we see all the data collapses onto a single curve with a slope of 1. This shows that the scaling law that governs flux dry zones when $\zeta/R \sim 1$ is $\delta_F \sim RPe^{-1}S^{*-1}$, where Pe is the Péclet Number and $S^* = (c_w - c_i)/c_\infty$.

where $l_D \sim D/U$ is a diffusive length scale. Equation 7.5 is first plotted against all data collected in Figure 2, with excellent agreement. Furthermore, when plotting δ_{Cr} against $(c_w - c_i)/c_\infty$ in Figure 3b, all of the experimental dry zone values collapse onto a universal curve, validating Equation 7.5 as the emergent scaling law for flux dry zones around humidity sinks.

The diffusive length scale l_D is in fact related to a well-known non-dimensional number called the diffusive Péclet number: $Pe = RU/D = R/l_D$. The emergent value of $l_D = 1.3$ cm from our experiments corresponds to a $Pe \approx 0.08$. The Péclet number compares advective transport to diffusive transport and is thus expected to be much less than 1 for a diffusion-driven system as ours [198]. Furthermore, since l_D represents the vertical height at the periphery of the dry zone where the vapor concentration effectively reaches c_∞, we can estimate its value by solving $\nabla^2 c = 0$ in the vicinity of the frozen droplet. Rescaling the variables as $c^* = (c - c_i)/(c_\infty - c_i)$ and $r^* = r/R$, we get $\nabla^2 c^* = 0$. With the boundary conditions $c^*(r^* = 1) = 0$ and $c^*(r^* \to \infty) \to 1$, we obtain the solution of $c^* = 1 - 1/r^*$. An effective boundary layer thickness can be expressed as $c^* \gtrsim 0.9$. A boundary layer thickness of $l_D = 1.3$ cm around our milimetric frozen droplet, as found in our experiments, corresponds to a $c^* \approx 0.923$, further confirming our scaling. By introducing another dimensionless number comparing the ambient concentration to the differential between water and ice, $S^* \sim c_\infty/(c_w - c_i)$, Equation 7.5 can be succinctly expressed as $\delta_F \sim RPe^{-1}S^{*-1}$. This scaling law is further corroborated by numerical simulations that solved the diffusion equation in order to obtain the critical dry zone length around ice (see Section 5 and Figure S4 in the Supporting Information).
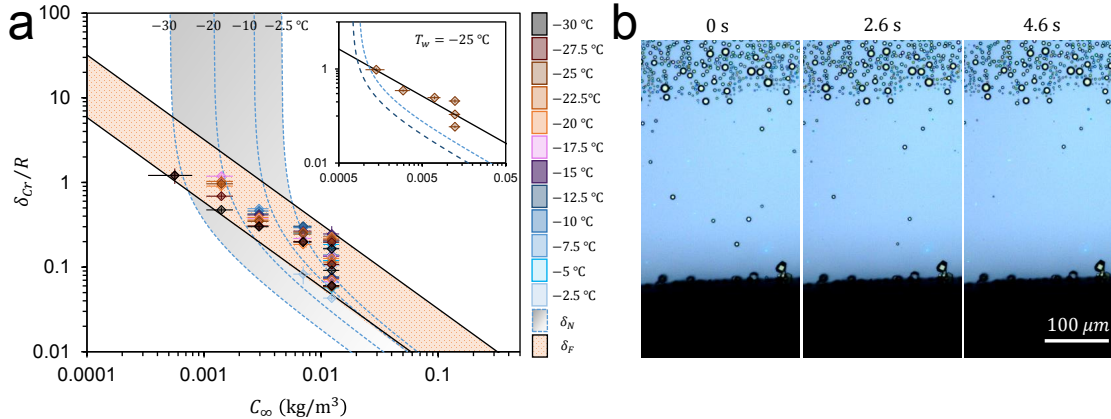
FIGURE 7.4: a) Phase Map of Nucleation and Flux Dry Zones. Dry zone lengths are nondimensionalized with the radius of the frozen droplet and plotted against the ambient vapor concentration. The gray and orange regions correspond to the theoretical values of nucleation dry zones (δ_N^*, Equation 7.2) and flux dry zones (δ_F^*, Equation 7.5), respectively. Any line running within and parallel to the gray or orange bands represents a given surface temperature where $c_w - c_i$ and SSD are fixed, such that δ_N^* and δ_F^* depend only upon c_∞. Here, a constant value of $SSD \approx 0.128$ for all temperatures was used to calculate δ_N^*, as indicated by our experimental observations (see Section 1 of Supporting Information). The upper and lower bounds of the orange band correspond to the minimum and maximum values of $c_w - c_i$ from our experiments, which were obtained at temperatures of $T_w = -12.5°C$ and $-30°C$, respectively. The experimental data points, collected from Figure 7.2b,d and color coded by the substrate temperature, universally fall within the orange region to suggest that the flux dry zone is always dominant ($\delta_{Cr}^* \sim \delta_F$). Inset: A simplified version of the same plot, where only $T_w = -25°C$ is considered. The dotted and the dashed blue lines represent nucleation dry zones corresponding to $SSD_{max} = 0.23$ and $SSD_{min} = 0.03$, as determined from. Comparisons of δ_{Cr} against theoretical values of δ_N and δ_F for all 12 choices of T_w are provided in Figure S5 of the Supporting Information. b) When rain droplets fell within the dry zone (first panel), they completely evaporated within seconds (second and third panels) while the droplets at the periphery of the dry zone remained unchanged in size.

7.2.4 Phase Map

A phase map is constructed in Figure 7.4 to directly compare nucleation dry zones (Equation 7.2) and flux dry zones (Equation 7.5). When superimposing our experimental data (cf. Figure 7.2) onto the phase map, we find that $\delta_N > \delta_F$ is only possible when the substrate is extremely close to the dew point. In other words, as $c_\infty \to c_N$, the nucleation dry zone shoots up asymptotically toward infinity and $\delta_N > \delta_F$ is true. The phase map shows that all of our experimental dry zone lengths fall in the orange region corresponding to flux dry zones: $\delta_F > \delta_N$. Obtaining data points in the

asymptotic region of δ_N would require exceptional control over the ambient humidity and substrate temperature, as even a slight variation may cause it collapse to the flux curve. Our experimental set-up was not sensitive enough for such near-dew point investigation. Nevertheless, our experimental findings and theoretical estimates provide conclusive evidence that the critical dry zone around a frozen droplet practically always corresponds to the flux dry zone, $\delta_{Cr} \sim \delta_F$. This explains why the experimental curves in both Figure 7.2b and 7.2d are qualitatively similar and all agree with Equation 7.5, despite the fact that both nucleation and flux dry zones were hypothetically possible in the former while only flux dry zones were possible for the latter.

As a final confirmation that δ_{Cr} is a flux dry zone, we observed that micrometric rain droplets was able to spontaneously form in the ambient air and gently fall onto the dry zone when the air was warm and humid ($H = 65.4\%, T_\infty = 23.8°\text{C}$) and the surface was sufficiently cold ($T_w = -30°\text{C}$). Every microdroplet landing within the dry zone promptly evaporated within a few seconds, regardless of which region of the dry zone it landed in, which provides direct experimental confirmation that the entire dry zone is a region of inhibited growth (Figure 7.4b).

A subtle question remains unanswered. It is well established that condensate initially nucleates with a nanometric embryo size (~ 1–$10\,\text{nm}$) [149]. Nanodroplets exhibit a supersaturated vapor concentration, which can be predicted by the Kelvin-Laplace equation: $\ln(c(a)/c_w) = -2\sigma \bar{R} T_w/(av)$ where σ is the surface tension of water, $\bar{R}$ and v are the gas constant and molar volume of water vapor, and a is the droplet's nanometric radius of curvature. It follows that the in-plane concentration gradient between a supersaturated nanodroplet and an ice droplet, $c_{w,\text{nano}} - c_i$, would be significantly larger than that between a micrometric (saturated) droplet and ice, $c_w - c_i$. From Equation 7.5, this mandates that the flux dry zone must be larger when considering a nanodroplet: $\delta_{F,\text{nano}} > \delta_F$. Why then, does our experimentally observed dry zone correspond to δ_F and not $\delta_{F,\text{nano}}$? In other words, how were the nanodroplets able to initially grow into the flux-balanced microdroplets observed along the periphery of δ_F, when a negative mass flux would be predicted for these nanodroplets? The answer is found by recalling that the nucleation dry zone is always smaller than the flux dry zone ($\delta_N < \delta_F$). This means that when droplets nucleate on the surface for the first time, the dry zone is initially smaller (δ_N), but then expands as these nucleated droplets evaporate, which is indeed what we observe here (Figure S6 in Supporting Information). We have previously observed that when ice is placed next to a vast array of droplets, it can only evaporate the closest row of droplets [63]. Thus, the nucleated nanodroplets will indeed disappear, but only one row at a time. By the time the ice droplet is interacting with the row of droplets corresponding to the flux dry zone, they have already grown to a micrometric size, which is why we obtain δ_F and not $\delta_{F,\text{nano}}$.

Finally, we note that when the frozen droplet is of the same size as the liquid microcondensate, the concentration profiles over all the droplets in the system can overlap, establishing a linear concentration variation in the vertical direction. In such

a case, $\zeta/R >> 1$ and dry zone lengths should indeed follow the Beysens' scaling law, $\delta_{Cr} \sim \zeta(c_w - c_i)/(c_\infty - c_i)$ [8]. Experimentally observed dry zones at this length scale are of the order of $\delta \sim 10\mu$m, which also follows from the scaling law for typical values of $\zeta \sim 1$mm. Such dry zones though are transient and collapse due to the formation of inter-droplet ice bridges from the frozen droplet to the liquid droplets [6, 57, 63]. These bridges grow at a rate of $v \sim D(c_w - c_i)/(\rho_i \delta)$, where ρ_i is the density of ice. For typical values of the different parameters ($D \sim 10^{-5}$ m^2/s, $\rho \sim 1$ kg/m^3, $(c_w - c_i) \sim 10^{-4}$ kg/m^3), we get $v \sim 0.1 - 1\,\mu m/s$. Thus the dry zones collapse within a matter of seconds as the ice bridges eventually connect to the neighboring liquid droplets, ensuing a chain reaction of percolating ice bridges that propagate through the entire population of supercooled condensate. However, in the case of milimetric frozen droplets, the dry zone seemed quite stable with no noticeable ice bridges growing from the frozen droplet. This can be rationalized by now considering the case where $\zeta/R \sim 1$ and the dry zone follows the scaling law $\delta_{Cr} \sim RPe^{-1}S^{*-1}$. As we saw in our experiments, this leads to much larger dry zones, $\delta_{Cr} \sim 100$–$1,000\,\mu$m. If we now estimate the bridge growth rate owing to the in-plane vapor flow for this δ, we find that $v \sim 10$ nm/s. In reality, the ambient vapor may also contribute to the in-plane growth of the ice droplet, but we observed in our experiments that out-of-plane growth was dominant. Indeed, the supercooled condensate beyond the dry zone was observed to freeze due to heterogeneous nucleation and ice bridging well before any noticeable ice bridges could begin. As such, we always get stable equilibrium dry zones around milimetric frozen droplets. Interestingly, if we keep increasing the size of the frozen droplet, the height would get capped at the capillary length scale $l_c = \sqrt{\sigma/\rho g}$ which is around 2.7 mm [163]. Thus the dry zone length would also get capped at $\delta_{Cr} \sim l_c Pe^{-1}S^{*-1}$ and would not increase any further.

7.3 Conclusion

In conclusion, we have obtained stable dry zones around hygroscopic ice droplets. The length of an annular dry zone depends upon the ambient vapor concentration, surface temperature, and the size of the ice droplet. Across a very wide parameter space, the experimental dry zones collapsed onto a universal scaling law corresponding to a region of inhibited droplet growth. Regarding the dueling mechanisms of a nucleation dry zone versus a flux dry zone, we can therefore declare the flux dry zone the emphatic victor. We hope that our physical model can rationalize future work on anti-fogging and anti-frosting surfaces that utilize overlapping dry zones between hygroscopic materials such as glycols, salts, or even ice itself!

8
Conclusions and Future Work

"You say why and I say I don't know..."

— The Beatles

The content of this chapter was previously published as a subsection of a journal manuscript in [14], and reproduced here with minor modifications. This chapter summarizes the key findings of the thesis and discusses future work in the context of anti-frosting strategies.

8.1   Summary

Our motivation behind this work, as outline in Chapter 1, has been understand the physics of condensation frosting, in particular, the phenomena of ice bridges and dry zones. We have indeed accomplished that step by step in chapters 3–7. Our observations can be summarized as follows:

First, in Chapter 3, using classical nucleation theory and Becker-Döring embryo formation kinetics, we formulated a comprehensive framework that can be utilized for studying localized vapor pressure gradients in mixed-mode phase change systems. Herein, we showed that the supersaturation degree (SSD) required for nucleation on a substrate was calculated as a function of surface temperature and wettability. While we agree with a previous report that SSD is always higher for desublimation than for condensation [7], by considering the SSD in conjunction with the difference in saturation pressure between water and ice, we showed that desublimation can actually be the thermodynamically favorable mode of nucleation at sufficiently low surface temperatures and wettabilities. This is in contrast to previous reports that stated that condensation is always the favored mode of nucleation. Furthermore, we saw that the SSD around pre-existing droplets can be calculated for liquid droplets using the Kelvin-Laplace equation and for frost by considering the free energy required to nucleate a disk-shaped embryo on top of the ice.

In Chapter 4, we used our previous model to contextualize the recently reported "frost halo" effect [4], where the rapid increase in temperature and vapor pressure of a freezing droplet can illicit a ring of nucleation on the surrounding substrate. We created a phase map for frost halos and showed that three seperate regimes are possible depending on the temperature and wettability of the substrate: no halo, a condensation halo, or a desublimation halo. To our knowledge, this is the first mention of a desublimation halo being possible, which will hopefully inspire experimental validation.

In Chapter 5, we investigate inter-droplet ice bridging between frozen condensate and neighboring liquid condensate that has been very recently shown to be the primary mechanism of in-plane frost growth on non-wetting surfaces [6, 57]. Following extensive experiments on ice bridging in a custom-made humidity chamber over wide parameter space for droplet sizes ranging from 1μm-1 mm, we investigated the critical condition for the ice bridge to connect to its neighboring liquid droplet. Our experiments show that the success and failure of ice bridge connections are independent of growth rate of ice bridge, substrate temperature, ambient temperature and humidity and only a function of the droplet sizes and inter-droplet distance. Correspondingly we derived scaling laws which capture the physics of this phenomena, that are in excellent agreement with the experiments. Subsequently, we formulated a first order scaling model for the growth rate of ice bridges, and show how it is consistent with are experiments. Previously, in Chapter 3, we had shown that the kinetics of embryo formation on ice, unlike that of a dry substrate, are not known and therefore the extent of supersaturation required to grow frost has been a long-

standing debate. Here we show that experimental measurements of inter-droplet ice bridging, which are highly sensitive to vapor pressures, demonstrate that the vapor pressure required to grow frost must be approximately saturated. This also suggests that desublimation on ice should always be the thermodynamically favorable mode of nucleation. Although the growing frost considered here was in the context of frost bridges, we expect that our finding of saturated vapor conditions should extend to more general cases such as macroscopic frost sheets.

In Chapter 6, based of our understanding of ice bridging and its dependency on inter-droplet distance, we try to control global frost propagation on a planar substrate. We do this designing chemically patterned surfaces that can spatially control the growth of supercooled condensation. The functionalized surface also has a water pad, which we can deliberately freeze to trigger the first freezing event, giving us temporal control on the start of frost propagation. Our experiments revealed that using patterned surfaces, not only could the geometry and speed of inter-droplet frost growth be controlled, it could also be completely halted. For the first time, we showed that inter-droplet ice bridging could be stopped by utilizing sufficiently dilute hydrophilic patterns and by triggering a very early freezing event near the patterned condensation. This leads to a dry zone around the frozen water pad where no condensation or ice can grow.

In Chapter 7 we systematically investigated the formation of dry zones around frozen droplets. This brought us to the broader question of whether dry zones around hygroscpoic droplets are regions of inhibited nucleation or inhibited growth. We elucidated the competition between these two mechanisms by generating steady-state dry zones about frozen water droplets serving as our hygroscopic agents, which are unique in their ability to remain undiluted throughout water harvesting. We performed extensive experiments of dry zones forming around frozen droplets for different ice droplet sizes, substrate temperatures varying from $-30°C \leq T_w < 0°C$, supersaturation varying two orders of magnitude. Our findings revealed that over the vast majority of the parameter space, the flux dry zone wins the duel over the nucleation dry zone, such that the size of all dry zones collapses onto a single scaling law. Our study on dry zones also opens up the possibility of creating frost-free surfaces using ice itself.

8.2 Future Directions: Anti-Frosting Strategies

Now that we understand the incipient stages of condensation frosting, we can use this knowledge to create frost-free surfaces. The most promising strategy for passively preventing ice formation up until now has been to fabricate surfaces that (1) delay the freezing of supercooled water and (2) exhibit a very low contact angle hysteresis. When both of these features are in place, supercooled water impacting the surface is able to bounce/slide off the substrate before the onset of heterogeneous ice nucleation [95, 103–107]. At first glance, this strategy may also seem amenable for the promo-

tion of anti-frosting, considering that the dynamical removal of condensate can be achieved by gravity at millimetric length scales [95, 103] or by coalescence-induced jumping at micrometric length scales [6, 58]. However, even when supercooled condensate is continually removed from the substrate by sliding and/or jumping, frost inevitably forms due to the heterogeneous nucleation of ice at edge defects, which subsequently propagates frost across the entire surface via inter-droplet ice bridging [6, 119]. If the edge defects are shielded, for example by using a rubber gasket, ice nucleation will still occur due to surface defects caused by dust particles and other unavoidable imperfections [118]. Even on liquid-impregnated surfaces, [199] where both hysteresis and surface defects are minimal, ice nucleation is followed by spontaneous oil migration onto the frozen droplets, causing irreversible damage to the self-healing properties of the surface [104]. Since heterogeneous ice nucleation will eventually occur somewhere on any real-life surface, promoting a delay in freezing onset is actually harmful for the context of anti-frosting efforts, as the rate of inter-droplet ice bridging propagating from this point source will significantly increase due to the increased size and surface coverage of the supercooled condensate [6, 63]. Thus, we see that anti-icing techniques do not typically translate to anti-frosting except for the unlikely case where the delay in ice nucleation achieved for all supercooled condensation is greater than the time for which the system needs to be kept frost-free.

So, what is an appropriate anti-frosting strategy?

Now that it is clear that inter-droplet ice bridging is the primary mechanism for in-plane frost growth, we suggest that the only viable anti-frosting strategies are to (1) promote the failure of inter-droplet ice bridges (i.e. water droplets evaporate before bridge connects), or (2) prevent the nucleation and growth of any nearby supercooled droplets so bridges cannot grow at all. Both of these approaches to creating a dry zone, free from condensation and frost, are best accomplished by the use of hygroscopic humidity sinks such as salty water [8, 9, 146], nectar [147], or glycols [10]. Historically, the germ of the idea of dry zones was seeded in the works of Lopez et al. [169] in 1993 and Aizenberg et al. in 1999 [188] that established how patterned surface functionalization can be utilized for spatial control of nucleation. However, these dry zones were reported as regions where *nucleation* was inhibited because the Gibbs free energy requirement had been increased by surface functionalization. Such nucleation dry zones are different from flux dry zones that emerge from the cooperative diffusion mechanism between condensing droplets [142] (see Stage IV), where *growth* is suppressed by the presence of neighboring humidity sinks that evaporate any condensing embryos. The first demonstration of overlapping flux dry zones was performed by Schäffle and co-workers in 2003 [143] well before the discovery of ice bridging. This clever study distributed an array of diethylene glycol droplets on a chemically patterned substrate to keep the intermediate surface area dry from condensate. More recent works have extended the concept of overlapping dry zones to supercooled condensate, in order to help suppress condensation frosting. Guadarrama–Cetina et al. showed that a salt crystal can promote an annular dry
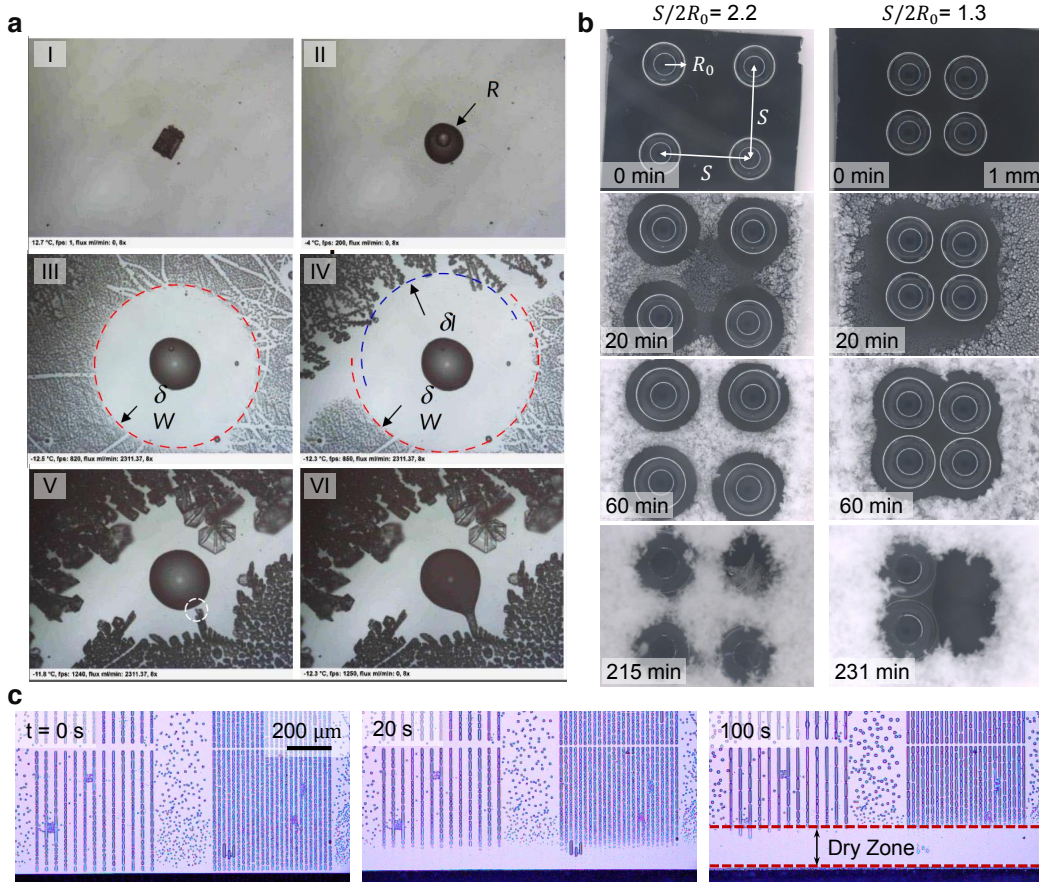
FIGURE 8.1: (a) Frost-phobic dry zone around a salty water droplet. [9] (I) $t = 0$ – Salt crystal just after deposition, (II) $t = 8$ s– Partial crystal dissolution, (III) $t = 30$ s– Condensation dry zone forming around the salty water droplet when under humid air is flown at 2.3 L/min; air saturated with water at 17°C, (IV) $t = 34$ s– Icing in the left diagonal, demonstrating a dry zone δ_I towards ice, while a condensation dry zone δ_W is visible towards water. (V) $t = 49.6$ s— 40 ms before the growing ice bridge can connect to the salty water droplet (white circle), and (VI) $t = 50$ s Upon contact, the salty droplet immediately freezes. Reprinted with permission from [52]; copyright 2015, IOP Publishing. (b) Using hygroscopic antifreeze liquids to prevent frost growth. Inhibition of condensation frosting around four $2\,\mu$L propylene glycol (PG) droplets over time [10]. Reprinted from [51]. Copyright 2015, American Chemical Society. (c) Using ice itself to prevent frost growth. The freezing of a film of water (visible at the bottom of the images) at $T_s = -5\,°$C and subsequent cooling to $T_w = -12.5\,°$C evaporates the condensate around it to cause a global failure of ice bridge connections. The condensate in these experiments have been grown on hydrophilic stripes and freezing causes evaporation along these stripes to halt interdroplet frost growth. Reprinted with permission from [50]; copyright 2016, Nature Publishing Group.
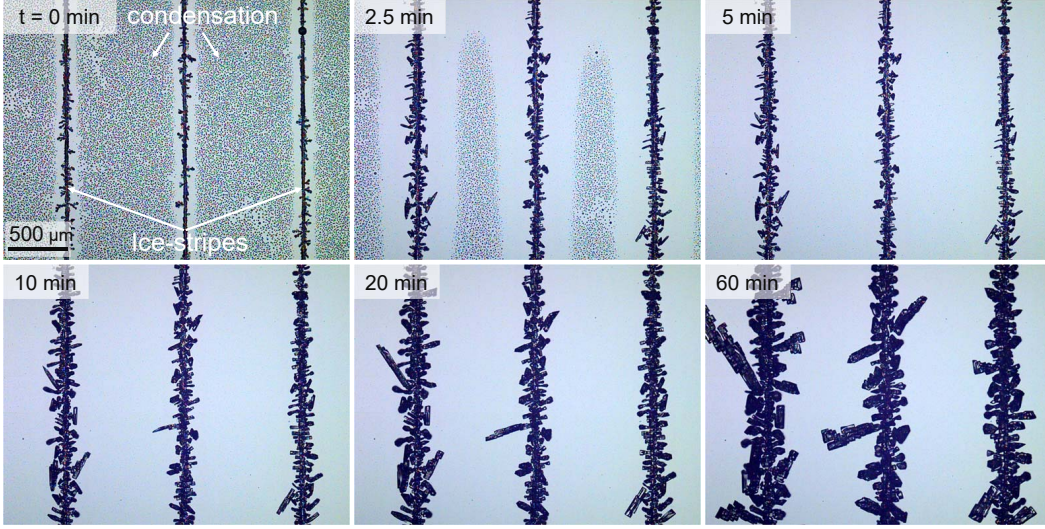
FIGURE 8.2: Experimental micrographs show how our proposed anti-frosting surface can create scalable frost-free surfaces using ice itself. 10μm water stripes with 1 mm inter-stripe distances are frozen. The ice stripes keep the intermittent distances dry because of overlapping dry zones. Experiment shows at a substrate temperature of $T_w = -8°$C and a supersaturation S=1.2, near 90% of our surface is with no frost or condensation after 5 min. However, over the course of an hour, the ice stripes significantly coarsen from the ambient vapor and decrease the surface coverage substantially.

zone for both supercooled condensate and frost [9]. Sun et al. scaled this concept up by depositing arrays of droplets (composed of propylene glycol or salty water) across a substrate, confirming that when the dry zones overlap the intermediate area initially remains dry from condensate and frost even under supersaturated conditions [10].

When using traditional humidity sinks such as salt crystals or glycols, their hygroscopic properties are gradually lost as they continually harvest water vapor from the ambient and become diluted. As a result, the dry zones eventually break down and the frost proceeds to invade across the surface after only a few minutes have passed. [9, 10] It follows that the applicability of such an approach is constrained to the (rather impractical) case where the time required to dilute the humidity sinks exceeds the desired operation time of the system. Therefore we argue here that the best choice of hygroscopic material is, ironically enough, ice itself. After all, as ice harvests water vapor from the ambient (and any neighboring supercooled droplets), it remains pure ice. Therefore the depressed vapor pressure of ice with respect to water continues unabated, regardless of how much water has been harvested. In Figure 2.5d, we see a stable dry zone around ice, that is analogous to the dry zones we see around hygroscopic droplets [141]. Figure 8.1c shows the dynamic evolution of such a dry zone around a droplet that has just been frozen [63]. This shows a global

failure of all ice bridge connections from the frozen droplet. Thus, it seems only logical to have sequential arrays of ice itself to uniquely promote stable and overlapping dry zones in between. This should in principle severely suppress in-plane frosting in favor of out-of-plane ice growth at the sacrificial humidity sinks. We are currently investigating the validity and robustness of such an idea.

Figure 8.2 shows our preliminary attempt at this approach. Here we see that surfaces functionalized with chemical or physical micropatterns that facilitate microscopic arrays of ice stripes can passively suppress in-plane frost growth. The dry zones around each ice stripe can be as large as 1 mm and when these dry zones overlap, they render at least 90 % of the surface frost-free, demonstrating the scalability of this application. However, over a course of an hour these ice stripes coarsen and decrease the frost-free area.

Thus as of now, the most important future work, in extension of the work that has been done, is to find out a strategy to prevent the in-plane coarsening of ice stripes.

8.3   Conclusions

Despite the abundant amount of research articles in anti-icing and anti-frosting, the incipient stages of condensation frosting that lead to frost densification have just been discovered. To this end, the discovery of frost halos, ice bridging, and dry zones mark the departure of the physics of frosting from icing physics. In the wake of these new discoveries relating to condensation frosting, anti-frosting studies have just begun. Ideas are nascent and strategies inconclusive. Experiments have just started to open up a vast unanswered domain in the physics of bridging and dry zones. We hope the work in this thesis will inspire experimentalists and theoreticians alike to investigate and unravel the intricacies of these phenomena, leading to an exceptional control of in-plane frost growth on surfaces.

Appendix A

Supporting Information:

Phase Stability

A.1 Relevant Equations

The equations used for estimation of accurate saturation vapor pressure P (in Pa) of water and ice and latent heat of condensation h_{liq} (in J/mol) and desublimation h_{ice} (in J/mol)as a function of temperature T ((in J/mol)) with the appropriate correction terms are [20]:

For $236 < T < 273.16$ K
$$h_{liq} \approx 56579 - 42.212T + \exp 0.119(281.6 - T) \tag{S1}$$

For $123 < T < 332$ K

$$\begin{aligned} \ln(p_{liq}) \approx \ & 54.842763 - 6763.22/T - 4.210\ln(T) \\ & + 0.000367T + \tanh 0.0415(T - 218.8)(53.878 \\ & - 1331.22/T - 9.44523\ln(T) + 0.014025T) \end{aligned} \tag{S2}$$

For $T > 30$ K

$$\begin{aligned} h_{ice} = \ & 46782.5 + 35.8925T - 0.07414T^2 \\ & + 541.5\exp(-T/(281.6 - T))^2 \end{aligned} \tag{S3}$$

For $T > 110$ K

$$\begin{aligned} p_{ice} = \ & \exp(9.550426 - 5723.265/T \\ & + 3.53068\ln(T) - 0.00728332T) \end{aligned} \tag{S4}$$

The equations used for surface energy (J/m^2) as a function of temperature are [7, 11]

$$\sigma_{l,v} = (75.7 - 0.1775(T - 273.15)) \times 10^{-3} \tag{S5}$$

$$\sigma_{i,v} = (99.5 - 0.075(T - 273.15)) \times 10^{-3}, \tag{S6}$$

where $\sigma_{l,v}$ is the surface tension of liquid water with respect to vapor and $\sigma_{i,v}$ is the surface tension of ice with respect to vapor and temperature T is in K.

A.2 Comparison with Previous Studies: $SSD-\theta$ Plot
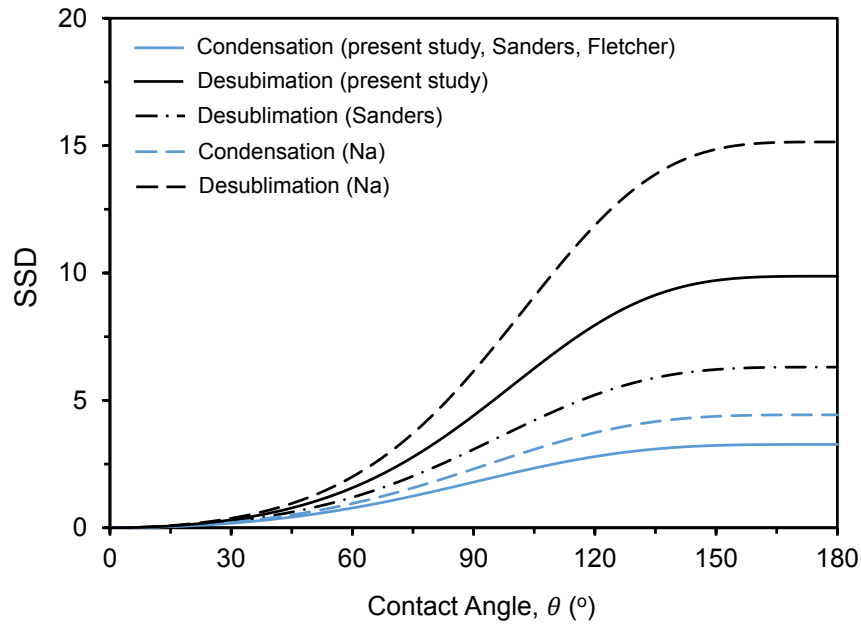
FIGURE A.1: Comparison between the plots for supersaturation degree SSD as obtained by Sanders [11], Fletcher [12], Na [7] and present study. Note that the nature of all the curves in the same. In particular, our condensation curve is in perfect agreement with that of both Sanders and Fletcher. However the desublimation curve of Sanders is lower than that of ours and that of Na is higher. It is not entirely clear why the desublimation curves in particular have had such variation in the past, but a possible explanation could be the lack of accurate data on saturation vapor pressures on ice.

A.3 Comparison with Previous Studies: $\Delta T - \theta$ Plot
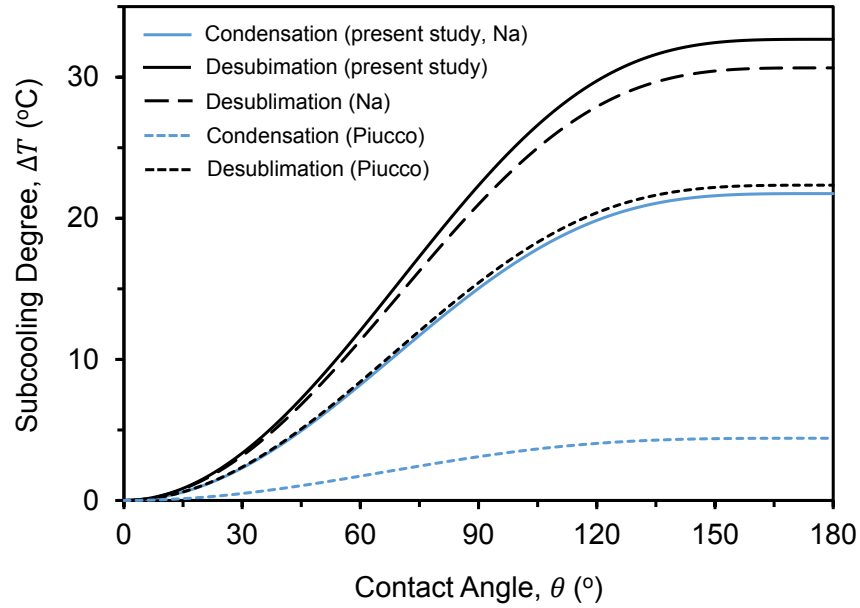
FIGURE A.2: Comparison between the plots for subcooling degree as obtained by Piucco et al. [13], Na et al. [7] and present study. Note that our condensation curve is in perfect agreement with that of Na, however the desublimation curve of Na is slightly lower than that of ours. It appears likely that the significant under-prediction of Piucco et al. has stemmed from an error induced in their surface energy equations (Equations S5 and S6) where they have used T instead of $T - 273.15$ where T is the temperature in Kelvin.

A.4 Subcooling Degree for Heterogeneous Nucleation
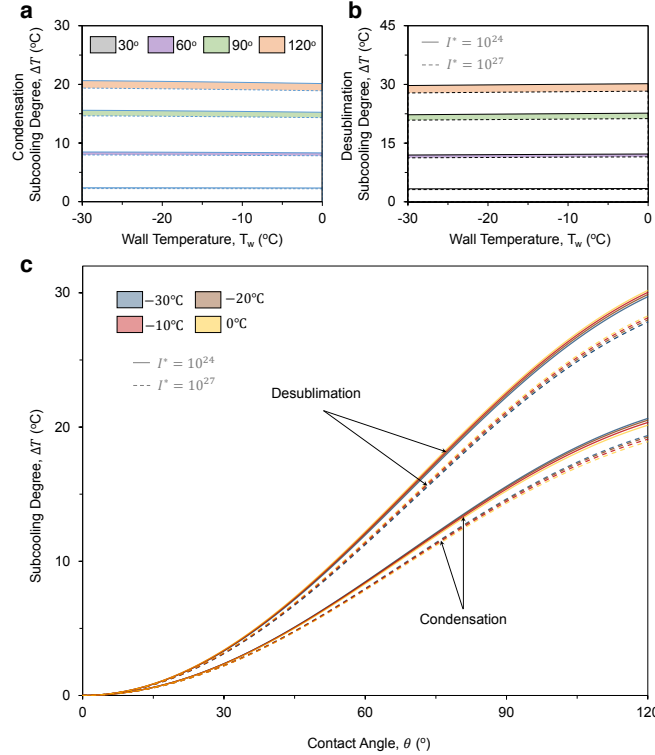
FIGURE A.3: Subcooling degree ΔT for condensation (a) and desublimation (b) as a function of wall temperature T_w for four different contact angles $\theta = 30°, 60°, 90°$C and $120°$C and two different embryo formation rates $I^* = 10^{24}$ and 10^{27}. (c) ΔT for both modes of nucleation as a function of wettability for wall temperatures $T_w = 0°$C, $-10°$C, $-20°$C and $-30°$C and embryo formation rates $I^* = 10^{24}$ and 10^{27}. Note that though both SSD and ΔT are analogous descriptions of heterogeneous nucleation, unlike SSD, ΔT remains fairly constant with temperature, for a given contact angle and mode of nucleation. This is why the ΔT–θ curves for a given mode of nucleation and embryo formation rate almost collapse on each other. The weak dependence of ΔT with respect to T_w can be seen in the direction of change in color. This shows that though the subcooling degree for desublimation is higher than that for condensation, the extent of subcooling required is strongly dependent on the wettability of a substrate. All plots are solutions to Eq. 4, 8 and 9.

A.5 Supersaturation Pressure for Heterogeneous Nucleation
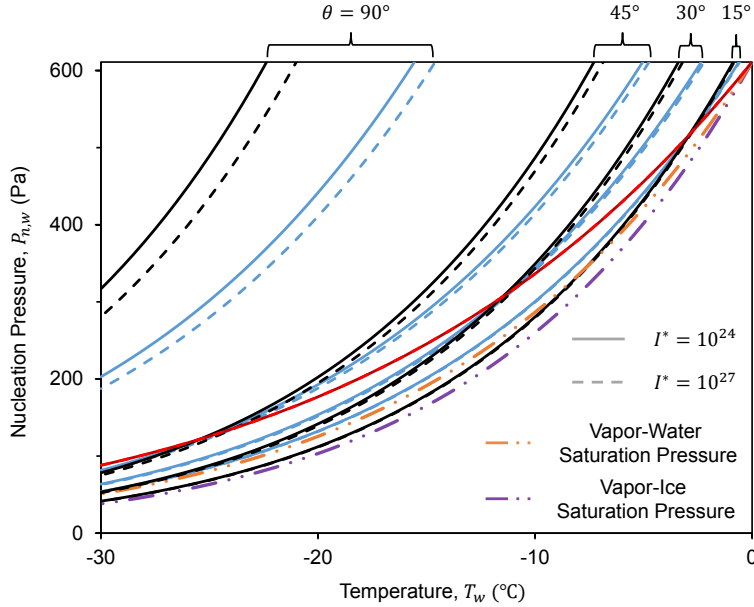
FIGURE A.4: Nucleation pressure $p_{n,w}$ required for condensation (blue lines) and desublimation (black lines) as a function of T_w for contact angles $\theta = 15°$, $30°$, $45°$, and $90°$ and embryo formation rates $I^* = 10^{24}$ and 10^{27}. The red dotted line is the locus of the intersection points of $p_{n,w}$ for the desublimation and condensation curves for contact angles ranging continuously from $0°$ to $120°$, where desublimation is favored to the left (or below) and condensation to the right (or above) of the red line. As expected we see nucleation pressure decreases with T_w. Also note, the more hydrophyllic the substrate, the lesser is the pressure required for nucleation at a given T_w. It is also interesting to note that at extremely hydrophilic angles, for example, $\theta = 15°$, the nucleation pressure requirement dips below even the saturation vapor pressure of water for temperatures below $T_w \approx -10\,°C$ (though always staying above the saturation vapor pressure above ice, as expected). This is strong evidence that indeed at low contact angles and sufficiently cold temperatures. In general, desublimation is the preferred mode of nucleation in the entire regime below the red line in where desublimation has a lower $p_{n,w}$ than that of condensation.

A.6 Thermodynamically Favored Mode of Heterogeneous Nucleation
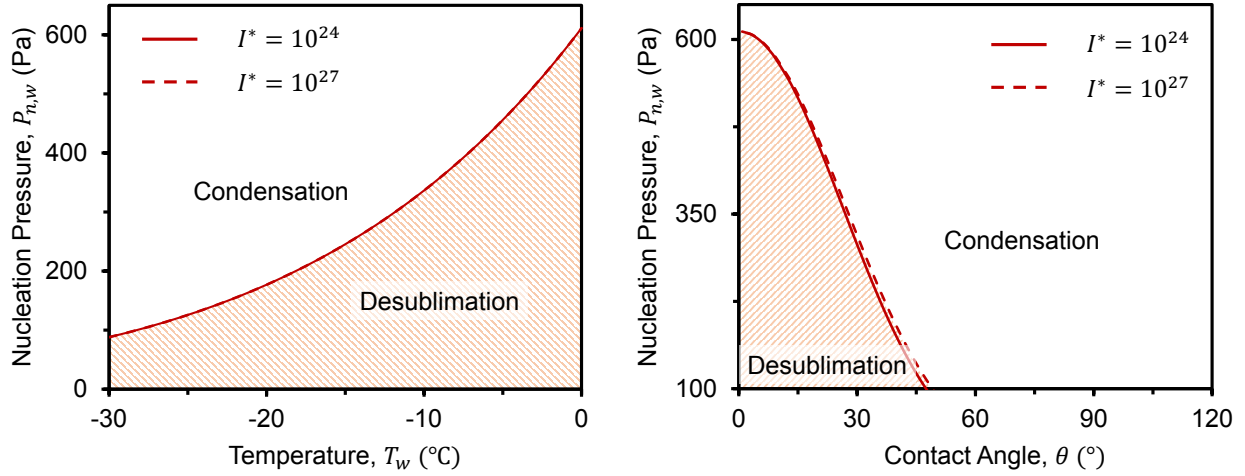
FIGURE A.5: (a) Phase diagram for the thermodynamically favored mode of nucleation for any pressure and surface temperature. Supercooled condensation is favorable in the phase space above the critical line and desublimation is preferred below. (b) Phase diagram for the same for any pressure and wettability, condensation being favored in the phase space to the right of the critical line and desublimation to the left. The solid lines correspond to $I^* = 10^{24}$ and the dashed lines correspond to $I^* = 10^{27}$. Note that these plots assume $\theta_{ice} = \theta_{water}$. In reality since on any substrate $\theta_{ice} > \theta_{water}$ [11], the red-lines will be shifted a bit lower than what we see in these plots.

A.7 Nucleation Pressure on Ice
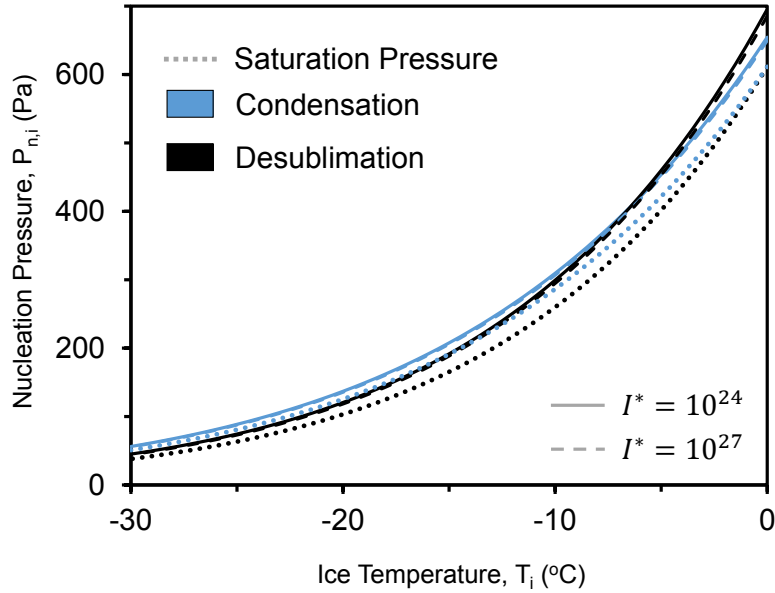
FIGURE A.6:   Vapor pressure required for nucleation $p_{n,i}$ on pre-existing ice as a function of the ice temperature. Blue/black lines represent the pressure to nucleate water/ice on ice when $I^* = 10^{24}$ (solid line), $I^* = 10^{27}$ (dashed line), or under saturated conditions (dotted lines). Assuming supersaturated conditions, condensation becomes the favorable mode of nucleation on ice above a critical temperature ($T_i > -6\,^\circ\text{C}$ for $I^* = 10^{24}$ or $I^* = 10^{27}$), while desublimation always exhibits a lower $p_{n,i}$ for nucleation occurring under approximately saturated conditions. However, embryo formation rates $I^* = 10^{24} - 10^{27}$ are not applicable to the cases of nucleation on ice, as we show in our Results and Discussion Section.

Appendix B

Controlling Frost Growth

B.1 Microfabrication Procedure
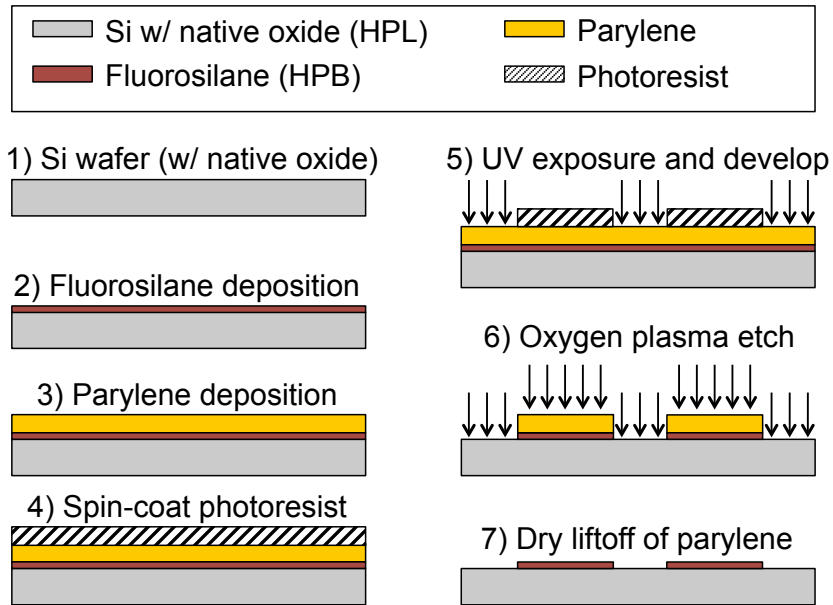
FIGURE B.1: Schematic of the procedure for the microfabrication of the chemical patterns. See Methods in the main text for more detailed information.

B.2 Atomic Force Microscopy
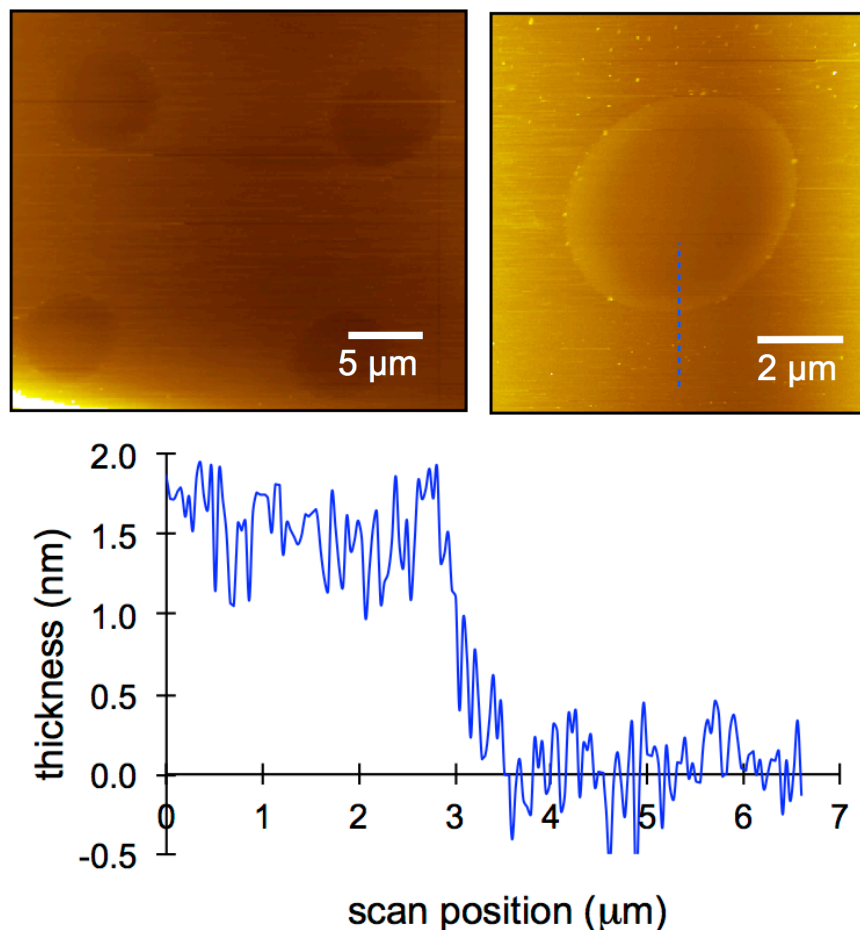
FIGURE B.2: Atomic force microscopy of the chemical micropatterns. The blue dotted line in the upper-right micrograph represents the line scan depicted below graphically. The average thickness of 1.5 nm corresponds to a self-assembled silane monolayer comprising the hydrophobic surface. Note that while the hydrophilic circles shown here are $5\,\mu$m in diameter compared to the $10\,\mu$m patterns used in the condensation/frosting experiments, the fabrication steps to create the patterns were identical.

B.3 Spatial Control of Condensation
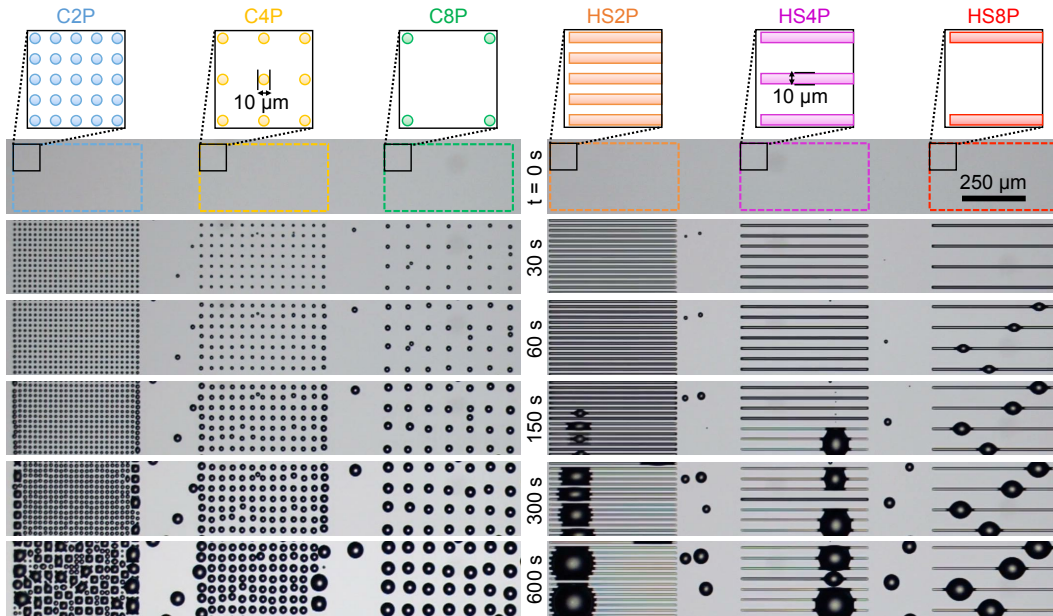
FIGURE B.3: Spatial control of condensation on smooth chemical micropatterns composed of arrays of circles or stripes. The colored shapes in the schematics represent the hydrophilic features while the white background is hydrophobic. Time zero corresponds to the onset of cooling from 10°C down to a steady-state temperature of $T_s = 5\,°\mathrm{C}$ from 5 s onward.
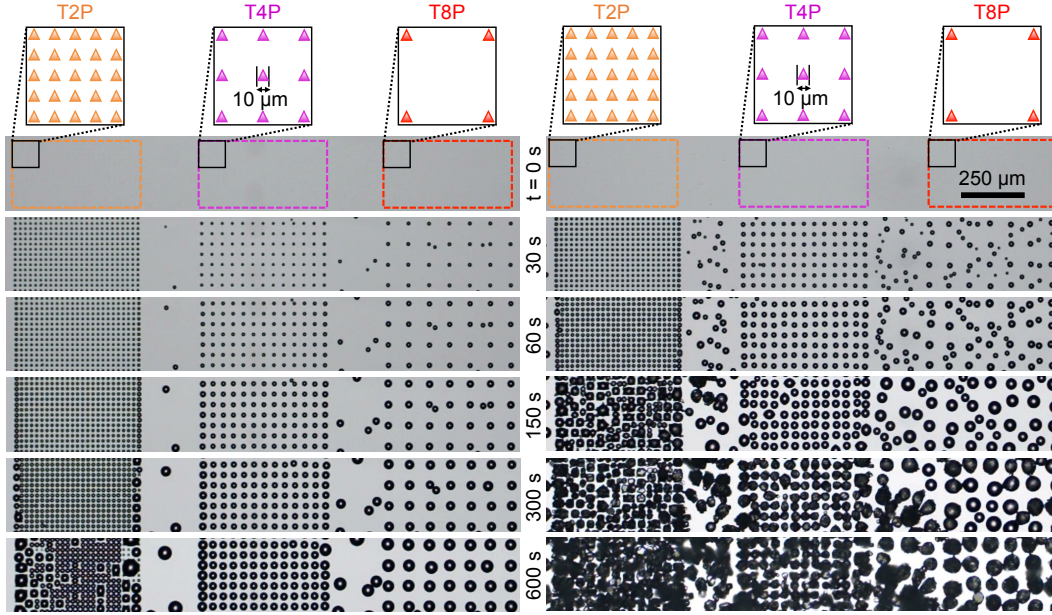
FIGURE B.4: Spatial control of condensation on smooth chemical micropatterns composed of arrays of hydrophilic triangles. Time zero corresponds to the onset of cooling from 10°C down to a steady-state temperature of $T_s = 5\,°\mathrm{C}$ (images on left) or $T_s = -10\,°\mathrm{C}$ (right).
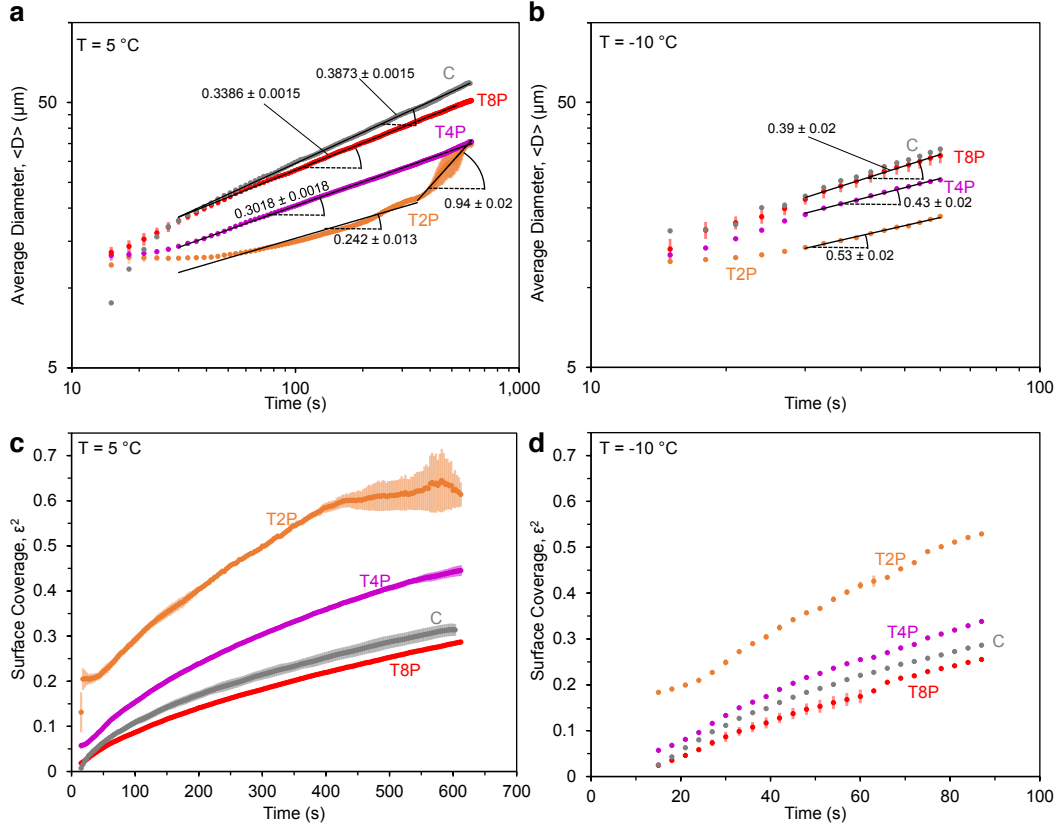
FIGURE B.5: Average diameter and surface coverage of condensation growing on arrays of hydrophilic triangles. (**a**) In a manner equivalent to condensation on the circle arrays (cf. Fig. 2), the growth rate of isolated condensation on T4P or T2P was smaller than the typical $\alpha \approx 1/3$ rule at a low supersaturation ($S = 1.2$). As previously discussed, this is likely due to the combination of a highly elevated nucleation density and a small supersaturation serving to increase the boundary layer of the vapor pressure gradient. (**b**) Also in a manner similar to the circle arrays, the growth rate of isolated condensate on T4P and T2P was higher than the $\alpha \approx 1/3$ rule at higher supersaturations ($S = 3.5$). Unlike with the circle arrays, heterogeneous nucleation and frost growth occurred only several minutes into the experiment, so the growth rates at a plateau surface coverage could not be measured. (**c,d**) As with the circle arrays, the surface coverage of condensate was larger for T2P and T4P compared to the uniformly hydrophobic control surface (C).

100
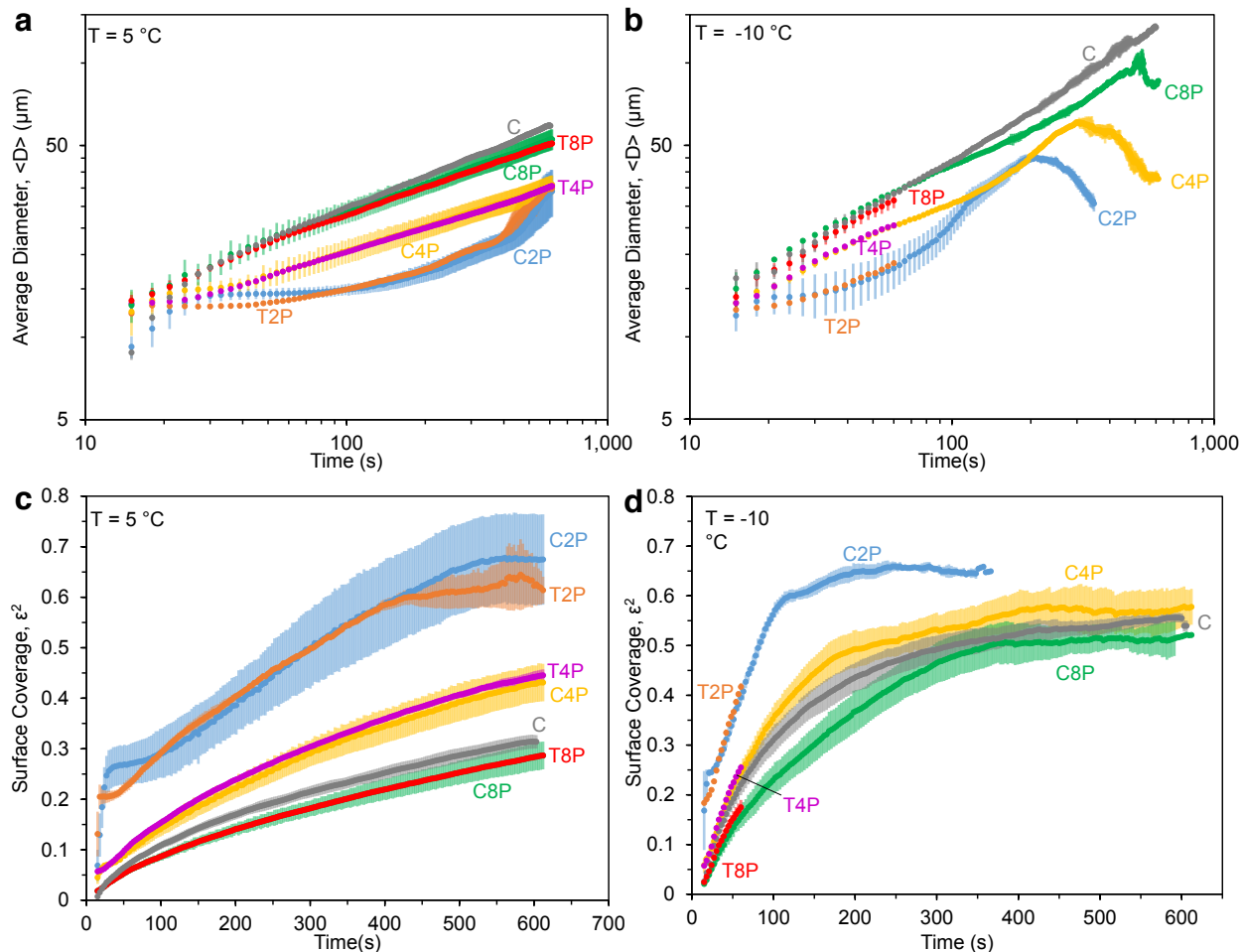
FIGURE B.6: A direct comparison of condensation on the circle arrays and triangle arrays (overlay of Fig. 2 and Supplementary Fig. S5). Because the water nucleating on the hydrophilic patterns tends to grow beyond the hydrophilic/hydrophobic borders within a few seconds, the condensation growth on the circles versus triangles is essentially equivalent.
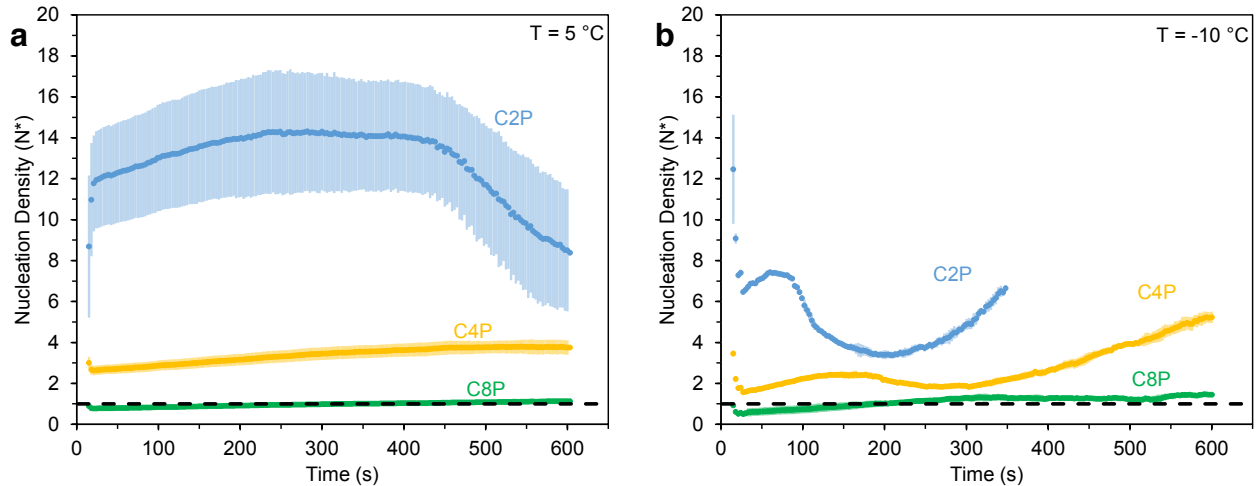
FIGURE B.7: The dimensionless nucleation density, where $N^*(t)$ is the ratio of droplets nucleated on each patterned surface to the number of droplets nucleated on the uniformly hydrophobic control surface. (**a**) At lower supersaturations ($S = 1.2$), the nucleation density is significantly higher on the C2P and C4P surfaces, especially for C2P where $N^* > 10$. Conversely, for patterns with a larger pitch between features (C8P), $N^* < 1$ for the first several minutes of condensation. (**b**) The nucleation density is still larger for C2P and C4P compared to the control surface (C) at higher supersaturations ($S = 3.5$), but the effect is less pronounced. This is because droplets tend to nucleate on the hydrophilic patterns regardless of the extent of supersaturation, whereas more droplets can nucleate on the control surface at the higher supersaturation.

B.4   The "Ice Shrapnel" Effect
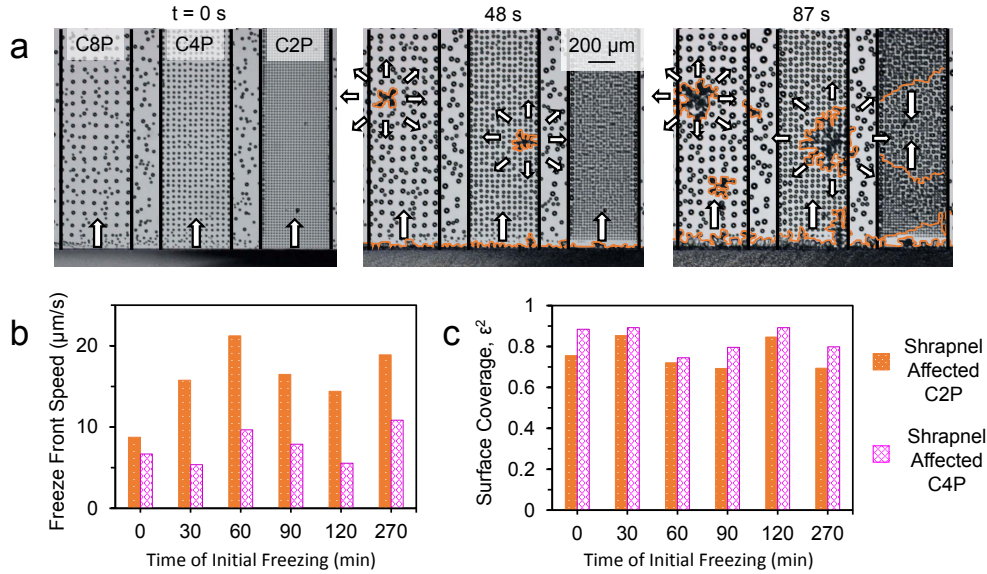
FIGURE B.8: Characterizing the "ice shrapnel" effect. (**a**) Under ambient conditions of $T_\infty = 21\,°C$ and $H = 40\,\%$, the patterned substrate was cooled to a steady-state temperature of $T_s = -10\,°C$. Immediately upon reaching steady-state, the thin film of supercooled water (bottom of screen) happened to freeze due to heterogeneous nucleation at the liquid-solid interface (1st frame). In the seconds after this initial freezing event, small pieces of ice appeared at random sites on the surface (second frame) which were likely ejected from the initial freezing event and are therefore termed "ice shrapnel." The frost proceeded to grow across the surface in two different ways: inter-droplet ice bridges that grew from the frozen film of water and additionally from the landing sites of the ice shrapnel (third frame). For clarity, the advancing frost fronts are outlined in orange. (**b,c**) To determine the dependence of pattern geometry and the time of freezing onset on the rate of frost growth, the thin film of supercooled water was intentionally frozen either 0, 30, 60, 90, 120, or 270 s after reaching a steady-state temperature of $T_s = -10\,°C$. As expected, frost was able to grow more quickly across the C2P array of condensation compared to C4P due to the closer packing of the supercooled condensation. However, the rate of frost growth did not exhibit any clear dependence upon the time of condensation growth prior to freezing, due to the highly random interference of the ice shrapnel.

B.5 Frost Propagation
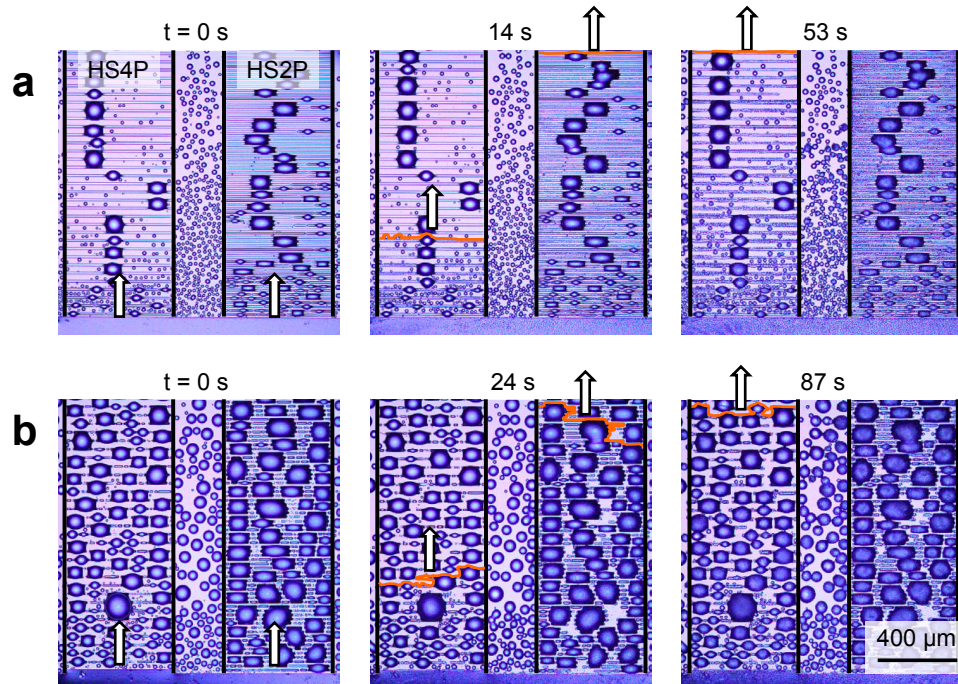
FIGURE B.9: Growth of inter-droplet frost across horizontal stripes of water (HS4P on left and HS2P on right). The ambient conditions were $T_\infty = 24.0\,°C$ and $H = 26\,\%$, such that the ice shrapnel effect was suppressed and all frost growth originated from the frozen pad of water (bottom of screen). Freezing was initiated either (**a**) 1 min or (**b**) 5 min after reaching a steady-state temperature of $T_s = -10\,°C$ by touching ice to the film of water bordering the stripe arrays. Unlike with the circle or triangle arrays (cf. Fig. 7), the average rate of frost growth did not increase at later freezing times. This is attributed to the growing bulges of water partially drying out the water along the stripes with increasing growth time. In other words, the increased ease of inter-droplet ice bridging along the larger bulges of water is cancelled out by an inhibited growth of ice across the stripes of water.
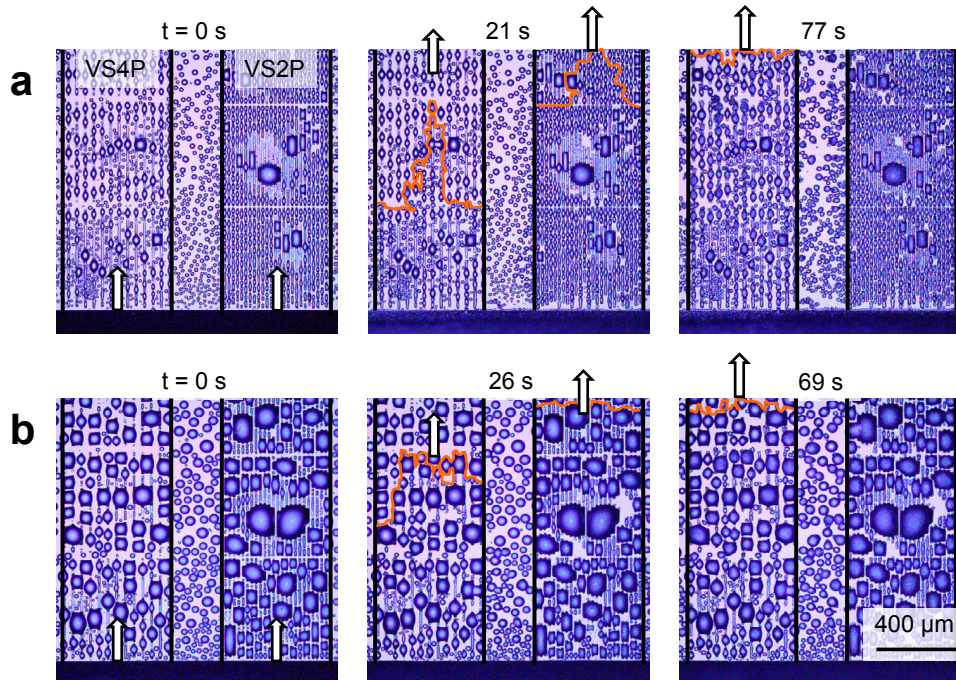
FIGURE B.10: Frost growth across vertical stripes of water (VS4P on left and VS2P on right) under the same experimental conditions as detailed in Supplementary Fig. S9. Note that the vertical stripes of water were somewhat discontinuous, potentially due to minor surface contamination. These discontinuities prevent the ice from directly propagating across the lines; instead, inter-droplet ice bridges had to connect across the gaps. Similar to what was observed with the horizontal stripes, the rate of frost growth was not significantly different for freezing initiated at (**a**) 1 min compared to (**b**) 5 min.
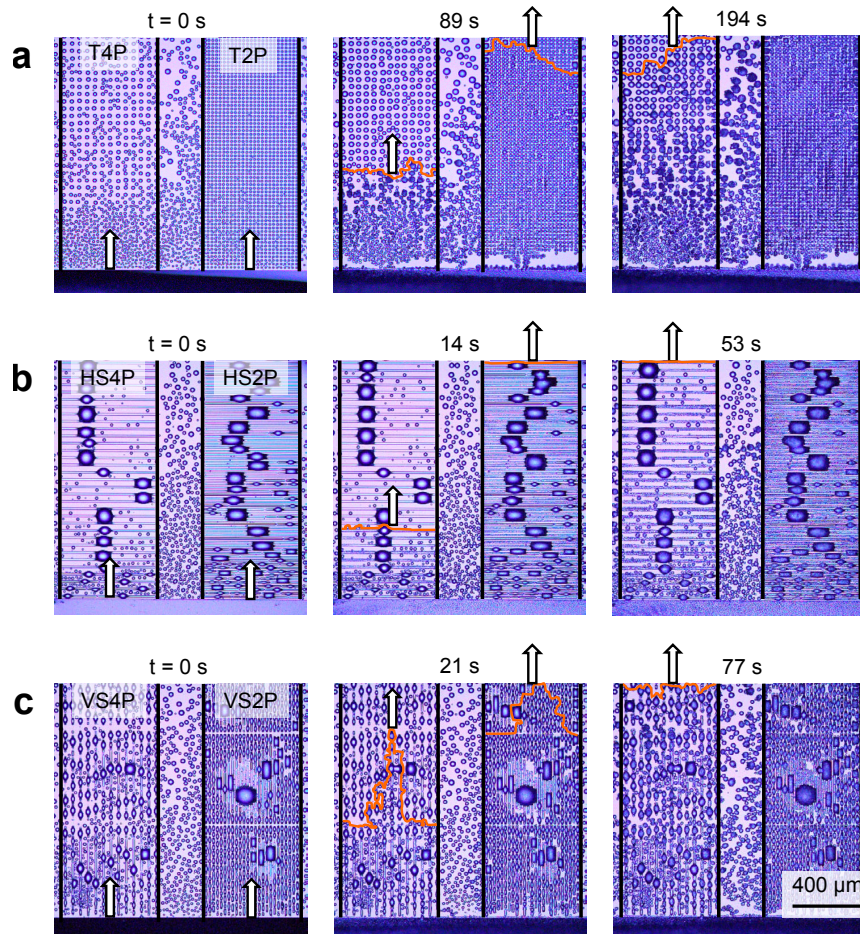
FIGURE B.11: A direct visual comparison of inter-droplet frost growth across (**a**) triangle arrays, (**b**) horizontal stripes, and (**c**) vertical stripes. Note that these figures were taken from Fig. 6a, Supplementary Fig. 9a, and Supplementary Fig. S10a, respectively. When the time of initial freezing is 1 min after reaching $T_s = -10\,^{\circ}\mathrm{C}$, the rate of frost growth was higher across the stripes by a factor of 3 compared to the discontinuous triangles. This is attributed to two primary factors: fewer inter-droplet ice bridges are required for the continuous stripe patterns, and the stripes exhibit a plateau surface coverage of water much faster than the triangles (cf. Figs. 2, 3).

B.6 Dry Zone Formation and Failure
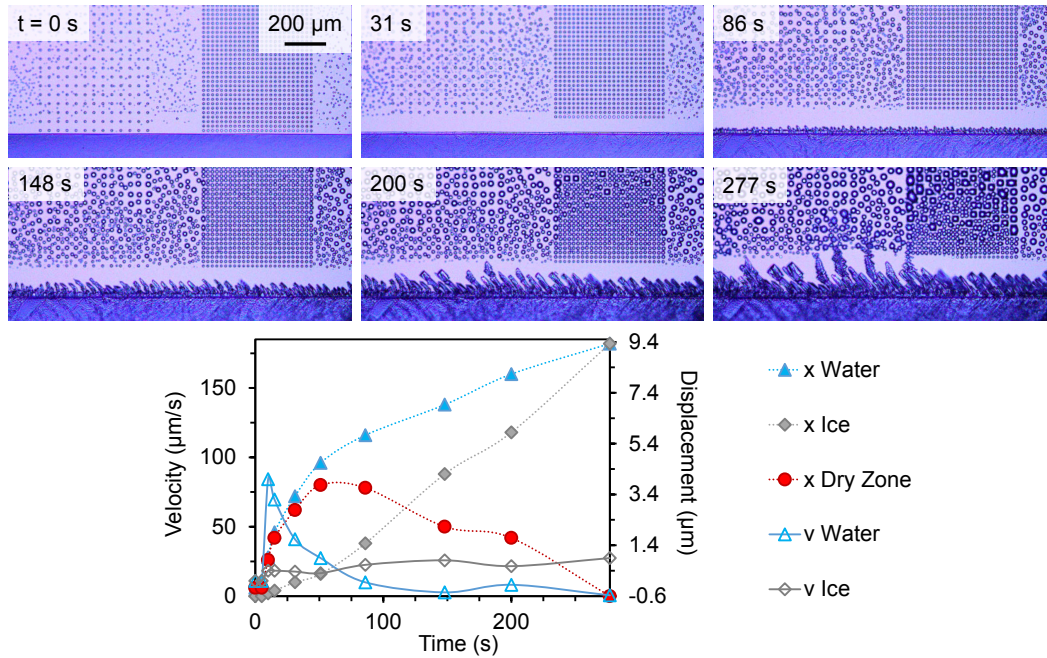
FIGURE B.12: Formation of a dry zone between a film of frozen water and arrays of supercooled condensate on triangular patterns. The film of water (bottom of screen) was frozen immediately after reaching $T_s = -10\,°C$ (1st frame) under ambient conditions of $T_\infty = 24.0\,°C$ and $H = 26\,\%$. Initially, the first eight rows of patterned condensate completely evaporated due to the vapor pressure gradient between the ice and water. However, eventually the growing frost was able to bridge all the way across the dry zone, resulting in the propagation of frost across the surface (last frame). Note that the shape of the advancing frost front has a finger-like geometry, due to the discontinuous pattern of liquid condensate being harvested. The positions and velocities of the receding water (triangles) and advancing frost (diamonds) are plotted as a function of time, where each data point corresponds to the complete evaporation of the next row of patterned condensate. The final data point corresponds to when the dry zone (circles) has completely collapsed due to ice bridging.
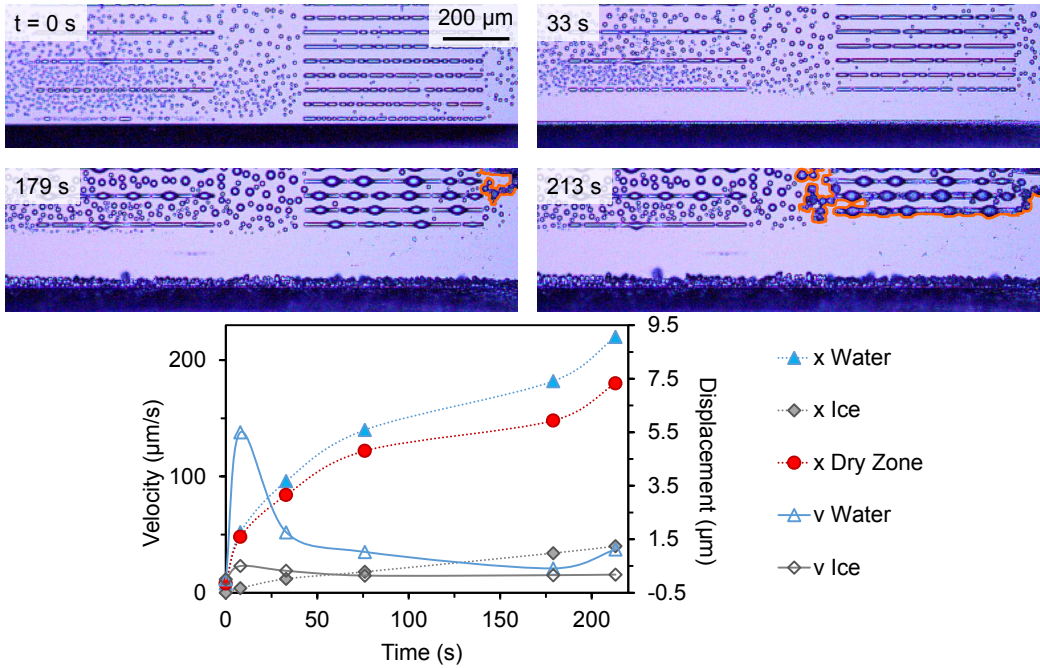
FIGURE B.13: Formation of a dry zone between ice and horizontal stripes of supercooled condensate. Except for the different geometry of the patterned water, the experimental conditions and protocol are identical to those described in Supplemental Fig. 12. Note that the frost advancing into the dry zone is extremely uniform in its profile, owing to the stripes of harvested water running parallel to the ice. Each data point in the graph represents the next stripe of water having evaporated completely due to the water harvesting of the ice. The dry zone was extremely stable for several minutes; in fact, the remaining stripes of supercooled water only froze due to the invasion of frost from elsewhere on the surface (final frame, frost invasion outlined in orange).

Appendix C

Dry Zones

C.1 Methods and Materials

Hydrophobic Silicon Surface: A silicon wafer with $100\,\mathrm{nm}$ of SiO_2 was cleaned with oxygen plasma for 4 min at $150\,\mathrm{W}$ (Plasma Etch, PE-25). Silane deposition was performed by placing the silicon wafer inside of a Pyrex pan with $20\,\mu L$ of trichloro(1H, 1H, 2H, 2H - perfluorooctyl) (Sigma Aldrich). The pan was subsequently heated on a hot plate at $70\,^\circ\mathrm{C}$ for two hours to facilitate the vapor-phase deposition of a self-assembled silane monolayer on the silicon. The advancing and receding contact angles were measured to be $\theta_A/\theta_R = 94°/77°$ using a contact angle goniometer (ramé-hart, Model 590), with an uncertainty of $\pm 1°$.

Humidity Chamber Experiments: For each experiment (corresponding to Figure 2a,b) the hydrophobic silicon chip was bonded, using thermal paste, to a Peltier stage inside a customized humidity chamber (ramé-hart) that was bolted underneath a top-down optical microscope (Nikon LV150). A quartz window was embedded in the chamber's roof to facilitate sample imaging with a 5, 10, or $20\times$ long working-distance lens (Mitutoyo). The vertical gap between the sample and the bottom of the quartz window was $2.2\,\mathrm{cm}$ to avoid disruption of the diffusive boundary layer that resulted during condensation.

The ambient humidity was set to a pre-determined amount, such that the substrate temperature was just above the dew point. For example, for a testing humidity of 21% and air temperature of 21°C, the Peltier stage was set to $-2\,^\circ\mathrm{C}$. When the surface was completely dry, the chamber was opened and a $10\mu L$ droplet of distilled water was deposited on the center of the silicon chip as quickly as possible. The chamber was then closed and allowed to equilibrate to the testing humidity so that

any surrounding condensation evaporated. The surface was then brought down to $-20\,°C$ in order to freeze the deposited droplet. If condensation ensued during or after the freezing of the droplet, the surface temperature was either brought above the dew point (but still below $0\,°C$ because of low humidity in the chamber) or the humidity in the chamber was further decreased to ensure evaporation of the condensate. Once the surface around the frozen droplet was completely dry, the Peltier stage and ambient humidity were set to their desired values.

A top-down video of a dry zone around the frozen droplet was recorded at 10 frames per second with a digital camera (Phantom v711). The length in pixels from the edge of the frozen drop to the perimeter of the dry zone were measured in four different places around the droplet (top, bottom, left, and right) once it appeared that the dry zone had stabilized at a steady-state value, and these four measurements were averaged for each trial. Three such trials were conducted and averaged together to obtain the value of the dry zone length for each surface temperature, ranging from $-2.5\,°C$ to $-30\,°C$ in intervals of $-2.5\,°C$. This process was repeated for four different humidity values: 50%, 21%, 10% and $4 \pm 1\%$. The average contact line radius of the frozen droplet was 1.7 ± 0.3mm. The average air temperature inside of the humidity chamber during steady-state conditions was $16 \pm 2\,°C$, due to the Peltier stage slightly cooling the air inside.

Ambient Experiments: For each experiment (corresponding to Figure 2c,d) a distilled water droplet that was either 1, 10, or $100\,\mu L$ in volume was deposited on a hydrophobic silicon chip and placed in a dry freezer. Once the droplet was frozen, the silicon chip was quickly transferred to a nearby Peltier stage (Linkam, PE120) that was preset to the testing temperature and pre-positioned under the microscope stage. Unlike the humidity chamber experiments, these experiments were conducted in the ambient laboratory environment with a relative humidity of $68 \pm 5\%$ and air temperature of $21.0 \pm 1.5\,°C$.

Measurements of the dry zones were performed in the same way described in the above section for each surface temperature. Instead of varying the humidity in addition to the surface temperature, it was the droplet volume that was varied to determine the size effect of the hygroscopic ice. Because of minor evaporation effects when the droplets were in the freezer, the final volumes of the ice droplets were slightly smaller than the initial volumes of 1, 10, or $100\,\mu L$. To account for this, the average contact line radius of the frozen droplets were measured under the microscope to be $0.76 \pm .03$ mm, $1.75 \pm .02$ mm and 4.12 ± 0.08 mm respectively. Using a side-view camera, the contact angle of each ice droplet was measured to be approximately $90\,°$, such that its contact radius is approximately equal to its radius of curvature.

Nucleation Experiments: The hydrophobic silicon wafer was bonded onto a Peltier stage inside the humidity chamber (ramé-hart). Keeping the humidity fixed at $H = 10.3 \pm 0.4\%$ and the air temperature at $T_\infty = 15.7 \pm 0.1$°C, the surface temperature was incrementally cooled until the nucleation and growth of condensate occurred at a

critical temperature. This process was performed on three equivalently treated silicon chips, with three trials performed for each sample. The critical surface temperatures for nucleation to occur was $-18.3 \pm 1.2°$C, $-19.4 \pm 1.4°$C, and $-17.3 \pm 0.9°$C for the three respective surfaces. This yields an SSD ranging from 0.03–0.23, with the average being 0.13 ± 0.10, where SSD is defined as $(c_N - c_w)/c_w$ and the uncertainty corresponds to a standard deviation.

In order to obtain the (receding) intrinsic contact angle θ_r for a nucleating embryo, we use classical nucleation theory to relate our experimentally determined nucleation pressure p_N to the θ_r (Ref. 11 from manuscript):

$$p_N = p_w \, \exp\left(\frac{v}{RT_w}\sqrt{\frac{4\pi}{3}\frac{\sigma^3}{kT_w \, \ln\left(\frac{I_0}{I_c}\right)}\left(2 + \cos\theta_r\right)\left(1 - \cos\theta_r\right)^2}\right), \tag{C.1}$$

where σ is the surface energy per unit area of water with respect to vapor, k is the Boltzmann constant, $I_0 \sim 10^{29}\,\mathrm{m^{-2}s^{-1}}$ is the kinetic constant of nucleation and $I_c \sim 10^4\,\mathrm{m^{-2}s^{-1}}$ is the critical embryo formation rate for nucleation to occur. Plugging in our experimentally measured values of p_N, we solve Equation S1 for θ_r to obtain an effective surface wettability of $\theta_r = 33 \pm 5°$ at the nucleation sites. While this is much lower than the surface's global receding contact angle for macroscopic droplets, it is well known that nucleation occurs at local defects that can exhibit significantly lower nucleation energy barriers.

C.2 Pathways to the Dry Zone
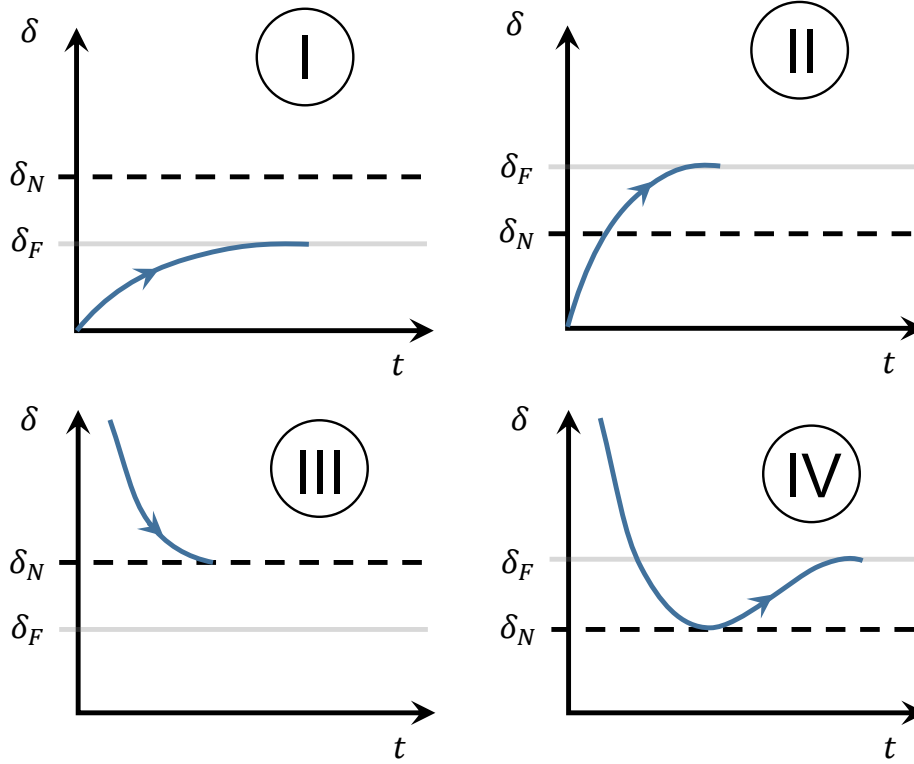
FIGURE C.1: There are two ways of performing the dry zone experiment: by evaporating out the surrounding condensate (Cases I and II) or by growing in the condensation toward the frozen droplet (Cases III and IV). In both cases the condensation stops at a dry zone threshold, δ_{Cr}. However, for cases I and II, the emerging dry zone is necessarily a flux dry zone, that is $\delta_{Cr} = \delta_F$, as there are pre-existing droplets inside the nucleation dry zone, δ_N which are subsequently *evaporated out*. On the other hand, when condensation is grown in, droplets are *nucleating* on a previously dry region. Therefore, δ would first reach δ_N and would stop if $\delta_N > \delta_F$, because the nucleated droplets are free to grow. However, if this $\delta_N < \delta_F$, then the droplets in the region between δ_F and δ_N would evaporate and thus the emergent dry zone would be δ_F (Case IV). The above discussion shows that only by doing experiments with an initially dry environment, that is $\delta \to \infty$, can we experimentally determine which one of the two dry zones wins.

C.3   Comparison between δ_N and δ_F for Constant Humidity
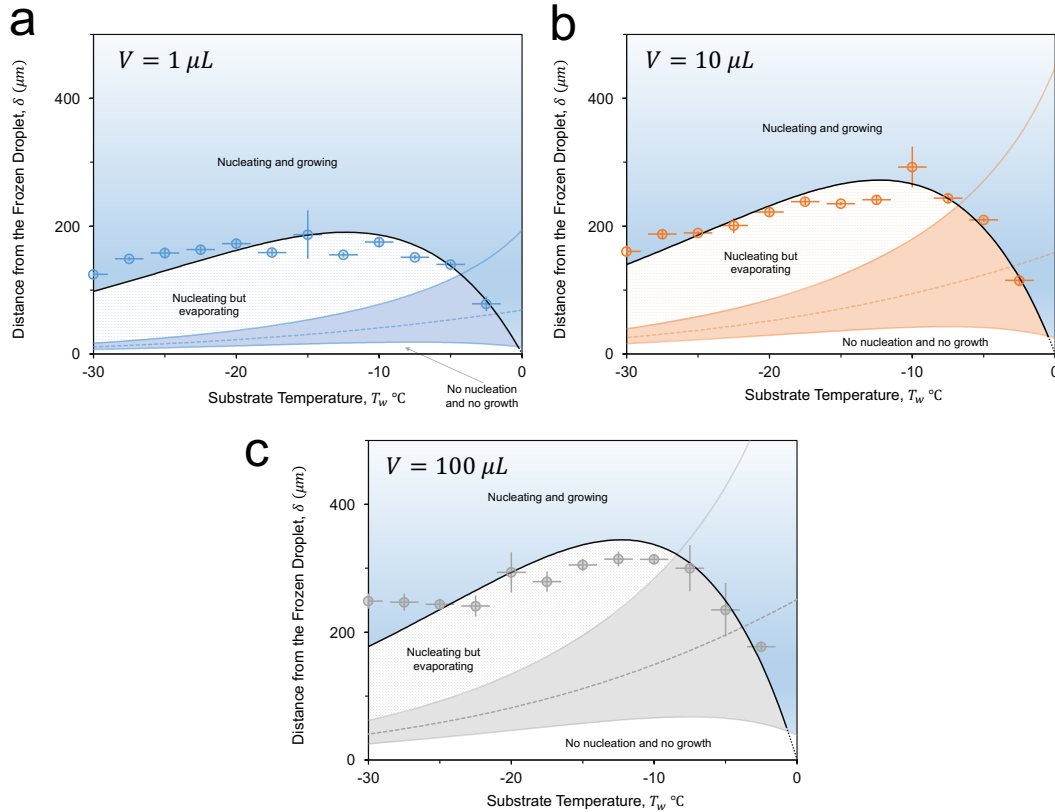
FIGURE C.2: Ambient Experiments: a-c) The blue, orange and gray solid lines denote the upper and lower bound of the nucleation dry zones around frozen droplets of volumes $V = 1$, 10, and $100\,\mu$L at a fixed humidity of $H = 68 \pm 5\%$ and $T_\infty = 21.0 \pm 1.5°$C. The two bounds of the nucleation dry zone are estimated taking into account the variations in c_∞ and SSD of the substrate. The black solid line denotes the flux dry zone. The nucleation dry zone curves do not capture the emergent dry zones quantitatively or qualitatively. Below the lower bound of the nucleation dry zone, no nucleation is possible. Above the nucleation dry zone, but below the flux dry zone is a region where droplets can nucleate but not survive, due to a net evaporative flux toward the humidity sink. Finally, beyond the flux the dry zone, droplets are free to grow. Note that even within the range of uncertainty of the nucleation dry zone, the critical dry zone always finds the flux line and settles there at steady state.

C.4 Comparison between δ_N and δ_F for Constant Volume
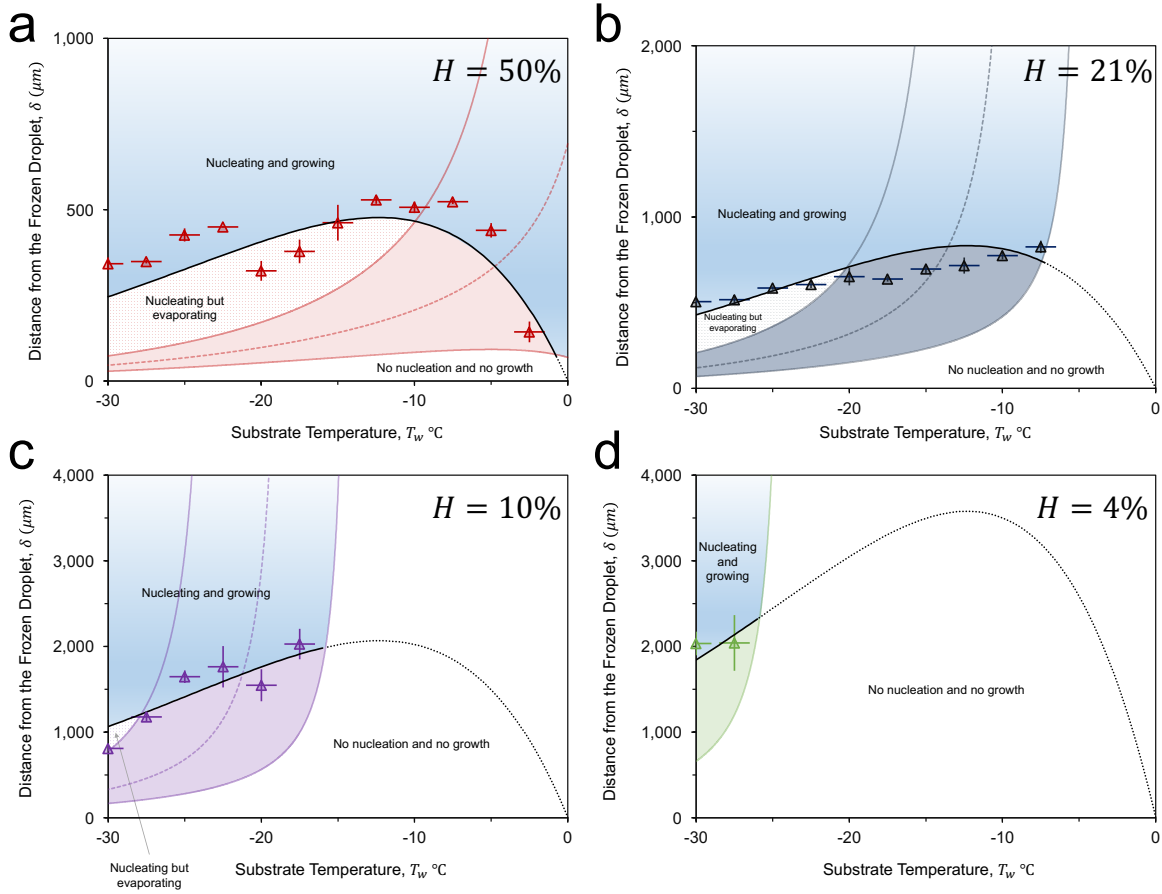
FIGURE C.3: Humidity Chamber Experiments: a-d) The light red, dark blue, purple and green solid lines denote the upper and lower bound of the nucleation dry zones around frozen droplets of a fixed volume of $V = 10 \, \mu L$ but different humidities $H = 50\%$, 21%, 10% and $4 \pm 1\%$. The black solid line denotes the flux dry zone. The data points follow the flux lines and are finally terminated by the lower bound of the nucleation dry zones. As in the previous figure, we find that the nucleation dry zones cannot capture the nature or the values of the $\delta - T_w$ plot.

C.5   Numerical Modeling

Here we present complementary computational results that further substantiate our findings and corroborate our scaling law, $\delta_F \sim RPe^{-1}S^{*-1}$, derived in the main text. Since the diffusion coefficient of water vapor is constant, the steady-state concentration is governed by the following Laplace equation, $\nabla^2 c = 0$, where c is the water vapor concentration. To make the problem tractable, we approximate the layer of condensed water droplets on the solid substrate as a thin water film. The ice droplet is further assumed to be hemispherical. Thus the problem is axisymmetric and can be solved in a 2D computational domain. We impose Dirichlet conditions $c = c_\infty$, $c = c_i$, and $c = c_w$ on the upper boundary, ice surface, and the water film, respectively; no-flux condition is imposed on the rest of the boundary.

Here c_∞ is the ambient vapor concentration while c_i and c_w are the saturation vapor concentrations of ice and water, respectively. In order to capture the dry zone length, we vary the inner edge of the water film systematically until it coincides with the stagnation point of the diffusion flux. For each different water film The Laplace equation is solved by a finite element method using the COMSOL Multiphysics software. To ensure numerical accuracy, the computational mesh in refined in a small region above the dry zone and the finest element size is typically 10^{-3} ice radius and the computational domain was taken to be $10\,\mathrm{mm} \times 5\,\mathrm{mm}$. Figure SC.4a and b shows how the existence of an adjacent condensate (shown in dark gray) changes the concentration field around ice droplet. Figure SC.4c shows how the size effect of the frozen droplet on the dry zone. The numerical δ is not necessarily an exact quantitative match with the experimentally measured δ, but it accurately captures the functional dependencies of the scaling trend. This can be seen in Figure C.4d where the numerical results corresponding to different humidities in our experiments follow the scaling law $\delta_F \sim RPe^{-1}S^{*-1}$.
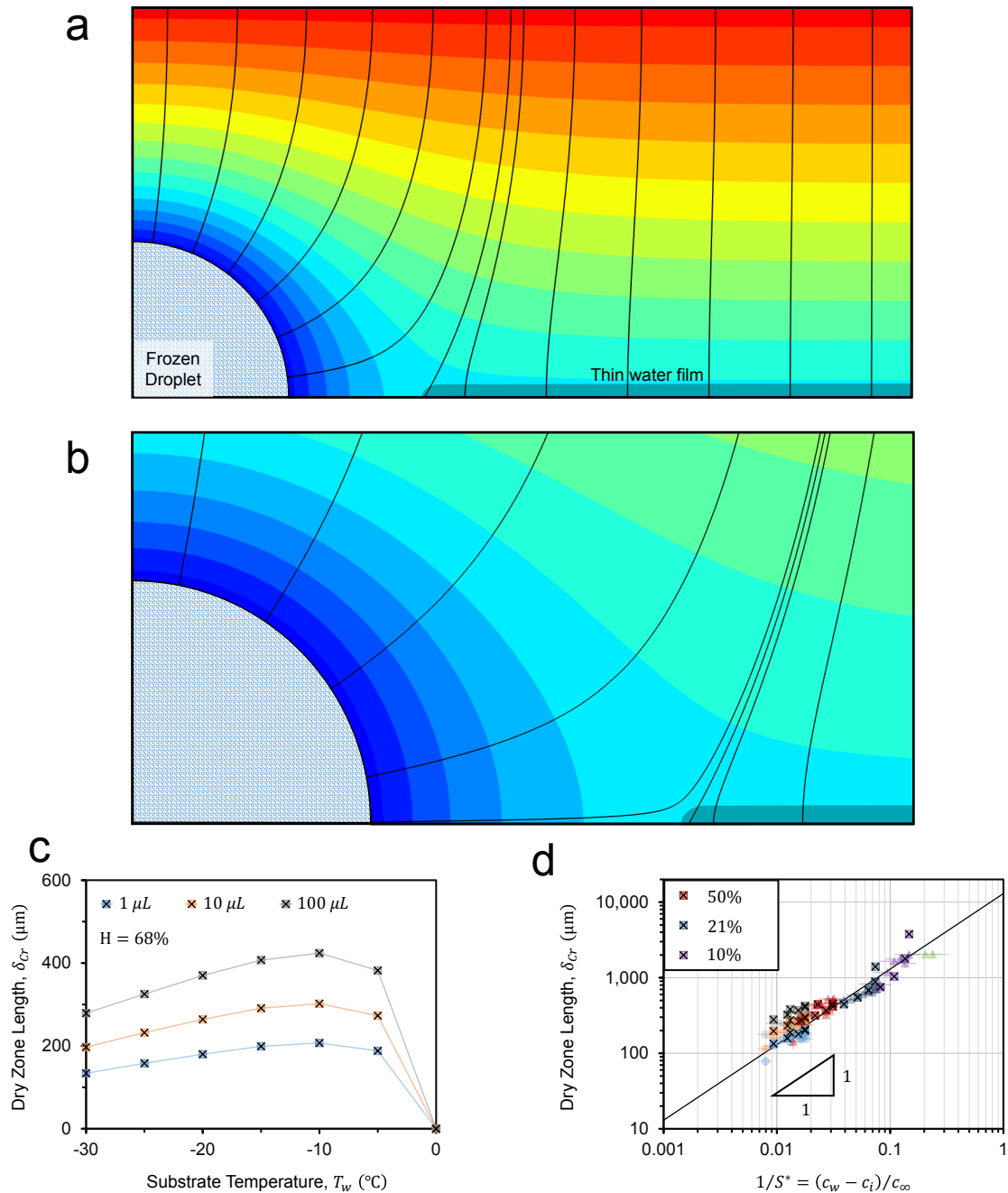
FIGURE C.4: a) Concentration field around a frozen droplet. The supercooled liquid condensate approximated as a thin water film (dark gray region to the right of the frozen droplet). The black curves correspond to the pathlines of vaporr flowing vertically downward. b) Zoomed in version of the dry region shows how vapor flows from the edge of the thin film toward the frozen droplet. c) Numerical results of dry zones around frozen droplets of 1, 10 and 100 μL corresponding an ambient humidity of $H = 68\%$ shows the lager the size of the droplets, the larger the dry zone (as seen in Figure 2b of main text). Also, note the $\delta - T_w$ curves closely follow the variation of $(c_w - c_i)$ with temperature. c) Numerically obtained δ for different humidities fall on the experimentally observed scaling law $\delta_F \sim RPe^{-1}S^{*-1}$.

116

C.6 Comparison between δ_N and δ_F for Constant Temperatures, $-30 \leq T_w < 0°\text{C}$
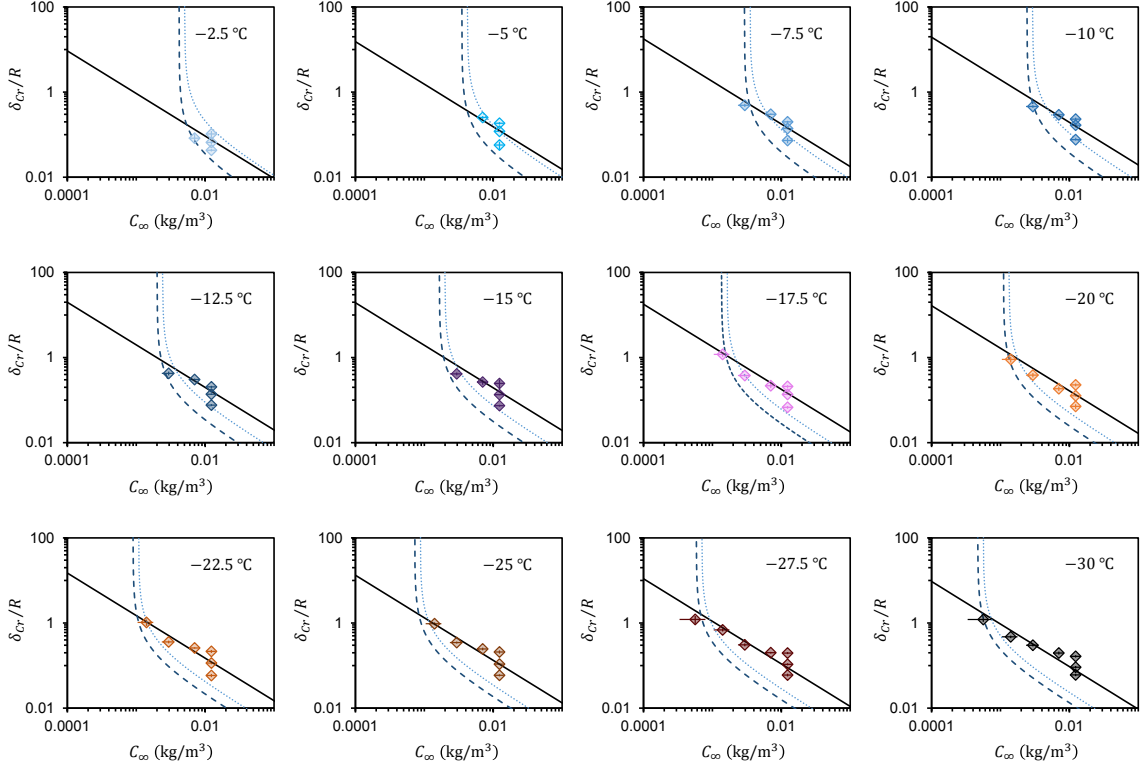
FIGURE C.5: Phase map of nucleation and flux dry zones at different surface temperatures, $-30 \leq T_w < 0°\text{C}$, at 2.5°C intervals. The dashed lines correspond to nucleation dry zone, δ_N at a fixed temperature (dark blue for $SSD = 0.03$, light blue for $SSD = 0.23$). The solid line corresponds to the flux dry zone, δ_F at constant temperature. The critical dry zone, δ_{Cr} should correspond to the greater of the two dry zones. As evident from the figures, the dry zone always follows the flux dry zone line. As c_∞ approaches the critical nucleation concentration c_N, δ_N asymptotes sharply. This is why it is experimentally extremely difficult to obtain data points on the asymptotic region of the dashed line. Experiments at $c_\infty \to c_N$, yielded either $\delta_{Cr} \to \infty$ (when erring on the lower side of nucleation concentration) or $\delta_{Cr} = \delta_F$ (when erring on the higher side of nucleation concentration).

C.7 The Breathing of the Dry Zone
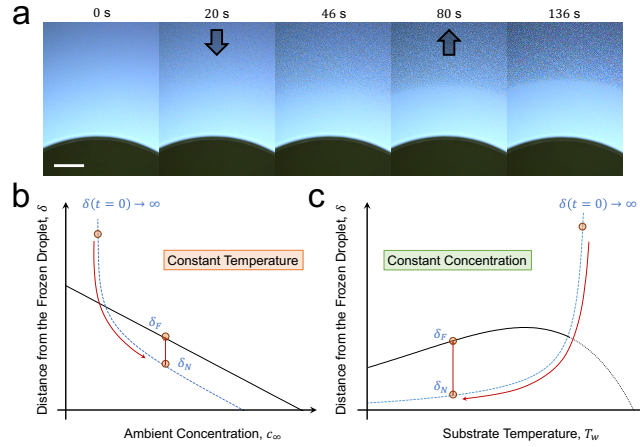
FIGURE C.6: Ambient Experiments: a) Condensation grows radially inward toward the frozen droplet and then subsequently evaporates out to settle at the flux dry zone. The steady state dry zone in the figure corresponds to a frozen droplet of volume $V = 10\,\mu L$, at a substrate temperature $T_w = -12.5°C$, air temperature $T_\infty = 14.9°C$ and humidity of $H = 21\%$. Scale bar denotes $100\,\mu m$ b) Schematic of how δ evolves over time when substrate temperature is kept constant and c_∞ is gradually increased. The dotted blue line corresponds to an isothermal nucleation dry zone line, δ_N and the black solid line represents an isothermal flux dry zone, δ_F. As c_∞ is increased, δ initially moves along the dotted blue line till the c_∞ is set at a particular value. This sets $\delta = \delta_N$, but δ_N being below δ_F, the nucleated droplets cannot survive and evaporate out to the distance δ_F. c) Schematic of how δ evolves over time when c_∞ is held constant and T_w is decreased from the dew point to the desired value. Initially δ follows the iso-concentration δ_N curve, but once the T_w is held constant, it moves to δ_F. Both pathways lead to initial condensation up to δ_N and subsequent evaporation to δ_F. The droplets that nucleate and evaporate out are not expected to be visible under an optical microscope as nucleating embryos are typically 1-10 nm in size. Nevertheless, the evaporation were sometimes visible in our experiments, as the droplets that nucleated close to δ_F transiently grew to micrometric sizes. This is because the rows of nanometric droplets close to δ_N interact with the frozen droplet first and evaporate out, thus shielding the droplets behind them and allowing them to grow. This results in a micrometric 'breathing of the dry zone', as seen in a).

Bibliography

[1] T. M. Schutzius, S. Jung, T. Maitra, P. Eberle, C. Antonini, C. Stamatopoulos, D. Poulikakos, Physics of icing and rational design of surfaces with extraordinary icephobicity, Langmuir 31 (17) (2015) 4807–4821.

[2] S. Jung, M. K. Tiwari, N. V. Doan, D. Poulikakos, Mechanism of supercooled droplet freezing on surfaces, Nat. Commun. 3 (2012) 615.

[3] O. R. Enriquez, A. G. Marin, K. G. Winkels, J. H. Snoeijer, Freezing singularities in water drops, Phys. Fluids 24 (9) (2012) 091102.

[4] S. Jung, M. K. Tiwari, D. Poulikakos, Frost halos from supercooled water droplets, Proc. Natl. Acad. Sci. U.S.A. 109 (2012) 16073–16078.

[5] J. B. Dooley, Determination and characterization of ice propagation mechanisms on surfaces undergoing dropwise condensation, Ph.D. thesis, Texas A & M (2010).

[6] J. B. Boreyko, C. P. Collier, Delayed frost growth on jumping-drop superhydrophobic surfaces, ACS Nano 7 (2013) 1618–1627.

[7] B. Na, R. L. Webb, A fundamental understanding of factors affecting frost nucleation, Int. J. Heat Mass Transfer 46 (2003) 3797–3808.

[8] M. G. Medici, A. Mongruel, L. Royon, D. Beysens, Edge effects on water droplet condensation, Phys. Rev. E 90 (2014) 062403.

[9] J. Guadarrama-Cetina, A. Mongruel, W. Gonzalez-Vinas, D. Beysens, Frost formation with salt, Europhys. Lett. 110 (2015) 56002.

[10] X. Sun, V. G. Damle, A. Uppal, R. Linder, S. Chandrashekar, A. R. Mohan, K. Rykaczewski, Inhibition of condensation frosting by arrays of hygroscopic antifreeze drops, Langmuir 31 (2015) 13743–13752.

[11] C. T. Sanders, The influence of frost formation and defrosting on the performance of air coolers, Ph.D. thesis, Delft University of Technology (1974).

[12] N. H. Fletcher, Physics of Rain Clouds, Cambridge University Press, Cambridge, UK, 1962.

[13] R. O. Piucco, C. J. L. Hermes, C. Melo, J. R. Barbosa, A study of frost nucleation on flat surfaces, Exp. Therm. Fluid Sci. 32 (8) (2008) 1710–1715.

[14] S. Nath, S. F. Ahmadi, J. B. Boreyko, A review of condensation frosting, Nanosc. Microsc. Therm. 21 (2017) 81–101.

[15] J. Barnes, Complete works of Aristotle, Volume 1: The revised Oxford translation, Vol. 1, Princeton University Press, 2014.

[16] N. H. Fletcher, The Chemical Physics of Ice, Cambridge University Press, Cambridge, UK, 1970.

[17] L. Boschiero, Experiment and natural philosophy in seventeenth-century Tuscany: The history of the Accademia del Cimento, Vol. 21, Springer Science & Business Media, 2007.

[18] A. M. Meirmanov, The Stefan Problem, Vol. 3, Walter de Gruyter, 1992.

[19] P. V. Hobbs, Ice Physics, Clarendon Press, Oxford, England, 1974.

[20] D. M. Murphy, T. Koop, Review of the vapour pressures of ice and supercooled water for atsmopheric applications, Q. J. R. Meteorol. Soc. 131 (2005) 1539–1565.

[21] T. Koop, Homogeneous ice nucleation in water and aqueous solutions, Z. Phys. Chem. 218 (11/2004) (2004) 1231–1258.

[22] H. R. Pruppacher, J. D. Klett, K. P. Wang, Microphysics of Clouds and Precipitation, Taylor & Francis, 1998.

[23] N. H. Fletcher, Structural aspects of the ice-water system, Rep. Prog. Phys. 34 (3) (1971) 913–994.

[24] J. G. Dash, A. W. Rempel, J. S. Wettlaufer, The physics of premelted ice and its geophysical consequences, Rev. Mod. Phys. 78 (3) (2006) 695–741.

[25] K. G. Libbrecht, The physics of snow crystals, Rep. Prog. Phys. 68 (4) (2005) 855–895.

[26] D. M. Anderson, N. R. Morgenstern, Physics, chemistry, and mechanics of frozen ground: a review, in: Permafrost: The North American Contribution to the Second International Conference, National Academy of Sciences, Washington, DC, 1973, pp. 257–288.

[27] H. G. Goff, 65 years of ice cream science, Int. Dairy J. 18 (7) (2008) 754–758.

[28] W. F. Budd, T. H. Jacka, A review of ice rheology for ice sheet modelling, Cold Reg. Sci. Technol. 16 (2) (1989) 107–144.

[29] E. M. Schulson, P. Duval, Creep and Fracture of Ice, Vol. 432, Cambridge University Press Cambridge, 2009.

[30] D. N. Thomas, G. S. Dieckmann, Sea Ice: an Introduction to its Physics, Chemistry, Biology and Geology, John Wiley & Sons, 2008.

[31] K. E. Zachariassen, E. Kristiansen, Ice nucleation and antinucleation in nature, Cryobiology 41 (4) (2000) 257–279.

[32] G. J. Morris, E. Acton, Controlled ice nucleation in cryopreservation–a review, Cryobiology 66 (2) (2013) 85–92.

[33] K. Sobolev, M. Nosonovsky, T. Krupenkin, I. Flores-Vivian, S. Rao, M. Kozhukhova, V. Hejazi, S. Muzenski, B. Bosch, R. Rivero, Anti-icing and de-icing superhydrophobic concrete to improve the safety on critical elements on roadway pavements (no. cfire 07-03), **2013**.

[34] S. Frankenstein, A. M. Tuthill, Ice adhesion to locks and dams: past work; future directions?, J. Cold Reg. Eng. 16 (2) (2002) 83–96.

[35] R. W. Gent, N. P. Dart, J. T. Cansdale, Aircraft icing, Phil. Trans. R. Soc. A. 358 (1776) (2000) 2873–2911.

[36] Y. Cao, Z. Wu, Y. Su, Z. Xu, Aircraft flight characteristics in icing conditions, Prog. Aerosp. Sci 74 (2015) 62–80.

[37] W. S. Pike, Extreme warm frontal icing on 25 february 1994 causes an aircraft accident near uttoxeter, Meteor. Appl. 2 (3) (1995) 273–279.

[38] J. Marwitz, M. Politovich, B. Bernstein, F. Ralph, P. Neiman, R. Ashenden, J. Bresch, Meteorological conditions associated with the atr72 aircraft accident near roselawn, indiana, on 31 october 1994, B. Am. Meteorol. Soc. 78 (1) (1997) 41–52.

[39] J. Lv, Y. Song, L. Jiang, J. Wang, Bio-inspired strategies for anti-icing, ACS Nano 8 (4) (2014) 3152–3169.

[40] C. C. Ryerson, T. Gilligan, G. Koenig, Evaluation of three helicopter preflight deicing techniques, in: AIAA, 1999, pp. 11–14.

[41] C. C. Ryerson, Ice protection of offshore platforms, Cold Reg. Sci. Technol. 65 (2011) 97–110.

[42] C. C. Ryerson, Assessment of superstructure ice protection as applied to offshore oil operations safety, U. S. Cold Res. Eng. Lab. (ERDC-CRREL) (2009) TR–09–4, 342 pp.

[43] S. B. Subramanyam, K. Rykaczewski, K. K. Varanasi, Ice adhesion on lubricant-impregnated textured surfaces, Langmuir 29 (2013) 13414–13418.

[44] A. K. Andersson, L. Chapman, The impact of climate change on winter road maintenance and traffic accidents in west midlands, uk, Accident Anal. Prev. 43 (1) (2011) 284–289.

[45] J. Andrey, R. Olley, The relationship between weather and road safety: past and future research directions, Climatological Bulletin 24 (3) (1990) 123–127.

[46] A. F. Emery, B. L. Siegel, Experimental measurements of the effects of frost formation on heat exchanger performance, ASME HTD 139 (1990) 1–7.

[47] L. Huang, Z. Liu, Y. Liu, Y. Gou, J. Wang, Experimental study on frost release on fin-and-tube heat exchangers by use of a novel anti-frosting paint, Exp. Therm. Fluid Sci. 33 (7) (2009) 1049–1054.

[48] M. Farzaneh, Atmospheric icing of power networks, Springer Science & Business Media, 2008.

[49] K. Ji, X. Rui, L. Li, A. Leblond, G. McClure, A novel ice-shedding model for overhead power line conductors with the consideration of adhesive/cohesive forces, Comput. Struct. 157 (2015) 153–164.

[50] L. Guo, L. Zhou, M. Chen, W. Huang, Online catenary anti-icing technique for electric railways employing direct feeding systems, IET Gener. Transm. Dis. 10 (8) (2016) 1969–1975.

[51] G. Fortin, J. Perron, Wind turbine icing and de-icing, in: 47th AIAA, 2009.

[52] O. Parent, A. Ilinca, Anti-icing and de-icing techniques for wind turbines: Critical review, Cold Reg. Sci. Technol. 65 (1) (2011) 88–96.

[53] K. Li, S. Xu, W. Shi, M. He, H. Li, S. Li, X. Zhou, J. Wang, Y. Song, Investigating the effects of solid surfaces on ice nucleation, Langmuir 28 (2012) 10749–10754.

[54] H. Wang, L. Tang, X. Wu, W. Dai, Y. Qiu, Fabrication and anti-frosting performance of super hydrophobic coating based on modified nano-sized calcium carbonate and ordinary polyacrylate, Appl. Surf. Sci. 253 (2007) 8818–8824.

[55] M. He, J. Wang, H. Li, Y. Song, Super-hydrophobic surfaces to condensed micro-droplets at temperatures below the freezing point retard ice/frost formation, Soft Matter 7 (2011) 3993–4000.

[56] Q. Zhang, M. He, X. Zeng, K. Li, D. Cui, J. Chen, J. Wang, Y. Song, L. Jiang, Condensation mode determines the freezing of condensed water on solid surfaces, Soft Matter 8 (2012) 8285–8288.

[57] J. Guadarrama-Cetina, A. Mongruel, W. Gonzalez-Vinas, D. Beysens, Percolation-induced frost formation, Europhys. Lett. 101 (2013) 16009.

[58] Q. Zhang, M. He, J. Chen, J. Wang, Y. Song, L. Jiang, Anti-icing surfaces based on enhanced self-propelled jumping of condensed water microdroplets, Chem. Commun. 49 (2013) 4516–4518.

[59] J. B. Boreyko, B. R. Srijanto, T. D. Nguyen, C. Vega, M. Fuentes-Cabrera, C. P. Collier, Dynamic defrosting on nanostructured superhydrophobic surfaces, Langmuir 29 (2013) 9516–9524.

[60] T. Jing, Y. Kim, S. Lee, D. Kim, J. Kim, W. Hwang, Frosting and defrosting on rigid superhydrohobic surface, Appl. Surf. Sci. 276 (2013) 37–42.

[61] X. Chen, R. Ma, H. Zhou, X. Zhou, L. Che, S. Yao, Z. Wang, Activating the microscale edge effect in a hierarchical surface for frosting suppression and defrosting promotion, Sci. Rep. 3 (2013) 2515.

[62] L. Boinovich, A. M. Emelyanenko, Role of water vapor desublimation in the adhesion of an iced droplet to a superhydrophobic surface, Langmuir 30 (2014) 12596–12601.

[63] J. B. Boreyko, R. R. Hansen, K. R. Murphy, S. Nath, S. T. Retterer, C. P. Collier, Controlling condensation and frost growth with chemical micropatterns, Sci. Rep. 6 (2016) 19131.

[64] A. Ghosh, S. Beaini, B. J. Zhang, R. Ganguly, C. M. Megaridis, Enhancing dropwise condensation through bioinspired wettability patterning, Langmuir 30 (2014) 13103–13115.

[65] R. Enright, N. Miljkovic, J. L. Alvarado, K. Kim, J. W. Rose, Dropwise condensation on micro-and nanostructured surfaces, Nanosc. Microsc. Therm. 18 (3) (2014) 223–250.

[66] Y. Hou, M. Yu, X. Chen, Z. Wang, S. Yao, Recurrent filmwise and dropwise condensation on a beetle mimetic surface, ACS Nano 9 (2015) 71–81.

[67] E. Olceroglu, M. McCarthy, Self-organization of microscale condensate for delayed flooding of nanostructured superhydrophobic surfaces, ACS Appl. Mater. Interfaces 8 (2016) 5729–5736.

[68] D. Attinger, C. Frankiewicz, A. R. Betz, T. M. Schutzius, R. Ganguly, A. Das, C. J. Kim, C. M. Megaridis, Surface engineering for phase change heat transfer: A review, MRS Energy Sustain. 1 (2014) 1–40.

[69] R. P. Garrod, L. G. Harris, W. C. E. Schofield, J. McGettrick, L. J. Ward, D. O. H. Teare, J. P. S. Badyal, Mimicking a stenocara beetle's back for microcondensation using plasmachemical patterned superhydrophobic–superhydrophilic surfaces, Langmuir 23 (2007) 689–693.

[70] S. C. Thickett, C. Neto, A. T. Harris, Biomimetic surface coatings for atmospheric water capture prepared by dewetting of polymer films, Adv. Mater. 23 (2011) 3718–3722.

[71] H. Bai, L. Wang, J. Ju, R. Sun, Y. Zheng, L. Jiang, Efficient water collection on integrative bioinspired surfaces with star-shaped wettability patterns, Adv. Mater. 26 (2014) 5025–5030.

[72] L. Mishchenko, M. Khan, J. Aizenberg, B. D. Hatton, Spatial control of condensation and freezing on superhydrophobic surfaces with hydrophilic patches, Adv. Funct. Mater. 23 (2013) 4577–4584.

[73] A. S. V. Dyke, D. Collard, M. M. Derby, A. R. Betz, Droplet coalescence and freezing on hydrophilic, hydrophobic, and biphilic surfaces, Appl. Phys. Lett. 107 (2015) 141602.

[74] T. M. Rogers, K. Elder, R. Desai, Droplet growth and coarsening during heterogeneous vapor condensation, Phys. Rev. A 38 (10) (1988) 5303–5309.

[75] P. L. Krapivsky, Growth of a single drop formed by diffusion and adsorption of monomers on a two-dimensional substrate, Phys. Rev. E 47 (1993) 1199–1202.
doi:10.1103/PhysRevE.47.1199.
URL http://link.aps.org/doi/10.1103/PhysRevE.47.1199

[76] A. Steyer, P. Guenoun, D. Beysens, C. M. Knobler, Growth of droplets on a substrate by diffusion and coalescence, Phys. Rev. A 44 (12) (1991) 8271–8277.

[77] D. Beysens, The formation of dew, Atmos. Res. 39 (1995) 215–237.

[78] J. L. Viovy, D. A. Beysens, C. M. Knobler, Scaling description for the growth of condensation patterns on surfaces, Phys. Rev. A 37 (1988) 4965–4970.

[79] M. Sokuler, G. K. Auernhammer, C. J. Liu, E. Bonaccurso, H. J. Butt, Dynamics of condensation and evaporation: Effect of inter-drop spacing, EPL (Europhysics Letters) 89 (3) (2010) 36004.

[80] J. Guadarrama-Cetina, R. D. Narhe, D. A. Beysens, W. Gonzalez-Vinas, Droplet pattern and condensation gradient around a humidity sink, Phys. Rev. E 89 (2014) 012402.

[81] R. A. Shaw, A. J. Durant, Y. Mi, Heterogeneous surface crystallization observed in undercooled water, J. Phys. Chem. B 109 (20) (2005) 9865–9868.

[82] N. H. J. Fletcher, Size effect in heterogeneous nucleation, J. Chem. Phys. 29 (3) (1958) 572–576.

[83] A. W. Adamson, A. P. Gast, Physical Chemistry of Surfaces (6th ed.), Wiley, 1997.

[84] P. Eberle, M. K. Tiwari, T. Maitra, D. Poulikakos, Rational nanostructuring of surfaces for extraordinary icephobicity, Nanoscale 6 (2014) 4874–4881.

[85] D. Quere, Non-sticking drops, Rep. Prog. Phys. 68 (2005) 2495–2532.

[86] L. Cao, A. K. Jones, V. K. Sikka, J. Wu, D. Gao, Anti-icing superhydrophobic coatings, Langmuir 25 (2009) 12444–12448.

[87] S. A. Kulinich, S. Farhadi, K. Nose, X. W. Du, Superhydrophobic surfaces: are they really ice-repellent?, Langmuir 27 (2011) 25–29.

[88] L. B. Boinovich, A. M. Emelyanenko, Anti-icing potential of superhydrophobic coatings, Mendeleev Commun. 23 (1) (2013) 3–10.

[89] L. Boinovich, A. M. Emelyanenko, V. V. Korolev, A. S. Pashinin, Effect of wettability on sessile drop freezing: when superhydrophobicity stimulates an extreme freezing delay, Langmuir 30 (2014) 1659–1668.

[90] M. Wen, L. Wang, M. Zhang, L. Jiang, Y. Zheng, Antifogging and icing-delay properties of composite micro-and nanostructured surfaces, ACS Appl. Mater. Interfaces 6 (6) (2014) 3963–3968.

[91] A. Alizadeh, M. Yamada, R. Li, W. Shang, S. Otta, S. Zhong, L. Ge, A. Dhinojwala, K. R. Conway, V. Bahadur, A. J. Vinciquerra, B. Stephens, M. L. Blohm, Dynamics of ice nucleation on water repellent surfaces, Langmuir 28 (2012) 3180–3186.

[92] S. Farhadi, M. Farzaneh, S. A. Kulinich, Anti-icing performance of superhydrophobic surfaces, Appl. Surf. Sci. 257 (2011) 6264–6269.

[93] P. Guo, Y. Zheng, M. Wen, C. Song, Y. Lin, L. Jiang, Icephobic/anti-icing properties of micro/nanostructured surfaces, Adv. Mater. 24 (2012) 2642–2648.

[94] S. Jung, M. Dorrestijn, D. Raps, A. Das, C. M. Megaridis, D. Poulikakos, Are superhydrophobic surfaces best for icephobicity?, Langmuir 27 (2011) 3059–3066.

[95] P. Kim, T. S. Wong, J. Alvarenga, M. J. Kreder, W. E. Adorno-Martinez, J. Aizenberg, Liquid-infused nanostructured surfaces with extreme anti-ice and anti-frost performance, ACS Nano 6 (2012) 6569–6577.

[96] K. K. Varanasi, T. Deng, J. D. Smith, M. Hsu, N. Bhate, Frost formation and ice adhesion on superhydrophobic surfaces, Appl. Phys. Lett. 97 (2010) 234102.

[97] A. J. Meuler, J. D. Smith, K. K. Varanasi, J. M. Mabry, G. H. McKinley, R. E. Cohen, Relationships between water wettability and ice adhesion, ACS Appl. Mater. Interfaces 2 (11) (2010) 3100–3110.

[98] S. B. Subramanyam, V. Kondrashov, J. Rühe, K. K. Varanasi, Low ice adhesion on nano-textured superhydrophobic surfaces under supersaturated conditions, ACS Appl. Mater. Interfaces 8 (2016) 12583âĹŠ–12587.

[99] T. Maitra, S. Jung, M. E. Giger, V. Kandrical, T. Ruesch, D. Poulikakos, Superhydrophobicity vs. ice adhesion: The quandary of robust icephobic surface design, Adv. Mater. Interfaces 2 (16) (2015) 1500330.

[100] Y. Wang, M. Li, T. Lv, Q. Wang, Q. Chen, J. Ding, Influence of different chemical modifications on the icephobic properties of superhydrophobic surfaces in a condensate environment, J. Mater. Chem. 3 (9) (2015) 4967–4975.

[101] M. J. Kreder, J. Alvarenga, P. Kim, J. Aizenberg, Design of anti-icing surfaces: smooth, textured or slippery?, Nat. Rev. Mater. 1 (2016) 15003.

[102] P. Tourkine, M. L. Merrer, D. Quere, Delayed freezing on water repellent materials, Langmuir 25 (2009) 7214–7216.

[103] Y. Zhang, X. Yu, H. Wu, J. Wu, Facile fabrication of superhydrophobic nanostructures on aluminum foils with controlled-condensation and delayed-icing effects, Appl. Surf. Sci. 258 (2012) 8253–8257.

[104] K. Rykaczewski, S. Anand, S. B. Subramanyam, K. K. Varanasi, Mechanism of frost formation on lubricant-impregnated surfaces, Langmuir 29 (2013) 5230–5238.

[105] L. Mishchenko, B. Hatton, V. Bahadur, J. A. Taylor, T. Krupenkin, J. Aizenberg, Design of ice-free nanostructured surfaces based on repulsion of impacting water droplets, ACS Nano 4 (2010) 7699–7707.

[106] T. Maitra, M. K. Tiwari, C. Antonini, P. Schoch, S. Jung, P. Eberle, D. Poulikakos, On the nanoengineering of superhydrophobic and impalement resistant surface textures below the freezing temperature, Nano Lett. 14 (2014) 172–182.

[107] T. Maitra, C. Antonini, M. K. Tiwari, A. Mularczyk, Z. Imeri, P. Schoch, D. Poulikakos, Supercooled water drops impacting superhydrophobic textures, Langmuir 30 (36) (2014) 10855–10861.

[108] H. Liu, P. Zhang, M. Liu, S. Wang, L. Jiang, Organogel-based thin films for selfcleaning on various surfaces, Adv. Mater. 25 (2013) 4477–4481.

[109] L. Yin, Q. Xia, J. Xue, S. Yang, Q. Wang, Q. Chen, *In Situ* investigation of ice formation on surfaces with representative wettability, Appl. Surf. Sci. 256 (2010) 6764–6769.

[110] G. Chaudhary, R. Li, Freezing of water droplets on solid surfaces: An experimental and numerical study, Exp. Therm. Fluid Sci. 57 (2014) 86–93.

[111] F. Aliotta, P. V. Giaquinta, R. C. Ponterio, S. Prestipino, F. Saija, G. Salvato, C. Vasi, Supercooled water escaping from metastability, Sci. Rep. 4.

[112] F. Feuillebois, A. Lasek, P. Creismeas, F. Pigeonneau, A. Szaniawski, Freezing of a subcooled liquid droplet, J. Colloid Interf. Sci. 169 (1) (1995) 90 – 102. `doi:http://dx.doi.org/10.1006/jcis.1995.1010`.
URL `http://www.sciencedirect.com/science/article/pii/S0021979785710107`

[113] S. Tabakova, F. Feuillebois, S. Radev, Freezing of a supercooled spherical droplet with mixed boundary conditions, in: Phil. Trans. R. Soc. A: Mathematical, Physical and Engineering Sciences, Vol. 466, The Royal Society, 2010, pp. 1117–1134.

[114] A. G. Marin, O. R. Enriquez, P. Brunet, P. Colinet, J. H. Snoeijer, Universality of tip singularity formation in freezing water drops, Phys. Rev. Lett. 113 (5) (2014) 054301.

[115] J. H. Snoeijer, P. Brunet, Pointy ice-drops: How water freezes into a singular shape, Am. J. Phys. 80 (9) (2012) 764–771.

[116] R. J. Cheng, Water drop freezing: ejection of microdroplets, Science 170 (1970) 1395–1396.

[117] M. He, J. Wang, H. Li, Y. Song, Super-hydrophobic surfaces to condensed micro-droplets at temperatures below the freezing point retard ice/frost formation, Soft Matter 7 (8) (2011) 3993–4000.

[118] Q. Hao, Y. Pang, Y. Zhao, J. Zhang, J. Feng, S. Yao, Mechanism of delayed frost growth on superhydrophobic surfaces with jumping condensates: more than interdrop freezing, Langmuir 30 (2014) 15416–15422.

[119] A. Kim, C. Lee, H. Kim, J. Kim, Simple approach to superhydrophobic nanostructured al for practical antifrosting application based on enhanced self-propelled jumping droplets, ACS Appl. Mater. Interfaces 7 (2015) 7206–7213.

[120] J. Petit, E. Bonaccurso, General frost growth mechanism on solid substrates with different stiffness, Langmuir 30 (2014) 1160–1168.

[121] B. Na, R. L. Webb, New model for frost growth rate, Int. J. Heat Mass Transfer 47 (2004) 925–936.

[122] B. Na, R. L. Webb, Mass transfer on and within a frost layer, Int. J. Heat Mass Transfer 47 (5) (2004) 899–911.

[123] A. E. Cheikh, A. Jacobi, A mathematical model for frost growth and densification on flat surfaces, Int. J. Heat Mass Transfer 77 (2014) 604–611.

[124] K. S. Lee, S. Jhee, D. K. Yang, Prediction of the frost formation on a cold flat surface, Int. J. Heat Mass Transfer 46 (20) (2003) 3789–3796.

[125] R. L. Gall, J. M. Grillot, C. Jallut, Modelling of frost growth and densification, Int. J. Heat Mass Transfer 40 (13) (1997) 3177–3187.

[126] P. L. T. Brian, R. C. Reid, Y. T. Shah, Frost deposition on cold surfaces, Ind. Eng. Chem. Fundament. 9 (3) (1970) 375–380.

[127] C. J. L. Hermes, F. R. Loyola, V. S. Nascimento, A semi-empirical correlation for the frost density, Int. J. Refrigeration 46 (2014) 100–104.

[128] C. J. L. Hermes, An analytical solution to the problem of frost growth and densification on flat surfaces, Int. J. Heat Mass Transfer 55 (23) (2012) 7346–7351.

[129] B. D. Storey, A. M. Jacobi, The effect of streamwise vortices on the frost growth rate in developing laminar channel flows, Int. J. Heat Mass Transfer 42 (20) (1999) 3787–3802.

[130] H. W. Schneider, Equation of the growth rate of frost forming on cooled surfaces, Int. J. Heat Mass Transfer 21 (8) (1978) 1019–1024.

[131] Y. B. Lee, S. T. Ro, Analysis of the frost growth on a flat plate by simple models of saturation and supersaturation, Exp. Therm. Fluid Sci. 29 (6) (2005) 685–696.

[132] C. J. L. Hermes, R. O. P. Piucco, C. Melo, J. R. Barbosa, A study of frost growth and densification on flat surfaces, Exp. Therm. Fluid Sci. 33 (2) (2009) 371–379.

[133] B. W. Jones, J. D. Parker, Frost formation with varying environmental parameters, J. Heat Transfer 97 (2) (1975) 255–259.

[134] D. K. Yang, K. S. Lee, Dimensionless correlations of frost properties on a cold plate, Int. J. Refrigeration 27 (1) (2004) 89–96.

[135] Y. Hayashi, A. Aoki, S. Adachi, K. Hori, Study of frost properties correlating with frost formation types, J. Heat Transfer 99 (2) (1977) 239–245.

[136] D. K. Yang, K. S. Lee, Modeling of frosting behavior on a cold plate, Int. J. Refrigeration 28 (3) (2005) 396–402.

[137] D. K. Yang, K. S. Lee, S. Song, Modeling for predicting frosting behavior of a fin–tube heat exchanger, Int. J. Heat Mass Transfer 49 (7) (2006) 1472–1479.

[138] J. M. Huang, W. C. Hsieh, X. J. Ke, C. C. Wang, The effects of frost thickness on the heat transfer of finned tube heat exchanger subject to the combined influence of fan types, Appl. Therm. Eng. 28 (7) (2008) 728–737.

[139] J. T. Kwon, H. J. Lim, Y. C. Kwon, S. Koyama, D. H. Kim, C. Kondou, An experimental study on frosting of laminar air flow on a cold surface with local cooling, Int. J. Refrigeration 29 (5) (2006) 754–760.

[140] I. Tokura, H. Saito, K. Kishinami, Study on properties and growth rate of frost layers on cold surfaces, J. Heat Transfer 105 (4) (1983) 895–901.

[141] S. Nath, J. B. Boreyko, On localized vapor pressure gradients governing condensation and frost phenomena, Langmuir 32 (2016) 8350–8365.

[142] C. Schäfle, C. Bechinger, B. Rinn, C. David, P. Leiderer, Cooperative evaporation in ordered arrays of volatile droplets, Phys. Rev. Lett. 83 (1999) 5302–5305. doi:10.1103/PhysRevLett.83.5302.
URL http://link.aps.org/doi/10.1103/PhysRevLett.83.5302

[143] C. Schafle, P. Leiderer, C. Bechinger, Subpattern formation during condensation processes on structured surfaces, Europhys. Lett. 63 (2003) 394–400.

[144] R. N. Leach, F. Stevens, S. C. Langford, J. T. Dickinson, Dropwise condensation: experiments and simulations of nucleation and growth of water drops in a cooling system, Langmuir 22 (2006) 8864–8872.

[145] Y. Zhao, C. Yang, Retarded condensate freezing propagation on superhydrophobic surfaces patterned with micropillars, Appl. Phys. Lett. 108 (2016) 061605.

[146] R. Williams, J. Blanc, Inhibition of water condensation by a soluble salt nucleus, J. Chem. Phys. 74 (8) (1981) 4675–4677.

[147] S. Biswas, A. Chakrabarti, A. Chateauminois, E. Wandersman, A. M. Prevost, M. K. Chaudhury, Soft lithography using nectar droplets, Langmuir 31 (2015) 13155–13164.

[148] M. Volmer, H. Flood, Tröpfchenbildung in dämpfen, Z. Phys. Chem. A 170 (1934) 273–285.

[149] V. P. Carey, Liquid–Vapor Phase-Change Phenomena, 2nd ed., CRC Press, Boca Raton, FL, 2007.

[150] H. Asakawa, G. Sazaki, K. Nagashima, S. Nakatsubo, Y. Furukawa, Two types of quasi-liquid layers on ice crystals are formed kinetically, Proc. Natl. Acad. Sci. U.S.A. 113 (7) (2016) 1749–1753.

[151] L. A. Guildner, D. P. Johnson, F. E. Jones, Vapor pressure of water at its triple point: highly accurate value, Science 191 (4233) (1976) 1261–1261.

[152] K. Sassen, G. C. Dodd, Homogeneous nucleation rate for highly supercooled cirrus cloud droplets, J. Atmos. Sci. 45 (8) (1988) 1357–1369.

[153] T. Peter, C. Marcolli, P. Spichtinger, T. Corti, M. B. Baker, T. Koop, When dry air is too humid, Science 314 (5804).

[154] H. Mendoza, V. P. Carey, A dsmc model on droplet clusters to explore the limiting factors of modified surfaces promoting enhanced dropwise condensation, in: ASME International Mechanical Engineering Congress and Exposition, American Society of Mechanical Engineers, 2015, p. V08AT10A035.

[155] H. Mendoza, S. Beaini, V. P. Carey, An exploration of transport within micro and nano droplet clusters during dropwise condensation of water on nanostructured surfaces, in: ASME International Mechanical Engineering Congress and Exposition, American Society of Mechanical Engineers, 2011, pp. 589–600.

[156] N. Bruot, F. Caupin, Curvature dependence of the liquid-vapor surface tension beyond the tolman approximation, Phys. Rev. Lett. 116 (2016) 056102. `doi:10.1103/PhysRevLett.116.056102`.
URL `http://link.aps.org/doi/10.1103/PhysRevLett.116.056102`

[157] N. Miljkovic, R. Enright, Y. Nam, K. Lopez, N. Dou, J. Sack, E. N. Wang, Jumping-droplet-enhanced condensation on scalable superhydrophobic nanostructured surfaces, Nano Lett. 13 (2013) 179–187.

[158] D. J. Preston, D. L. Mafra, N. Miljkovic, J. Kong, E. N. Wang, Scalable graphene coatings for enhanced condensation heat transfer, Nano Lett. 15 (2015) 2902–2909.

[159] T. Young, An essay on the cohesion of fluids, Phil. Trans. R. Soc. Lond. 95 (1805) 65–87.

[160] R. Enright, N. Miljkovic, A. Al-Obeidi, C. V. Thompson, E. N. Wang, Condensation on superhydrophobic surfaces: the role of local energy barriers and structure length scale, Langmuir 28 (2012) 14424–14432.

[161] R. Enright, N. Miljkovic, N. Dou, Y. Nam, E. N. Wang, Condensation on superhydrophobic copper oxide nanostructures, J. Heat Transfer 135 (2013) 091304.

[162] N. Miljkovic, R. Enright, E. N. Wang, Modeling and optimization of superhydrophobic condensation, J. Heat Transfer 135 (2013) 111004.

[163] P. G. de Gennes, F. Brochard-Wyart, D. Quéré, Capillarity and wetting phenomena: drops, bubbles, pearls, waves, Springer Science & Business Media, 2013.

[164] C. Parneix, P. Vandoolaeghe, V. S. Nikolayev, D. Quéré, J. Li, B. Cabane, Dips and rims in dried colloidal films, Physical review letters 105 (26) (2010) 266103.

[165] J. B. Boreyko, C. H. Chen, Self-propelled dropwise condensate on superhydrophobic surfaces, Phys. Rev. Lett. 103 (2009) 184501.

[166] K. Rykaczewski, Microdroplet growth mechanism during water condensation on superhydrophobic surfaces, Langmuir 28 (2012) 7720–7729.

[167] J. C. Bird, R. Dhiman, H. M. Kwon, K. K. Varanasi, Reducing the contact time of a bouncing drop, Nature 503 (2013) 385–388.

[168] A. R. Parker, C. R. Lawrence, Water capture by a desert beetle, Nature 414 (2001) 33–34.

[169] G. P. Lopez, H. A. Biebuyck, C. D. Frisbie, G. M. Whitesides, Imaging of features on surfaces by condensation figures, Science 260 (1993) 647–649.

[170] L. Zhai, M. C. Berg, F. C. Cebeci, Y. Kim, J. M. Milwid, M. F. Rubner, R. E. Cohen, Patterned superhydrophobic surfaces: toward a synthetic mimic of the namib desert beetle, Nano Lett. 6 (2006) 1213–1217.

[171] K. K. Varanasi, M. Hsu, N. Bhate, W. Yang, T. Deng, Spatial control in the heterogeneous nucleation of water, Appl. Phys. Lett. 95 (2009) 094101.

[172] C. W. Lo, C. C. Wang, M. C. Lu, Spatial control of heterogeneous nucleation on the superhydrophobic nanowire array, Adv. Funct. Mater. 24 (2014) 1211–1217.

[173] A. R. Betz, J. Jenkins, C. J. Kim, D. Attinger, Boiling heat transfer on superhydrophilic, superhydrophobic, and superbiphilic surfaces, Int. J. Heat Mass Transfer 57 (2013) 733–741.

[174] H. Gau, S. Herminghaus, P. Lenz, R. Lipowsky, Liquid morphologies on structured surfaces: from microchannels to microchips, Science 283 (1999) 46–49.

[175] A. N. Efremov, M. Grunze, P. A. Levkin, Digital liquid patterning: a versatile method for maskless generation of liquid patterns and gradients, Adv. Mater. Interfaces 1 (2014) 1300075.

[176] H. Kusumaatmaja, J. M. Yeomans, Modeling contact angle hysteresis on chemically patterned and superhydrophobic surfaces, Langmuir 23 (2007) 6019–6032.

[177] S. Varagnolo, D. Ferraro, P. Fantinel, M. Pierno, G. Mistura, G. Amati, L. Biferale, M. Sbragaglia, Stick-slip sliding of water drops on chemically heterogeneous surfaces, Phys. Rev. Lett. 111 (2013) 066101.

[178] D. Qin, Y. Xia, B. Xu, H. Yang, C. Zhu, G. M. Whitesides, Fabrication of ordered two-dimensional arrays of micro- and nanoparticles using patterned self-assembled monolayers as templates, Adv. Mater. 11 (1999) 1433–1437.

[179] F. L. Geyer, E. Ueda, U. Liebel, N. Grau, P. A. Levkin, Superhydrophobic-superhydrophilic micropatterning: towards genome-on-a-chip cell microarrays, Angew. Chem. Int. Ed. 50 (2011) 8424–8427.

[180] A. Ghosh, R. Ganguly, T. M. Schutzius, C. M. Megaridis, Wettability patterning for high-rate, pumpless fluid transport on open, non-planar microfluidic platforms, Lab Chip 14 (2014) 1538–1550.

[181] C. P. Tan, H. G. Craighead, Surface engineering and patterning using parylene for biological applications, Materials 3 (2010) 1803–1832.

[182] Y. Yamada, T. Ikuta, T. Nishiyama, K. Takahashi, Y. Takata, Droplet nucleation on a well-defined hydrophilic-hydrophobic surface of 10 nm order resolution, Langmuir 30 (2014) 14532–14537.

[183] M. Brinkmann, R. Lipowsky, Wetting morphologies on substrates with striped surface domains, J. Appl. Phys. 92 (2002) 4296–4306.

[184] J. B. Boreyko, C. H. Chen, Vapor chambers with jumping-drop liquid return from superhydrophobic condensers, Int. J. Heat Mass Transfer 61 (2013) 409–418.

[185] B. J. Mason, J. Maybank, The fragmentation and electrification of freezing water drops, Quart. J. Roy. Meteor. Soc. 87 (1960) 176–185.

[186] A. T. Paxson, J. L. Yague, K. K. Gleason, K. K. Varanasi, Stable dropwise condensation for enhancing heat transfer via the initiated chemical vapor deposition (icvd) of grafted polymer films, Adv. Mater. 26 (2014) 418–423.

[187] M. Kemp, Leonardo da Vinci: The Marvellous Works of Nature and Man, Oxford University Press, 2007.

[188] J. Aizenberg, A. J. Black, G. M. Whitesides, Oriented growth of calcite controlled by self-assembled monolayers of functionalized alkanethiols supported on gold and silver, J. Am. Chem. Soc. 121 (1999) 4500–4509.

[189] C. Dawson, J. F. V. Vincent, A. M. Rocca, How pine cones open, Nature 390 (6661) (1997) 668–668.

[190] R. Elbaum, L. Zaltzman, I. Burgert, P. Fratzl, The role of wheat awns in the seed dispersal unit, Science 316 (5826) (2007) 884–886.

[191] C. W. Chan, J. Ling-Chin, A. P. Roskilly, A review of chemical heat pumps, thermodynamic cycles and thermal energy storage technologies for low grade heat utilisation, Appl. Therm. Eng. 50 (2013) 1257–1273.

[192] S. Narayanan, X. Li, S. Yang, H. Kim, A. Umans, I. S. McKay, E. N. Wang, Thermal battery for portable climate control, Appl. Energ. 149 (2015) 104–116.

[193] E. Reyssat, L. Mahadevan, Hygromorphs: from pine cones to biomimetic bilayers, J. R. Soc. Interface 6 (39) (2009) 951–957.

[194] M. Ma, L. Guo, D. G. Anderson, R. Langer, Bio-inspired polymer composite actuator and generator driven by water gradients, Science 339 (6116) (2013) 186–189.

[195] X. Chen, L. Mahadevan, A. Driks, O. Sahin, Bacillus spores as building blocks for stimuli-responsive materials and nanogenerators, Nat. Nanotechnol. 9 (2) (2014) 137–141.

[196] X. Chen, D. Goodnight, Z. Gao, A. H. Cavusoglu, N. Sabharwal, M. DeLay, A. Driks, O. Sahin, Scaling up nanoscale water-driven energy conversion into evaporation-driven engines and generators, Nat. Commun. 6 (2015) 7346.

[197] X. Sun, K. Rykaczewski, Suppression of frost nucleation achieved using the nanoengineered integral humidity sink effect, ACS Nano 11 (2016) 906–917.

[198] T. Nishinaga, Handbook of Crystal Growth: Fundamentals, Elsevier, 2014.

[199] T. S. Wong, S. H. Kang, S. K. Y. Tang, E. J. Smythe, B. D. Hatton, A. Grinthal, J. Aizenberg, Bioinspired self-repairing slippery surfaces with pressure-stable omniphobicity, Nature 477 (2011) 443–447.